LATVIAN JOURNAL of PHYSICS and TECHNICAL SCIENCES

ISSN 0868 - 8257

(Vol. 62)

2025

CONTENTS

S. Zaichenko, D. Derevianko, O. Okhrimenko,
S. Korol, N. Shevchuk, N. Jukova
Modelling of the Generator Diagnosis System Based on a Spark Ignition Engine 3

S. R. Vejanand, A. Janushevskis, I. Vaicis
Selection of Appropriate Estimation Criteria in Flow Simulation Study for Predicting Cooling Efficiency of Ventilated Protective Clothing 17

F. I. Abbas, M. Sugiyama
A Comparative Study of Property Measurement for ZnO-Thin Film Growth Processes Using Hydrocloric Acid (HCl) and Water (H_2O) Solution-Dependent on Novel Electrostatic Spray Deposition (ESD) 30

S. Baghirov, V. Kharchenko, S. Shpak, O. Pitiakov,
S. Kyslytsia, T. Sakhno, H. Kozhushko
Influence of Eco-Design Policy and Energy Labeling on the Level of Energy Efficiency and Functionality of LED Lamps 42

J. V. Sanchaniya, G. Moothedath
Deformation Behaviour of Oriented Electrospun PAN Nanofiber Mats 60

D. Adilova, A. Tukhtamisheva, R. Bliudzius,
I. Geipele, L. Jansons, S. Lapuke
An Efficiency Study of Foamed Polyisocyanurate (PIR) Materials as Building Insulators 67

S. Al Sawafi
Polymer/Carbon Nanotube Nanocomposites for Strain Sensing Applications 81

A.G.E.M.I. Mowafy, I. Steiks
Maximising Efficiency and Stability in Photovoltaic-Reverse Osmosis Desalination Systems Through Data-Driven Optimisation and Advanced Control Strategies 91

LATVIAN JOURNAL of PHYSICS and TECHNICAL SCIENCES

LATVIJAS FIZIKAS un TEHNISKO ZINĀTŅU ŽURNĀLS

Published six times a year since February 1964
Iznāk sešas reizes gadā kopš 1964. gada februāra

2 (Vol. 62) • 2025

RĪGA

Language Editor: O. Ivanova
Computer Designer: I. Begicevs

INDEXED (PUBLISHED) IN

www.scopus.com
www.sciendo.com
EBSCO (Academic Search Complete, www.epnet.com), INSPEC (www.iee.org.com).
VINITI (www.viniti.ru), Begell House Inc/ (EDC, www.edata-center.com).

Issuers: Institute of Physical Energetics,
Institute of Solid State Physics, University of Latvia
Registration Certificate Number: 000700221

Editorial Contacts:
14 Dzerbenes Street, Riga, LV-1006
LATVIA
tel: +371 26245896
M: +371 29363105
leo@lza.lv

sciendo

LATVIAN JOURNAL OF PHYSICS
AND TECHNICAL SCIENCES
2025, N 2

DOI: 10.2478/lpts-2025-0009

MODELLING OF THE GENERATOR DIAGNOSIS SYSTEM BASED ON A SPARK IGNITION ENGINE

S. Zaichenko[1*], D. Derevianko[1], O. Okhrimenko[1],
S. Korol[2], N. Shevchuk[1], N. Jukova[1]

[1]Institute of Energy Saving and Energy Management,
National Technical University of Ukraine
"Igor Sikorsky Kyiv Polytechnic Institute"
37 Peremohy Ave., Kyiv, 03056, UKRAINE
[2]Thermometry Laboratories
Institute of Engineering Thermophysics of NAS of Ukraine
2[a] Marii Kapnist Str., Kyiv, 03057, UKRAINE
[*]e-mail: zstefv@gmail.com

This study proposes a new approach to the diagnosis of autonomous power-generating equipment operating on the basis of a spark-ignition engine, using computer simulation of the technical diagnosis system. The main idea of this method is the ability to mathematically determine the diagnostic parameters of the system, which allows analytically assessing the degree of wear of the cylinder-piston group. Determining the currents of the electric starter allows setting the functional parameter – the real degree of compression. This definition of the degree of compression allows setting the energy indicators of the generator. Using this method it is possible to establish the dependence of specific energy indicators on the technical condition of the generating plant. The conducted research resulted in the development of a multi-level hierarchical multi-component model of the system of technical diagnostics of a generator based on a spark-ignition engine. This model allows one to predict the diagnostic parameters of the research object and choose the necessary diagnostic tools. Calculation data obtained using the developed mathematical model of an electric generator with a single-cylinder engine and spark ignition based on real parameters testify to the high adequacy of the proposed mathematical model.

Keywords: *Electric generator, energy efficiency, internal combustion engine, fuel consumption.*

1. INTRODUCTION

Ukraine has considerable experience in the practical use of renewable energy sources. According to the estimated data of the long-term programme "Energy Conservation and Improvement of Energy Efficiency of Ukraine until 2050", the maximum use of renewable energy sources (RES) in Ukraine opens up real opportunities for increasing generation capacities based on them. Often, the use of RES technologies for autonomous power supply systems requires the availability of a reliable backup source of electricity. Electric generators based on internal combustion engines occupy the first place among reliable and profitable backup sources of electricity [1]– [3]. Electric generators based on internal combustion engines are also widely used independently to provide electricity in emergency situations and for humanitarian power supply.

Ensuring the efficient use of energy resources has always been of great interest to decision-makers at the national, European and international levels. The European Union (EU) and all its members signed and ratified the Paris Agreement, committing to reduce greenhouse gas emissions by 55 % by 2030 compared to 1990 levels. Achieving such a goal is possible only if reliable energy-generating equipment based on internal combustion engines with high energy efficiency and low emission levels is used. Maintenance of this equipment in good condition is possible thanks to the application of diagnostic methods aimed at monitoring indicators of its condition, which affect energy efficiency as a whole. Cylinder compression, or real compression, is one of the key indicators affecting the energy efficiency of power generating equipment. This indicator is determined by the ratio of the volume of the combustion chamber to the volume of the fuel-air mixture after closing the exhaust valve. Increased compression levels play a crucial role in enhancing the efficiency of fuel-air combustion. This, in turn, boosts productivity and lowers fuel consumption, thereby aiding in the pursuit of greater energy efficiency [4]–[8].

Obtaining experimental data and analysing diagnostic signs is the basis of the diagnostic process. These signs determine the state of the object under study depending on their informativeness. There are several diagnostic methods for the diagnosis of internal combustion engines, which is often carried out by comparing the obtained experimental data with normative ones. Compression measurement using compressors and barographs is a progressive method for diagnosing the tightness of the cylinder-piston group of an internal combustion engine. Among the disadvantages of this method, we can note the great laboriousness associated with disassembling the engine to measure compression, as well as the possible unreliability of the data obtained, which can arise for various reasons, such as the condition of the engine, the quality of the equipment and the correctness of its application.

The internal combustion engine diagnostic system, which uses the starter current level as a diagnostic parameter, will avoid the disadvantages associated with high labour intensity and unreliability of data that may occur when measuring compression. This method allows one to carry out diagnostics without the need to disassemble the engine, which simplifies the process and reduces its time and effort [6], [8]. Thus, diagnostic systems that are based

on the analysis of the change in the cranking moment of the spark-ignition engine without fuel supply in the compressor mode use the measurement of the starter current and voltage level as a diagnostic parameter. This method allows detecting anomalies in the operation of the engine, such as wear of the cylinder-piston group or problems with the lubrication system, without the need for extensive labour and disassembly of the engine. The motor testers, such as KAD30003, M32, MT3500 and similar, are examples of diagnostic complexes that use a diagnostic method based on the analysis of the change in the torque of the crankshaft of a spark ignition engine. They allow for comprehensive diagnostics of various engine systems and units, including checking the cylinder-piston group, starting system, ignition system, and others. The use of this method of diagnosis really allows increasing the reliability and accuracy of the results, while reducing labour costs. However, for the successful application of this method, it is necessary to have previously known values of diagnostic parameters, which can become a problem in the case of new diagnostic objects or unknown anomalies. Such limitations require careful planning and preparation before applying the method.

To predict the parameters of the system of technical diagnostics of the generator based on the engine with spark ignition using the compressor method, it is necessary to develop a process model that allows selecting system components. This model may include such components as mathematical equations, data analysis algorithms, statistical methods and other tools for predicting the state of the object and identifying possible malfunctions. An important part of developing such a model is choosing the right diagnostic parameters and their optimal combination to achieve the best forecasting results.

2. LITERATURE REVIEW

The studies of energy efficiency parameters of systems using a starter motor are divided into two main groups. The first group of studies concentrates on starting engines without switching the system into a special mode and describing functional diagnostic systems. The second group includes tests of the system in special modes, such as compression or with partial depressurization, and a description of diagnostic test systems.

Among the studies of the first group, which are distinguished by the high quality of the detailed description and formulation of the problem, it is possible to single out the starter alternator system in a hybrid electric vehicle [9]–[11]. The mentioned articles present an analytical model that is useful for analysing the torque of an internal combustion engine. This model also describes a control system that uses torque transfer with direct engine speed feedback to reduce engine torque ripple. The article proposes to use the dependencies describing the isothermal process to illustrate the process of air compression in cylinders. The application of these dependencies is possible provided that the real process of air compression by the engine starter in the compressor mode is considered.

In the studies devoted to the description of the functional diagnostic system, the crankcase gas pressure is used as a diagnostic parameter of the engine condition [12]–[14]. The articles do not contain proposals for mathematical modelling of the

diagnostic process. Application of the proposed method is possible only if experimental data are available for each specific object.

Research into the process of diagnosing the cylinder-piston group in the compressor mode is concentrated on the electrical parameters of starting the starter motor [15]–[18] or the pressure generated as a result of air compression [19]–[21] used as diagnostic indicators. The proposed models of the battery, electric starter and resistance of the engine with spark ignition can be useful for modelling the system of technical diagnostics of the generator.

When analysing the currents and pressures that occur during engine rotation, the supports originating from compression forces are taken into account, using the geometric parameters of the cylinder-piston group and the crank-connecting mechanism. Nevertheless, it is important to acknowledge that the overall resistance to rotation is not solely dictated by compression forces; rather, it is influenced by various other factors. These include the resistance stemming from lubricant blending, friction within rotating or slowly moving components, hindrance from auxiliary components within the power system, and inertial forces.

Setting the components of these components is a very difficult task due to the significant influence of the rheological and tribological properties of the system on the mechanics of the contact interaction of the elements [22]. Considering all the specified components, it is practically impossible to obtain a solution to the acquired systems of equations. Also, preliminary experimental studies confirm the significant influence of the flywheel, which temporarily evens out the curve of the current change.

Due to the complexity of the analytical solutions in many studies, numerical methods have been employed, utilising the Simulink/Matlab interactive simulation and analysis tool [23].

Considering the above, it is possible to conclude about the need to improve the theory, methods and means of existing methods of diagnostics of power equipment based on engines with spark ignition.

The aim of this research is to develop a mathematical model of a system of technical diagnostics of a generator based on a spark-ignition engine, where the starter current is used as a diagnostic indicator.

3. DESCRIPTION OF RESEARCH METHODS

Diagnostic indicators are used to determine the state of the spark-ignition engine as part of the power plant, particularly the current strength of the starter, which rotates the engine in compressor and depressurized modes. Diagnostics of the electric generator engine is carried out without fuel supply and with the load on the electric generator turned off.

Among the diverse spectrum of autonomous generators, the authors paid special attention to generating units that use a single-cylinder gasoline engine with a volume of 150 to 250 sm3. Table 1 shows the technical characteristics of these energy-generating systems. Most generators use a synchronous generator with an AVR, which includes both rotor and stator windings. The rotation of the generator rotor is provided by a centrifugal frequency regulator connected to the carburettor.

Table 1. Technical Characteristics of a Synchronous Electric Generator with a Spark Ignition Engine

Parameter	Unit	Value
Engine type	-	4-stroke gasoline engine with air cooling OHV
Number of cylinders	-	1
Engine model	-	168F, 170F, HONDA GX160, GX200
Engine capacity	cm^3	150-250
Rated engine power	W	3.3-4800
Maximum power	W	2800
The volume of the fuel tank	m^3	0.015
The volume of the oil sump	m^3	~0.0006
Weight	kg	53.6

This type of equipment uses a permanent magnet DC collector motor that has a high torque. The electric starter is equipped with a special relay that switches the power supply to the electric motor and controls a special clutch assembly with the engine flywheel with spark ignition.

The generator diagnostics process includes the following main components: generator (1), internal combustion engine (2), gearbox (3), starter (4), direct current sources (battery) (5), Hall effect sensor (6), sensor power source (7), analogue-digital converter (8) and computer (9) (see Fig. 1). The process of obtaining diagnostic data involves fixing the position of the crankshaft of the internal combustion engine (2) and the stator current (4) by the computer (9). This diagnostic system allows detecting the relationship between the stator current and the state of the thermal unit of the power plant. During the development of this diagnostic test system, the main aspect is the determination of the equipment parameters that will ensure the necessary accuracy and reliability of the process. The effectiveness of diagnostics depends on the energy characteristics, which determine the choice of sensors according to a certain level of direct current, the power of the current source and the polling frequency of the analogue-to-digital converter channels. The use of interactive tools for building multilevel hierarchical multi-component models of the system of technical diagnostics of a generator based on a spark-ignition engine will allow predicting the physical parameters of processes.

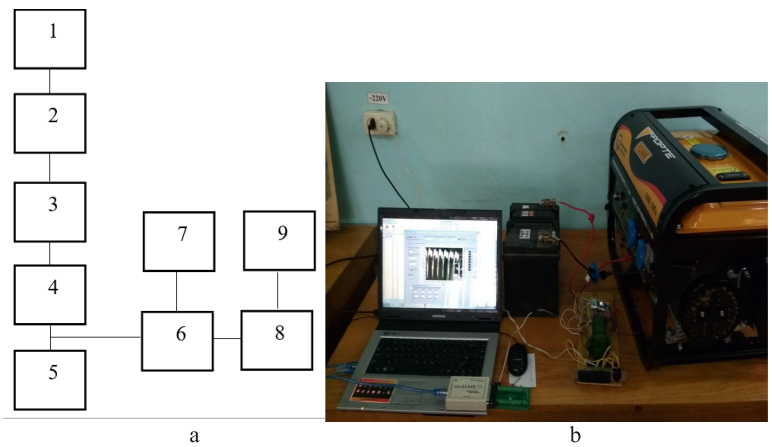

Fig. 1. Scheme (a) and appearance (b) of the system for diagnosing generators by starter current.

Figure 2 shows the scheme of the mathematical model of the system of technical diagnostics of the generator based on the engine with spark ignition. In the electromechanical scheme of this diagnostic system, the main components are the elements of the crank mechanism, such as piston (1), connecting rod (2) and crankshaft (3), as well as the generator rotor (4) and flywheel (5). There are also starter armature (6) and armature windings (7).

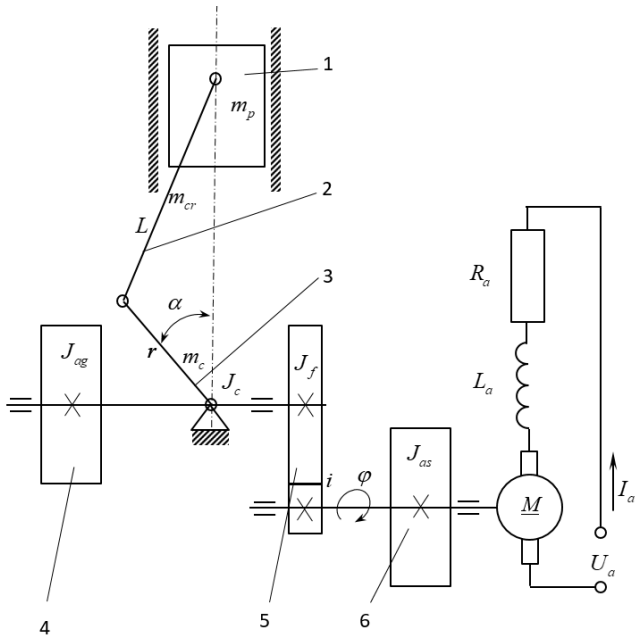

Fig. 2. Scheme of the electromechanical system of diagnostics of a generator operating based on an engine with spark ignition.

The functioning of the electric starter can be described by a system of differential equations in the normal Cauchy form for a DC motor with independent excitation from permanent magnets:

$$\begin{cases} U_a - R_a I_a - k_\omega \dfrac{d\varphi}{dt} = L_a \dfrac{dI_a}{dt}; \\ k_m I_a - b\dfrac{d\varphi}{dt} - M_0 / i_g = J_0 \dfrac{d^2\varphi}{dt^2}; \end{cases} \tag{1}$$

where U_a – DC power supply voltage; i_g – gear ratio of the electric starter reducer; R_a and L_a – active resistance and inductance of the armature winding; b – viscous friction resistance; k_ω – constant electromotive force of the engine; k_m – engine torque constant; M_0 – moment of resistance to rotation of the shaft; J_0 – the given moment of inertia.

The moment of inertia, taking into account the flywheel transmission ratio, is formed from a constant moment and a variable moment associated with a change in the inertia of the system:

$$J_0 = J_1 + J_2 = J_{as} + \left(J_f + J_{ag} + J_c + m_2 R^2\right)\left(1/i_g\right)^2 +$$

$$+\left(m_p + m_1\right)\left(\frac{r(\sin\left(\varphi/i_g\right) + \frac{R}{2L}\sin 2\,\varphi/i_g)}{i_g}\right)^2, \quad (2)$$

where m_1, m_2 – the separated mass of the connecting rod, which connects the piston and the crankshaft.

The analysis of the dependence of the change in the components of the moment of inertia of the selected diagnostic system during one rotation of the crankshaft shows the harmonic nature of the changes during the rotation of the crankshaft and the change in the moment of inertia within 0.8 %. Taking into account the insignificant influence of the variable inertial component, this system moment of inertia can be calculated with high accuracy by considering only its constant component.

In the balance of the moment of mechanical losses, the main parameter under consideration is the moment of resistance arising from the compressive forces in the cylinder. The moment of resistance is calculated using the dependence that connects the pressure and the kinematic characteristics of the system:

$$M_c \approx p_c F_c R\left(\sin(\varphi / i_g) + \frac{\lambda}{2}\sin(2\varphi / i_g)\right),\ \varphi / i_g \in (0;\pi), \quad (3)$$

where F_c – piston area; $\lambda = R / L$ – crank radius ratio R to the length of the connecting rod L; p_c – current pressure in the cylinder; R – crank radius.

With a certain approximation, it can be assumed that the increase in current pressure in the cylinder occurs according to the following dependence:

$$M_c \approx \frac{p_{\max}}{\pi}\varphi / i_g F_c R\left(\sin(\varphi / i_g) + \frac{\lambda}{2}\sin(2\varphi / i_g)\right),\ \varphi / i_g \in (0;\pi). \quad (4)$$

The resistances that arise from the forces of mechanical friction in the cylinder-piston group and from the hydraulic resistance during the passage of air are also significant. Mechanical losses include a number of aspects, such as overcoming the friction of pistons in cylinders, friction in bearings, losses associated with the operation of the pump (to carry out intake and exhaust processes), energy losses on the drive of auxiliary mechanisms (such as the distribution mechanism, oil, water and fuel pumps, as well as ventilation losses, etc.). During engine diagnostics at low speeds (<20 rad/s), hydraulic expenses are negligible. At this operational mode, approximately 90 % of mechanical losses stem from piston friction within the cylinders. The means of theoretical courses and special literature on the mechanics of contact interaction allow calculating the friction moment of piston rings using the following expression:

$$M_r \approx p_r i_r \pi D h \mu R \left(\sin(\varphi / i_g) + \frac{\lambda}{2} \sin(2\varphi / i_g) \right), \quad (5)$$

where p_r – radial pressure from the elastic forces of the piston ring; h – the height of the piston ring; i_r – the number of piston rings; D – cylinder diameter; μ – a coefficient of friction of the piston rings on the cylinder wall.

The total resistance arises from the forces of mechanical friction in the cylinder-piston group and from the compression forces in the cylinder:

$$M_r \approx \left| R \left(p_r i_r \pi D h \mu + \frac{p_c}{\pi i_g} \varphi F_c \right) \left(\sin(\varphi / i_g) + \frac{\lambda}{2} \sin(2\varphi / i_g) \right) \right|. \quad (6)$$

It should be noted that the total resistance to the rotation of the generator by the starter (6) has a constant value, regardless of the position of the crankshaft. It is also necessary to specify that the compression component of the total resistance acts on the part $(0;\pi)$ the entire cycle $(\pi;4\pi)$:

$$\begin{aligned} &M_c = R \text{ , with } \varphi / i_g \in (0;\pi) \text{ ;} \\ &M_c = 0 \text{ , with } \varphi / i_g \in (\pi;4\pi) \text{ .} \end{aligned} \quad (7)$$

The following expression was used in the modelling process:

$$f(\varphi) = \frac{\varphi}{i_g} \cdot \theta \left(0,25 - \left(\frac{\varphi}{i_g \cdot 4\pi} - \left[\frac{\varphi}{i_g \cdot 4\pi} \right] \right) \right). \quad (8)$$

Figure 3 shows a block diagram in an interactive programming environment for displaying the resistance that arises from the mechanical friction forces of the cylinder-piston group and from the compression forces in the cylinder (6).

In the block diagram using frames, the components reflecting the compression forces in the cylinder (3) and the friction forces of the piston rings (5) are marked. The function that determines the position of the crankshaft depending on the angle of rotation of the stator armature is shown by block (8). The main parameters describing the mechanical system include: maximum pressure $p_{\max} = 0.9MPa$; diameter of the cylinder $D = 0.07m$; crank radius $R = 0.0275m$; connecting rod length $L = 0.06m$;thickness of piston rings $i_r = 0.025m$; the number of piston rings $i_r = 3$; radial pressure from the elastic forces of the piston ring $p_r = 0.3MPa$; coefficient of friction of the piston rings on the cylinder wall $\mu = 0.4$.

The total moment of resistance arising from the forces of mechanical friction (Fig. 2) makes it possible to create a block

diagram based on the system of equations (1), which describes the functioning of the generator electric starter. The block diagram that describes the operation of the electric generator starter includes three main blocks: (I) – the block of integration of the first equation to determine the current of the armature windings; (II) – the block of integration of the second equation for determining the angle and speed of rotation of the armature; (III) – the load unit from a spark-ignition engine. Parts reflecting inertial forces and resistance from mechanical friction and air compression are added using a negative sign (Fig. 4). The parameters of the circuit block in the interactive environment for determining the parameters of the diagnostic system became: DC power supply voltage $U_a = 12V$;became the electromotive force of the engine $k_\omega = 0.35Nm/A$; viscous friction resistance $b = 0.012Nms/rad$; became the torque of the engine $k_m = 0.35Vs/rad$; gear ratio of the electric starter gearbox $i_g = 15$; active resistance $R_a = 0.1\Omega$ and the inductance of the armature winding $L_a = 0.0001H$; given moment of inertia $J_0 = 0.00093kg \cdot m^2$.

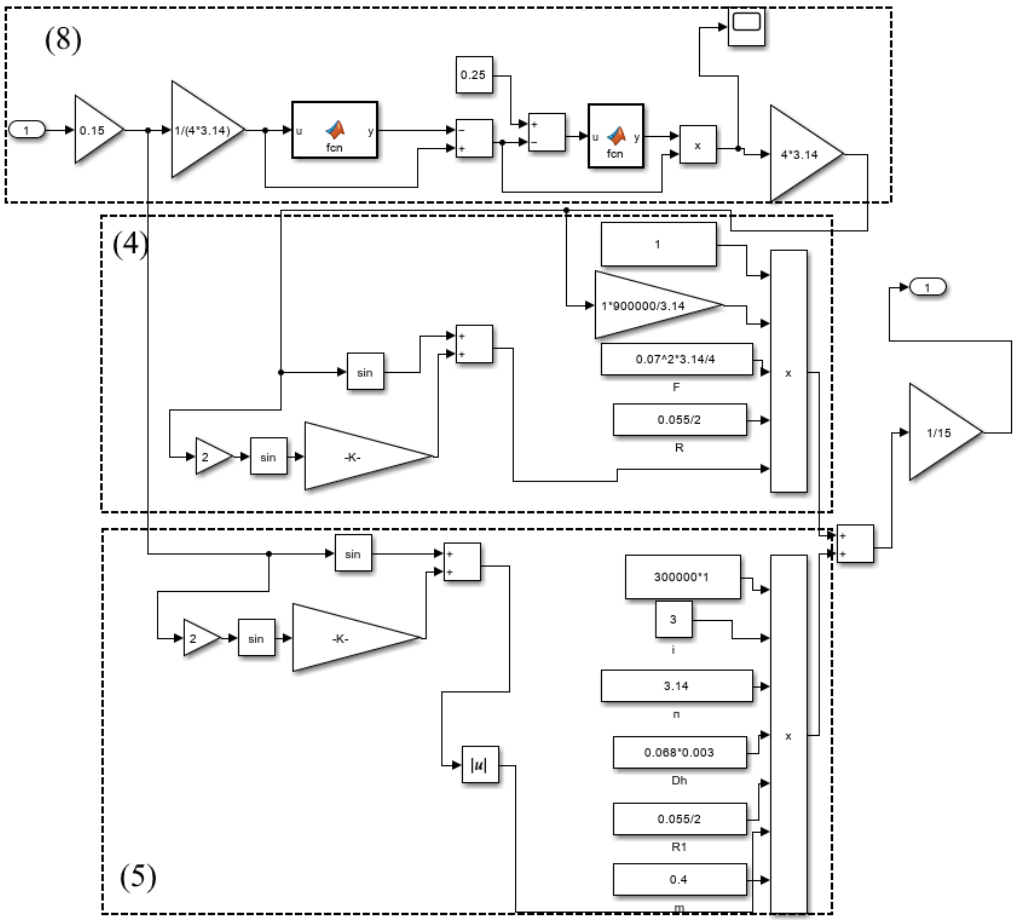

Fig. 3. Block diagram in an interactive environment for determining the resistance from the forces of mechanical friction and air compression.

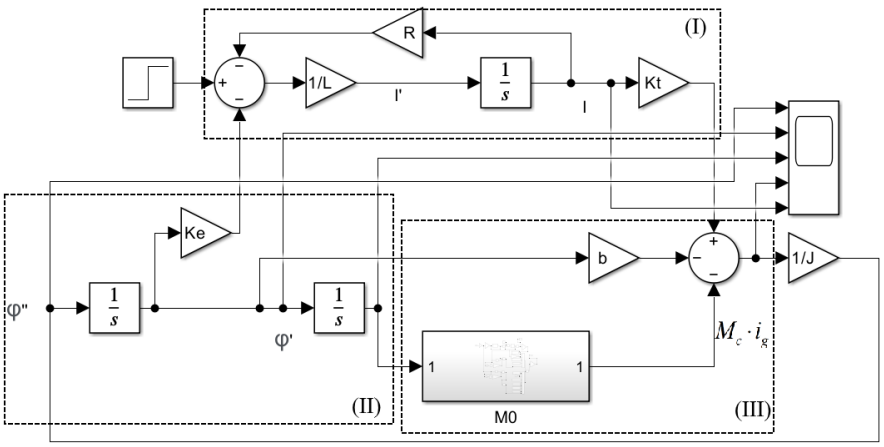

Fig. 4. Block diagram in an interactive environment for determining the parameters of the diagnostic system.

The developed block diagram allows determining the main parameters of the diagnostic system: current I_a, A and the angular speed of rotation of the electric starter $\frac{d\varphi}{dt}, rad^{-1}$ from time t, s . In addition to these parameters, it is also possible to determine the total torque on the starter armature, the angular acceleration of the starter, the rotation angle of the starter, and others. Figure 5 shows the graphs of changes in the angular speed of rotation of the electric starter $\frac{d\varphi}{dt}, rad^{-1}$ from time t, s in pressurized (compressor) and depressurized states.

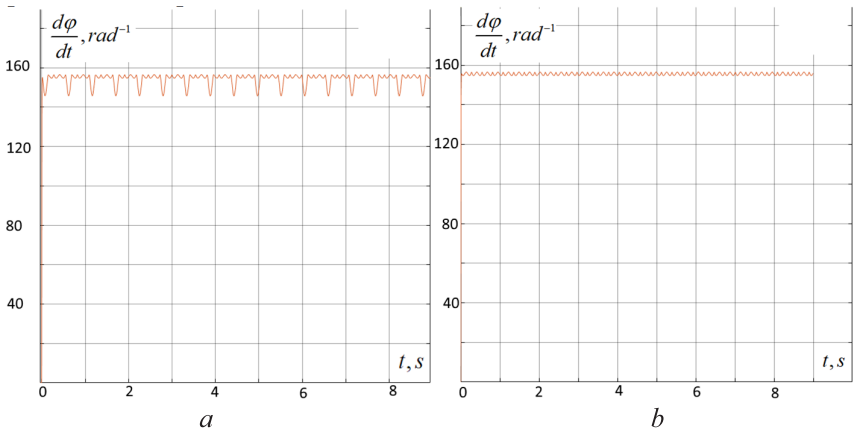

Fig. 5. Graphs of changes in the angular speed of rotation of the electric starter:
a – sealed state; b – depressurized state.

It can be understood from the graphs that in the compressor mode there is a pulsation and a decrease in the average speed, which is caused by the influence of the compression forces in the cylinder and the kinematics of the crankshaft.

Analysis of graphs of changes in starter current I_a over time indicates a substantial increase in pulsation, which is associated with the load from air compression forces (Fig. 6). The possibility of using the current strength of the electric starter to determine the state of the generator is confirmed by the significant influence of air compression forces.

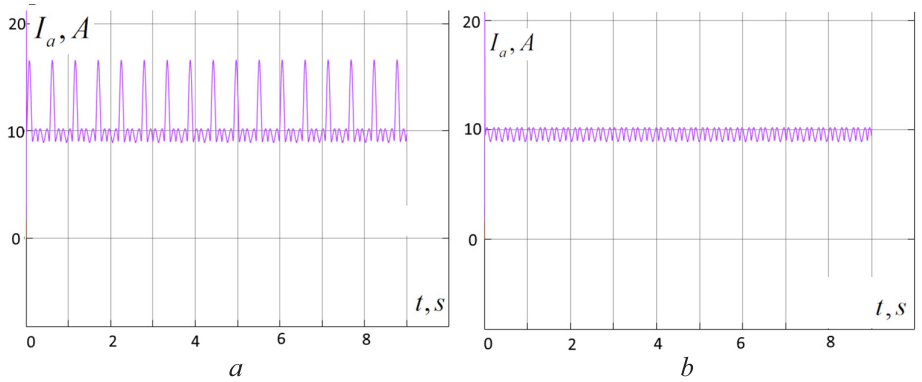

Fig. 6. Graphs of changes in electric starter current versus time:
a – sealed state; b – depressurized state.

The generalized energy balance of the diagnostic system can be presented as follows:

$$\sum_{i=1}^{n} A_i = \sum_{i=1}^{n} Q_i, \tag{9}$$

where A_i – operation of an external energy source;
Q_i – energy consumption for the implementation of a number of internal processes during engine rotation.

The power of the starter can be determined according to the technical documentation or depending on:

$$N_{st} = UI, \tag{10}$$

where U – battery voltage;
I – the average current for one cycle of the engine is determined by the results of modelling (Fig. 5).

Energy costs for the implementation of internal processes during engine rotation consist of costs for friction of parts Q_{fr} and thermodynamic gas Q_{ad} processes:

$$\sum_{i=1}^{n} Q_i = Q_{fr} + Q_{ad}. \tag{11}$$

It is possible to ignore the energy consumption for the rotation of the generator due to the fact that the starting frequency of the motor is only 5 % of the nominal frequency of rotation of the generator.

Friction costs of parts Q_{fr} are laid from a number of components that are related to the mixing of the piston, the rotation of the crankshaft, the operation of the oil pump, and the operation of the gas distribution mechanism. It is possible to determine friction costs of parts Q_{fr} when starting the engine without a screwed-in spark plug:

$$Q_{fr} = UI_1 \Delta t, \tag{12}$$

where I_1 – the average starter current without a screwed-in spark plug (depressurized state) (Fig. 5).

The costs of the gas thermal processes in compressed air are caused by the emission of heat Q_{ad}. From the known dependence of the indicator efficiency coefficient of gas thermodynamic processes Q_{ad} is as follows:

$$Q_{ad} = \eta_i A_{ad}, \tag{13}$$

where η_i – indicator coefficient of useful action:

$$\eta_i = 1 - \frac{1}{\varepsilon^{n-1}}, \tag{14}$$

where n' – experimental coefficient $1 < n < k$;
ε – engine compression ratio.

Work with polytropic compression:

$$Q_{ad} = \frac{p_0 V_0}{n-1}\left[\left(\frac{V_0}{V_1}\right)^{n-1} - 1\right], \quad (15)$$

where p_0 – initial pressure in the cylinder;
V_0 – the initial volume in the cylinder;
V_1 – final volume in the cylinder;
n – polytrophic index for air (1.2–1.365);

The relation V_0/V_1 pertains to the engine's compression ratio ε .

After substituting dependence (10–15) in (9) and assuming equality of coefficients $n' \approx k$ we obtain the energy balance equation of the diagnostic system:

$$\Delta tUI = \Delta tUI' + \frac{1}{\varepsilon^{n-1}} \frac{p_0 V_0}{\gamma - 1}\left[\left(\frac{V_0}{V_1}\right)^{n-1} - 1\right]. \quad (16)$$

Let us determine the degree of compression of the engine ε:

$$\varepsilon = \left(\frac{p_0 V_0}{\Delta tU(I(1-n) + I_1(n-1)) + p_0 V}\right)^{\frac{1}{n-1}}. \quad (17)$$

Solving Eq. (16) with respect to the degree of compression of the engine allows determining the energy efficiency of the electric generator. For analysis, we introduce a substitution in the obtained solution (17) using the ratio of currents:

$$k_I = \frac{I_1}{I}. \quad (18)$$

The current ratio coefficient in the adopted diagnostic system is an informative criterion that establishes a connection between two states of the system (pressurized (compressor) and depressurized states).

After substituting (18), the solution (17) takes the form

$$\varepsilon = \left(\frac{p_0 V_0}{\Delta tUI((1-n) + k(n-1)) + p_0 V}\right)^{\frac{1}{n-1}}. \quad (19)$$

As a result of using the value of the ratio of currents in the formula for the compression ratio, a value of 8.78 was obtained. The value of the passport compression ratio for this engine model is 9 units. Using Eq. (13) to determine the compression ratio, we can calculate the energy efficiency of the generator using the indicator coefficient of useful action. In this case, under the condition that the efficiency of the alternator is almost equal to 1, the energy efficiency of the generator is 0.22. The obtained value of energy efficiency corresponds to the results of previous studies conducted earlier [8].

4. CONCLUSION

A mathematical model has been developed in an interactive environment for diagnosing generators based on a spark-ignition engine. This model uses starter current as a diagnostic indicator. The mathematical model allows determining the main parameters of the diagnostic system, such as the current and angular speed of rotation of the electric starter as a function of time. In addition to the main parameters, the model also allows determining additional indicators that can be useful for assessing the condition of the generator, such as the total torque on the starter armature, angular acceleration and angle of rotation of the starter. Determining the ratio of current strength values in different modes allows establishing the energy efficiency of the generator. For a specific example of a generator based on the HONDA GX160 engine, it has been found that its energy efficiency is 0.22. Therefore, the developed mathematical model in an

interactive environment is a powerful tool for diagnosing and evaluating the energy efficiency of spark-ignition engine-based generators.

REFERENCES

1. Gaitan, N., Ungurean, I., Corotinschi, G., & Roman, C. (2020). An Intelligent Energy Management System Solution for Multiple Renewable Energy Sources. *Sustainability*, *15* (3), 2531.
2. Kim, H., Choi, H., Kang, H., An, J., Yeom, S., & Hong, T. (2021). A Systematic Review of the Smart Energy Conservation System: From Smart Homes to Sustainable Smart Cities. *Renewable and Sustainable Energy Reviews*, *140*, 110755.
3. Holub, H., Kulbovskyi, I., Skok, P., Bambura, O., Melnychenko, O., Kharuta, V., & Tretynychenko, Y. (2020). System model of information flows in networks of the electric supply system in transport infrastructure projects. In *Transport Means – Proceedings of the International Conference* (pp. 132–135).
4. Holub, H., Kulbovskyi, I., Sayapina, I., & Muraviov, V. (2023). Research of the information system of management of electrical supply processes on the railway using BPwim tools. In *Transport Means – Proceedings of the International Conference* (pp. 879–883), October 2023.
5. Kharrich, M., Kamel, S., Alghamdi, A., Eid, A., Mosaad, M., Akherraz, M., & Abdel-Akher, M. (2021). Optimal Design of an Isolated Hybrid Microgrid for Enhanced Deployment of Renewable Energy Sources in Saudi Arabia. *Sustainability*, *13* (9), 4708.
6. Zaichenko, S., Shevchuk, S., Kulish, R., Denysiuk, S., Derevianko, D., & Opryshko, V. (2021). Identification of the least reliable elements of autonomous power plant based on internal combustion and diesel engines by the method of the lowest residual entropy. In *2021 IEEE 2nd KhPI Week on Advanced Technology (KhPIWeek)*, vol. 1, (pp. 549–552), September 2021.
7. Zaichenko, S., Shevchuk, S., Kulish, R., Denysiuk, S., Derevianko, D., & Opryshko, V. (2021). Identification of the least reliable elements of autonomous power plant based on internal combustion and diesel engines by the method of the lowest residual entropy. In *2021 IEEE 2nd KhPI Week on Advanced Technology (KhPIWeek)*, September 2021, vol. 1, (pp. 549–552).
8. Zaichenko, S., Shevchuk, S., Opryshko, V., Pryadko, S., Halem, A., & Adjebi, A. (2020). Determination of autonomous electrical energy source technical condition based on an ISE. In *2020 IEEE 2nd KhPI Week on Advanced Technology (KhPIWeek)*, vol. 1, (pp. 305–308), October 2020.
9. Zaichenko, S., Shevchuk, S., Opryshko, V., Pryadko, S., & Halem, A. (2020). Autonomous electric power source energy efficiency improvement by ICE gases distribution control. In *2020 IEEE 7th International Conference on Energy Smart Systems (ESS)* (pp. 262–265), May 2020.
10. Zaichenko, S., & Derevianko, D. (2023). Comparison of the energy efficiency of synchronous power generator with spark ignition engine using different types of fuels. In *Systems, Decision and Control in Energy V* (pp. 155-177). Cham: Springer Nature Switzerland.
11. Cauet, S., Etien, E., & Rambault, L. (2017). Mechanical Sensorless LPV Torque Ripple Control of Hybrid Electric Vehicle. *IET Control Theory & Applications*, *11* (16), 2761–2771.
12. Qin, Y., Tang, X., Jia, T., Duan, Z., Zhang, J., Li, Y., & Zheng, L. (2020). Noise and Vibration Suppression in Hybrid Electric Vehicles: State of the Art and Challenges. *Renewable and Sustainable Energy Reviews*, *124*, 109782.

13. Davis, R., & Lorenz, R. (2003). Engine Torque Ripple Cancellation with an Integrated Starter Alternator in a Hybrid Electric Vehicle: Implementation and Control. *IEEE Transactions on Industry Applications*, *39* (6), 1765–1774.
14. Baboshin, A., Kosarev, A., & Malyshev, V. (2013). Assessing the Technical Condition of Internal Combustion Engines (ICEs) Based on Pressure Readings in the Intake and Exhaust Manifolds. *Bulletin of Technical University*, *3*, 23–32.
15. Baboshin, A., & Malyshev, V. (2010). Creating a Methodology for Comprehensive Engine Diagnosis and Devising Tools for Evaluating the Technical State of the Piston Component of Internal Combustion Engines. *Bulletin of the Technical University*, *4* (2), 925–930.
16. Bazhinov, A., & Serikova, E. (2009). A Software and Hardware System for Estimating the Remaining Lifespan of an Internal Combustion Engine. *Bulletin of Kharkov National Automobile and Highway University*, *45*, 25–31.
17. Averbukh, M., Rivin, B., & Vinogradov, J. (2007). On-board Battery Condition Diagnostics Using Mathematical Modeling of an Engine Starting System. *SAE Transactions*, *1476*, 406–413.
18. Nechaev, V., Kapustin, V., & Korablin, I. (2018). An Indiscriminate Method for Determining the State of a Cylinder-Piston Engine Group by the Spread of Compression. *Science*, *Education and Innovation in the Modern World*, *7*, 346–352.
19. Nechaev, V., Vorobev, E., & Tarasenko, A. (2018). Methods for the Technical Diagnosis of Diesel Cylinder-Piston Groups through Cold Cranking of the Crankshaft. *Engineering Bulletin of the Don*, *3* (50), 31–39.
20. Krivtsov, S., Ukkunov, Y., & Krivtsova, T. (2010). The Theoretical Foundation of the Method for Diagnosing the Compression Properties of a Diesel Engine Based on Current Parameters. *Bulletin of the Agricultural Academy*, *38*, 71–77.
21. Krivtsov, S., Pukalo, A., & Krivtsova, T. (2015). Contrast of Diagnostic Parameters Used to Assess the Piston Chamber Tightness in Diesel Engine Cylinders during Starter Rotation without Fuel Supply. *Automotive Engineers Journal*, *6*, 54–57.
22. Kukov, S., Gritsenko, A., & Bakaykin, D. (2016). Enhancing the Procedure for Diagnosing a Cylinder-Piston Assembly. *Materials from the LV International Scientific and Technical Conference Achievements of Science in Agricultural Production*, *1*, 77–82.
23. Larin, O., Kukov, S., Gritsenko, A., & Glemba, K. (2016). Diagnostic Results of the Cylinder-Piston Group by the Method of Assessing Dynamic Compression. *Agrobusiness*, *23* (3), 619–625.
24. Zaichenko, S., & Shevchuk, S. (2014). Formation of Geotechnical Properties of the Rock Mass Adjacent to Tunnels by Roll Pressing. *Scientific Bulletin of National Mining University*, *2*, 45–49.
25. Lefter, E. (2014). Aspects of simulating the behavior of an ISE for electric starter testing. *Electronics, Computers and Artificial Intelligence (ECAI), 2014 6th International Conference on IEEE*, 35–38.

sciendo

LATVIAN JOURNAL OF PHYSICS
AND TECHNICAL SCIENCES
2025, N 2

DOI: 10.2478/lpts-2025-0010

SELECTION OF APPROPRIATE ESTIMATION CRITERIA IN FLOW SIMULATION STUDY FOR PREDICTING COOLING EFFICIENCY OF VENTILATED PROTECTIVE CLOTHING

S. R. Vejanand, A. Janushevskis*, I. Vaicis

Institute of Mechanical and Biomedical Engineering,
Riga Technical University,
6A Kipsalas Str., Riga, LV-1048, LATVIA
*e-pasts: aleksandrs.janusevskis@rtu.lv

A Computational Fluid Dynamics (CFD) is utilised in various research and engineering areas across multiple fields and industries. The research field of ventilation and indoor air science has experienced a significant surge in scientific articles focused on the utilisation of CFD. With the solution of increasingly complicated ventilation problems, CFD validation and verification are more important than ever. The present study focuses on the crucial task of selecting suitable criteria in a flow simulation analysis aimed at predicting the cooling efficiency of ventilated protective clothing. This study examines three different cases of a simplified elliptical model of the human body with a protective jacket comprising 11, 48, and 105 ventilation elements. SolidWorks Flow Simulation is used to simulate all three models individually to calculate values of eight different criteria. It is assumed that increasing the number of ventilation units would result in an enhancement of cooling efficiency. However, it is crucial to understand how the values of various criteria change in flow simulation studies under different situations, and which criteria are crucial for the analysis. The criteria values for three cases are recorded and compared. The analysis results indicate a gradual increase in values of heat transfer rate, pressure and temperature differences as the number of ventilation units increases. However, certain parameter values like flow pressure difference do not provide sufficient information to predict efficiency of the system, whereas a parameter like average temperature shows low sensitivity. The study suggests that the heat transfer rate and heat flux are the most appropriate criterion to be examined in such a situation. This is due to the fact that an increased heat transfer rate from the body signifies a more effective cooling mechanism.

Keywords: *CFD, heat transfer, protective jacket, SolidWorks flow simulation, ventilation.*

1. INTRODUCTION

The efficient design and management of ventilation systems are crucial for maintaining indoor air quality and improving building energy efficiency [1]. The characteristics of the airflow within a building have a significant impact on the effectiveness of ventilation systems in removing pollutants from that space [2]. The same is true for ventilated protective clothing. Computational Fluid Dynamics (CFD) has been extensively utilised for the design and implementation of building ventilation systems. This approach is also increasingly being adopted in other areas of fluid dynamics research, such as the ventilation of protective clothing [3]. To design systems involving fluid flows, CFD simulations are frequently used as the base. Recent developments in CFD have enabled the creation of precise engineering models that capture the irregular shape of a clothed human body, as well as the significant variations in length and time scales that are typically encountered in computational simulations. These variations include thin layers of clothing covering a relatively large human body and irregular air spaces. Body-fitted coordinates or unstructured grids are employed to simulate intricate structures, such as a clothed human arm covered by a permeable layer of clothes, or simpler geometries like a cylinder covered with fabric [4]. This enhanced functionality can assist researchers in designing protective equipment that is both more comfortable and more effective.

In order to ensure human thermal comfort, it is necessary to maintain a heat balance between the human body and the surrounding environment. This involves regulating the heat generated within the body and the heat transferred to or from the body. The heat dissipation/gain process is influenced by multiple factors, and it involves different types of heat transport, such as conduction, convection, radiation, and evaporation. When the body absorbs more heat than it can release, it leads to thermal discomfort as the body's core temperature and heat storage grow. Normally, the body's core temperature is around 36.5 °C (+ or - 1 °C) in thermal comfort conditions. Experiencing an excessive increase in body heat may cause a serious threat to one's health and lead to heat stress. In order to alleviate heat stress or attain thermal comfort in such circumstances, it is imperative to implement efficient cooling methods [5]. Utilising personal cooling systems to provide individualised cooling can be an effective method to reduce heat stress or achieve thermal comfort in situations when implementing widespread air conditioning is not possible [6]. Personal cooling systems (PCS) are specifically developed to reduce the risks posed by elevated core body temperatures, while also enhancing the overall job performance of individuals. Various personal cooling systems are available, such as a cooling chair [7], wrist-band devices [8], radiant cooling desk [9], desk fan [10], and personal cooling clothing [11]–[14], and so on. Clothing creates its own atmosphere and is our most personal space, according to Watkins [15].

Computational Fluid Dynamics (CFD) is utilised to analyse the air exchange rates and forecast thermal comfort resulting from fluctuations in air flow. CFD allows us to adequately measure the heat and mass transfer, as well as analyse the airflow pattern within the garment system. The variation in thermal comfort is dependent on the quantity and arrangement of ventilation. Despite being constructed of the same material, the thickness and structure

of the air layer in a garment can vary significantly based on factors such as design, construction, easiness, openness, and slits. As a result, the ventilation impact will also differ significantly. Through the utilisation of CFD, we may include the air layer, openness, and slit as factors and forecast the thermal comfort sensation by establishing a correlation between results and human subject tests [16].

The current research concentrates on the important challenge of selecting appropriate criteria for a flow simulation analysis that is intended to predict the cooling performance of ventilated protective garments. In this study, three distinct cases of a simplified elliptical model of the human body with a protective jacket are investigated. The simplified elliptical model of the body and jacket is selected to reduce the complexity of the problem. The first model consists of eleven ventilation holes where there is a single inlet at the front and 10 outlets at the backside of the jacket. The second model is with 48 ventilation holes, having 24 inlets & 24 outlets, and the third model is with 105 ventilation holes, where there are 48 inlets and 57 outlets. For calculating the values of eight different criteria, SolidWorks Flow Simulation is utilised to simulate each of the three models individually. One can logically hypothesise that increasing the number of ventilation units will result in enhanced efficiency of the cooling. However, it is crucial to fully understand how the values of different parameters in flow simulation studies vary based on specific circumstances, and which parameter is the most appropriate to select in order to achieve a logical conclusion.

2. MODEL DESIGN AND BOUNDARY CONDITIONS

The model design with three distinct cases is depicted in Figs. 1–3, respectively. To reduce the complexity of the problem in this study, we have designed and assembled simple elliptical models of the body and jacket. The body remains centred, and the jacket is positioned over it. The ventilation hole diameter of 4.4 mm is used in all three cases, and toroidal cut out shaped ventilation element [17] is positioned to all the ventilation holes. The ventilation element is positioned at the ventilation hole in a concentric manner, with the front face of the element precisely aligned with the hole. The schematic diagram of ventilation element and its position to ventilation hole is shown in Fig. 4. The ventilation elements are positioned at the internal part of the jacket in the air gap between the body and jacket. This uniform air gap of 3.4 mm is shown in Figs. 1 and 2, with Detail View D. The air gap remains the same in all three cases stated in this study. All the dimensions presented in Figs. 1–4 are in millimetres.

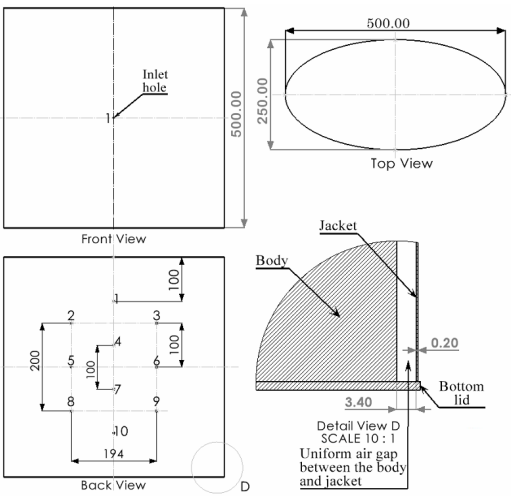

Fig. 1. Case 1: Model design with 11 ventilation holes [3].

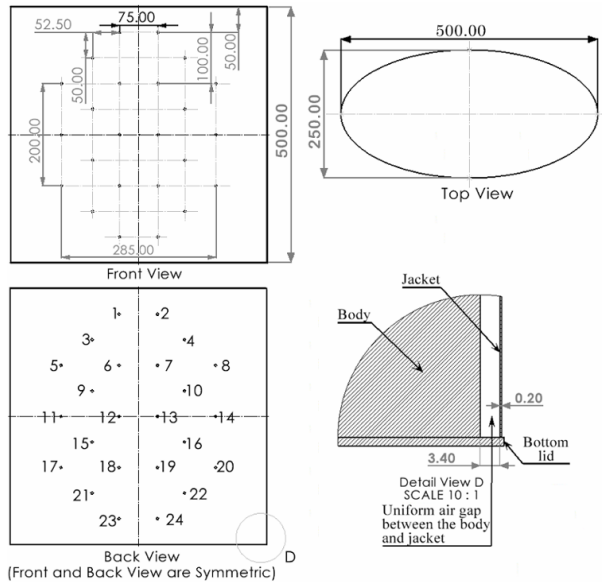

Fig. 2. Case 2: Model design with 48 ventilation holes.

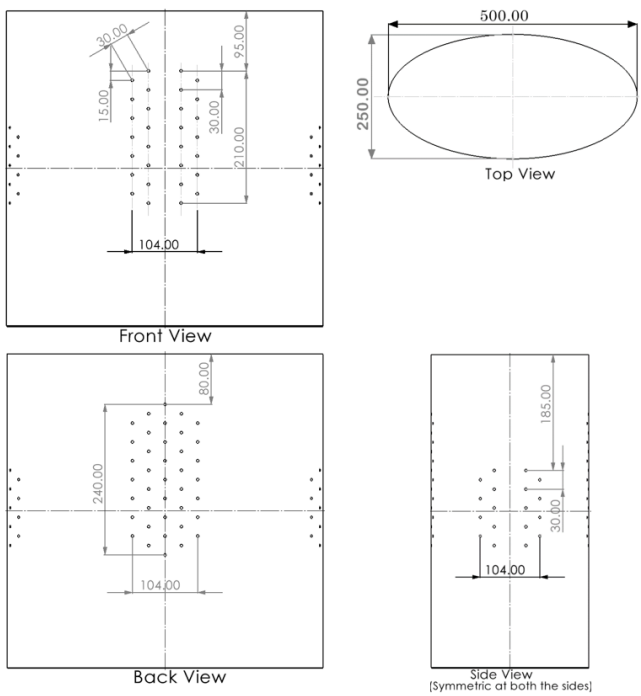

Fig. 3. Case 3: Model design with 105 ventilation holes.

For Cases 1 and 2, the model does not have any ventilation holes on the sides. However, in Case 3, there are a total of 18 ventilation holes on each side, as depicted in Fig. 3. The first 9 ventilations on each side are assigned as inlet boundary con-

ditions, while the remaining 9 on each side are designated as outlet boundary conditions. These nine elements on each side are also visible in the front and back views of Fig. 3.

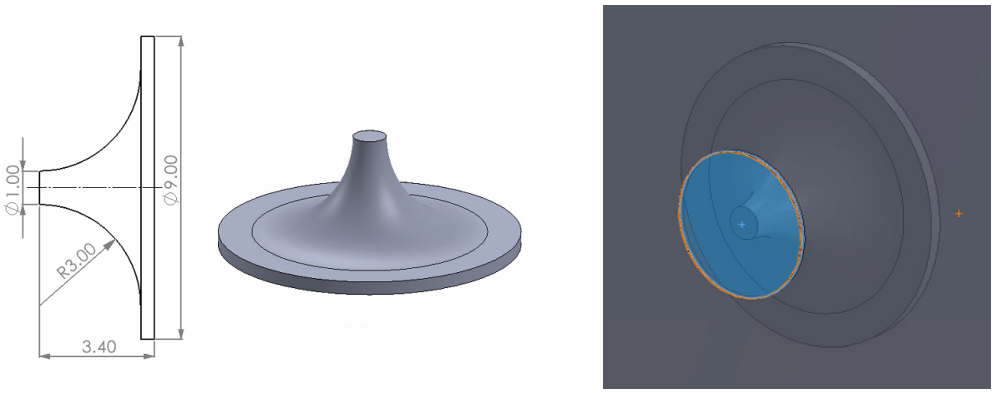

(**a**) (**b**)

Fig. 4. Ventilation element: (a) geometric dimensions of element; (b) position of ventilation element (highlighted orange circle shows ventilation hole).

The results are calculated using SolidWorks internal flow simulation tool. This study is transient, and the results are calculated for the physical time of 5 seconds. The flow simulation study uses standard settings, with an initial air temperature of 20 °C and an air pressure of 101325 Pa. The experiments are performed with an air velocity of 4 m/s, which is established as the inlet boundary condition. The airflow is perpendicular to the front surface of the model. The outlets located on the backside of the jacket are assigned to environmental pressure condition, which are designated as outlet boundary conditions. The average normal human body temperature is taken as 36.5 °C, while the amount of heat generated by the body during regular walking is considered to be 200 W [18], which is assigned to the body. Figure 5 shows the computational domain of the model, with the specified boundary conditions. In the simulation study, different materials with distinct properties are assigned to both the jacket and the body. Table 1 displays the material properties.

Table 1. Material Properties [19], [20]

Material property	**Human body**	**Jacket**
Average density [kg.m^{-3}]	985	1420
Specific heat [J.kg^{-1}.K^{-1}]	3500	1140
Thermal conductivity [W.m^{-1}.K^{-1}]	0.21	0.261

Assumptions considered in the simulation study are as follows:

- jacket is considered as air-tight, meaning that no air passes through the top and bottom parts;
- study does not take radiation into consideration, as the amount of heat lost through radiation will be equal in all circumstances;
- thermal energy transfers via conduction and convection from the body to jacket and then to the surrounding environment.

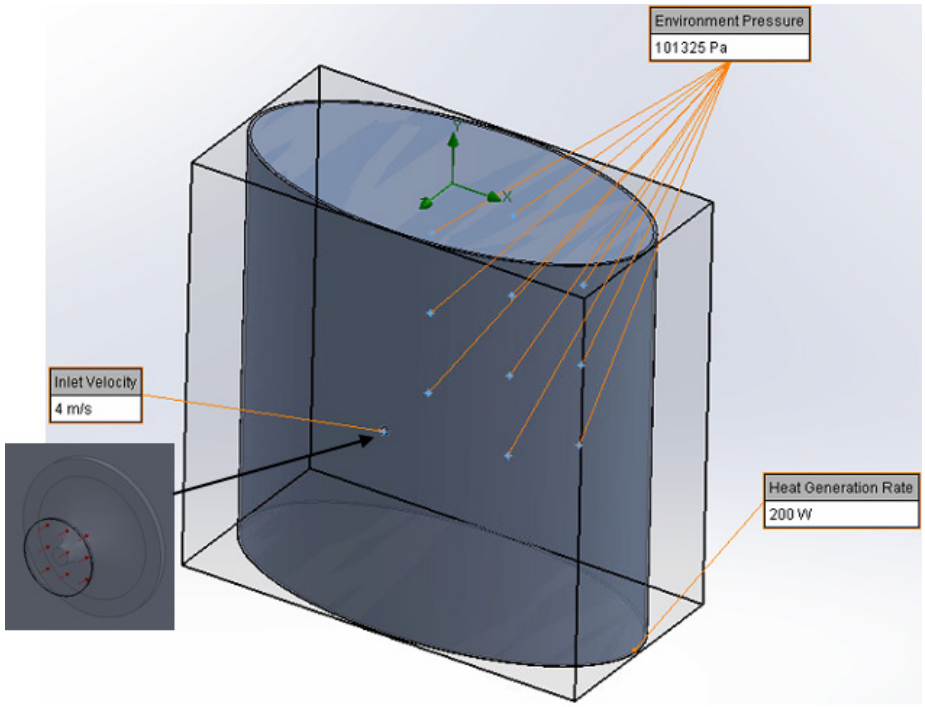

Fig. 5. Computational domain and boundary conditions in Case 1.

Figure 5 shows computational domain with set boundary conditions in Case 1. Inlet air of 4 m/s is visible at the front side, which enters into the air gap between the body and jacket and moves out through backside ventilations, which are assigned to environmental pressure. The heat generation rate of the body is set to 200 W. The same boundary conditions are assigned to model in Cases 2 and 3, the only difference is the numbers of inlet and outlet ventilation holes in each case. In this study basic mesh of size (Nx = 36, Ny = 36, Nz = 18) is utilised for the numerical simulation, as using fine mesh highly increases computational time. However, in this particular study, using fine mesh will not significantly impact the final outcome of finding appropriate criteria for cooling efficiency of protective clothing, as this study represents comparison of different criteria, using the same set of values in all three cases.

3. RESULTS AND DISCUSSION

The flow simulation study is set in SolidWorks for 5 seconds of physical time to obtain values of eight criteria mentioned in Table 2 below. Figure 6 shows the flow pressure and surface temperature plots for all three cases. The given pressure difference is measured in the air gap between the body and jacket. Air enters into this air gap through front inlet ventilations and moves out through outlet ventilations at the backside of jacket. The detail values of all the criteria obtained from the simulation studies are mentioned in Table 2.

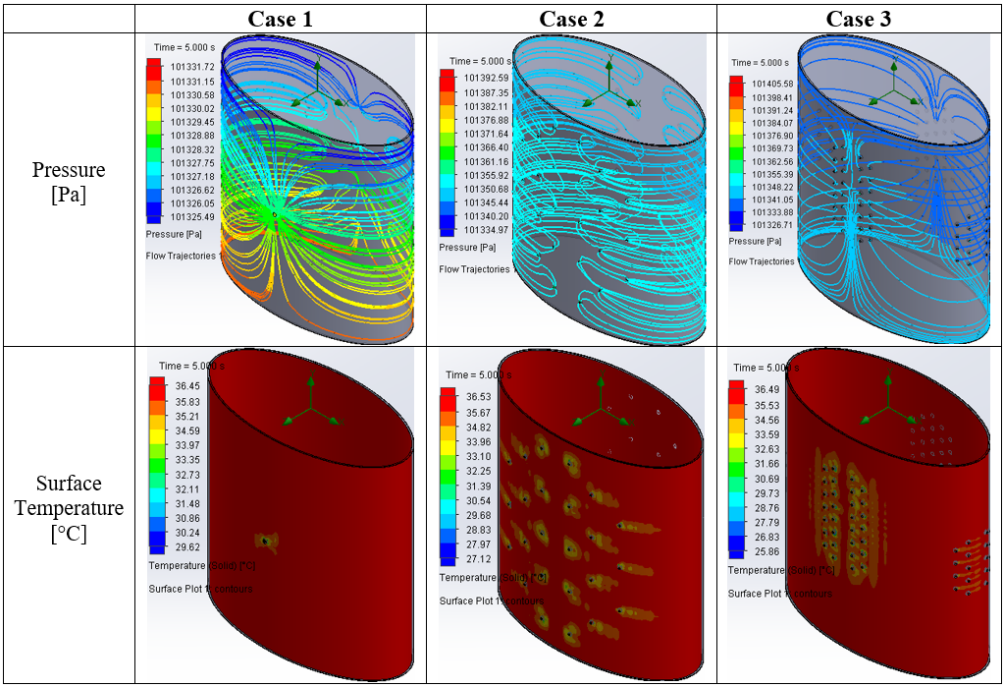

Fig. 6. Flow pressure and surface temperature plots in each case.

The surface temperature is determined by selecting surface of the body to observe how ventilation affects the temperature of body surface. The impact of ventilations on the surface body temperature for all three scenarios is shown in Fig. 6. The relative values of ΔP and ΔT are calculated based on the acquired results. The detail values of these parameters are provided in Table 2.

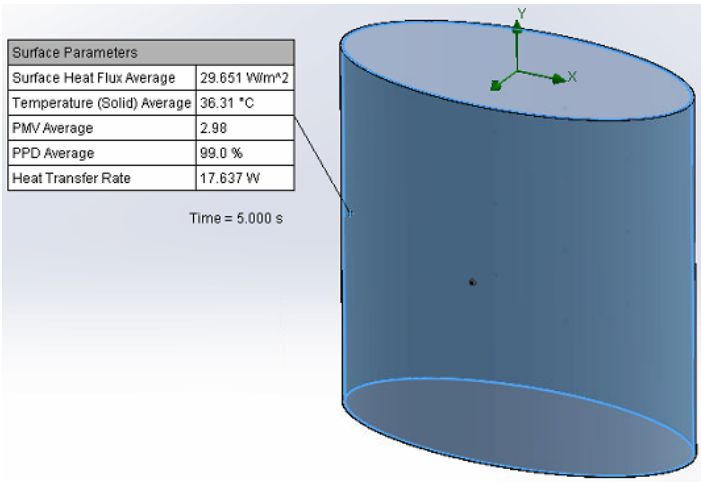

Fig. 7. Numerical values of criteria: HTR, HF, T (avg.), PMV and PPD in Case 1.

The values of the remaining criteria can be obtained using the surface parameter tool, which is available in the results section of SolidWorks flow simulation, as depicted in

Fig. 7. All these values are acquired in relation to surface of the body, except the criterion ΔH, which represents the heat transfer through ventilation holes rather than the body surface. This difference sets apart the HTR from ΔH. Thermal comfort in individuals can be assessed using the PMV and PPD. The PMV is a scale used to evaluate the thermal comfort experienced by individuals, indicating their perception of cold or warm temperatures. The 7-point thermal sensation scale used ranges from +3 (indicating hot) to -3 (indicating cold), with 0 representing a neutral temperature. The obtained specific values of these criteria for all three cases are indicated in Table 2.

Table 2. Numerical Values of the Analysed Criteria

Criteria	**Case 1**	**Case 2**	**Case 3**
HTR [W]	17.637	32.288	43.714
ΔH [W]	-1.021	-23.490	-43.140
HF (avg.) [W/m^2]	29.651	54.284	73.491
ΔP [Pa]	6.23	57.62	78.87
ΔT [°C]	6.83	9.41	10.63
T (avg.) [°C]	36.31	36.15	36.03
PMV (avg.)	2.98	2.95	2.93
PPD (avg.) [%]	99	98.8	98.5

From the examination of the results presented in Table 2, it is noticeable that all the criteria values show a gradual rise as the number of ventilations increases, with the exception of T (avg.), PMV, and PPD, which display an inverse trend. Moreover, these three criteria exhibit the least amount of variation when comparing the values of all three cases, as it can be noted from Table 2. This makes PVM, PPD, and T (avg.) less effective to accurately anticipate the system's efficiency, since the sensitivity of their values may further decrease when comparing two systems with a small number of ventilation difference. The comparison of results for other criteria in all three cases is illustrated in Figs. 8–12.

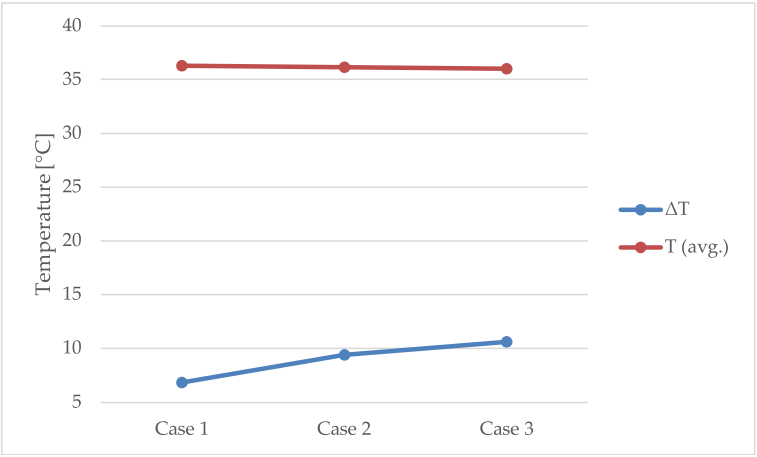

Fig. 8. Surface temperature of body in three cases.

The value of average temperature decreases with the increase in number of ventilations, which makes sense as with higher number of ventilation more heat can

transfer from the body that lowers body temperature. Moreover, with higher temperature difference, the value of average temperature decreases as the heat transfer rate increases with higher temperature difference. Though the sensitivity of average temperature obtained is very low as there is very small difference in the values, which may not be very useful in the analysis when there is a small difference in the number of ventilations. The same is true for PMV and PPD.

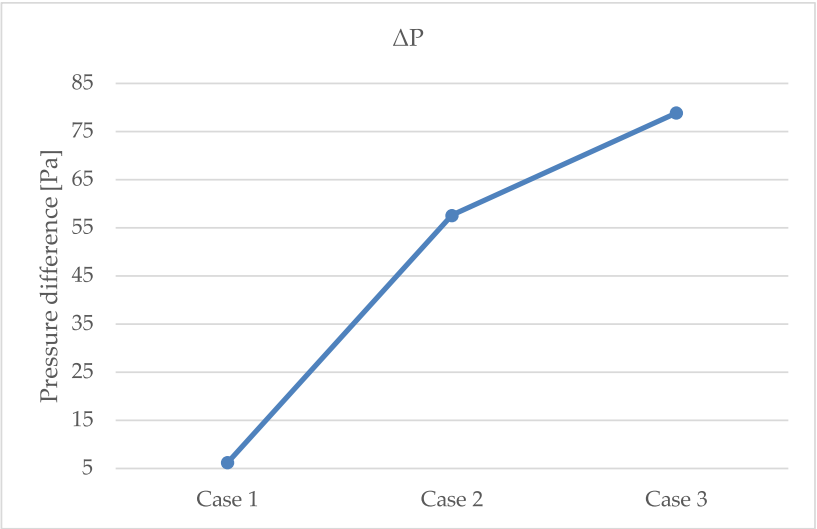

Fig. 9. Flow pressure in gap between the body and jacket in three cases.

Figure 9 shows that the pressure difference rises as the number of ventilations increases, and this provides a noticeable change in the values for three cases. While considering the pressure plots in Fig. 6, it does not offer significant insights into the cooling efficiency because the majority of pressure fluctuations occur at the ventilation openings in a very small area, particularly for Cases 2 and 3. Figure 10 (a) clearly illustrates that the maximum pressure, indicated by the red line, act in a very tiny region near the inlet, which may have a negligible effect or can be neglected. Moreover, the pressure difference values provided here are expressed in Pa, and according to the unit the difference between the measured values in all three cases are small to make any definitive conclusions on the cooling efficiency of the model based on these values. The same can also apply to temperature differences, where lower temperature occurs in a very small region that can be considered unimportant to provide any precise conclusion. This region is depicted by the dark blue colour in Fig. 10 (b). Consequently, relying on this small region may not yield an accurate measurement of the temperature difference, which may lead to incorrect conclusions.

In general, an increased temperature difference leads to higher heat transfer rate, which in turn enhances the efficacy of cooling. However, there are specific circumstances (such as discussed above) in which the region with the lowest temperature is negligible and thus cannot be regarded significant. Hence, it is critical to consider additional appropriate criteria in such circumstances to ensure the reliability of the results before making a final conclusion.

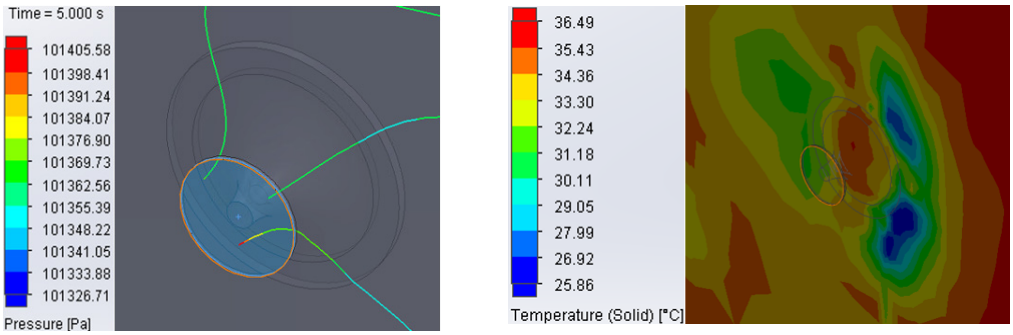

(**a**) (**b**)

Fig. 10. Pressure and surface temperature variation near ventilation hole:
(**a**) Flow pressure variation; (**b**) Surface temperature variation near ventilation hole.

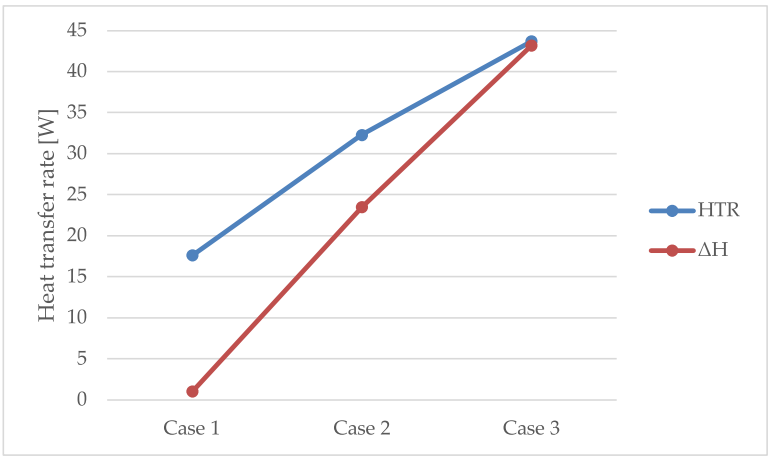

Fig. 11. Heat transfer rate in three cases.

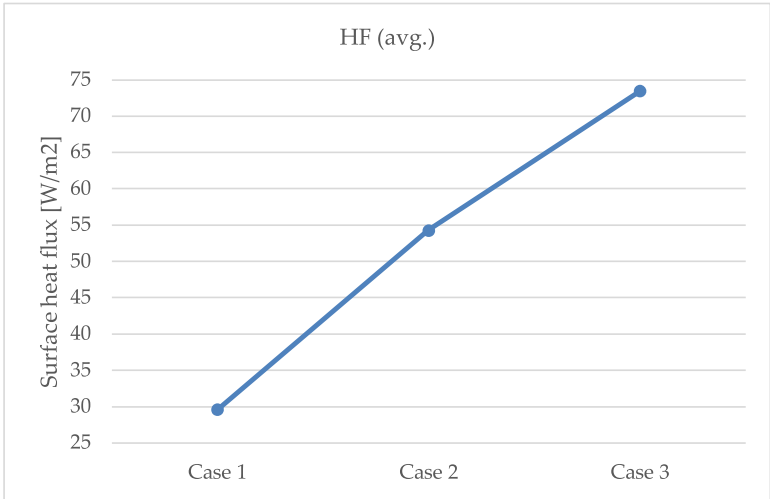

Fig. 12. Average surface heat flux of body in three cases.

The values of HTR, ΔH, and HF increase as the number of ventilation units increases. These values provide sufficient sensitivity for the analyses. However, ΔH only takes into account the area of heat transfer through ventilation holes and not the entire body surface. Thus, ΔH may not be the most suitable criterion compared to HTR and HF, which consider the overall heat transfer of the entire body surface. The main difference between HF and HTR is that HF provides surface heat flux per meter square area, whereas HTR provides the overall heat transfer rate of the body surface. Both of these criteria are very useful for predicting the cooling efficiency of the system and can be utilised based on specific requirements.

4. CONCLUSIONS

Based on the result analysis, it can be concluded that HTR (heat transfer rate) and HF (heat flux) are the most appropriate criteria for analysing the heat removal from the ventilated system (body with ventilated jacket) in the study. Since the goal is to predict cooling efficiency, either of the criteria can be helpful because cooling efficiency increases with an increase in heat transfer rate. While temperature difference can be following criteria for the analysis but in certain cases it might not provide enough sensitivity for the analyses, which is why it is better to use it in combination with other relevant criteria such as HTR or HF in this case to ensure the reliability of the results.

This study demonstrates variations in parameter values in CFD simulations in three different cases and identifies criteria that are helpful for forecasting cooling efficiency in the analysis. It is evident that certain criteria, such as flow pressure, may not be very useful in predicting cooling efficiency of the system. Moreover, parameters like average temperature, PMV and PPD can show less sensitivity in certain scenarios. In the future, it allows for the formulation of more realistic and complex CFD problems for ventilated protective clothing, taking into consideration uncertainty introduced, for instance, by varying wind direction and ventilation positions.

AUTHORS' CONTRIBUTIONS

Conceptualisation, S.R.V. and A.J.; methodology, S.R.V. and A.J.; software, S.R.V.; validation, I.V., and S.R.V.; formal analysis, S.R.V.; investigation, S.R.V.; data curation, S.R.V.; writing –original draft preparation, S.R.V.; writing – review and editing, I.V., S.R.V., A.J and I.V.; visualization, S.R.V. and I.V; project administration, S.R.V.; funding acquisition, S.R.V., A.J., and I.V. All authors have read and agreed to the published version of the manuscript.

ACKNOWLEDGEMENTS

This research/publication has been supported by the Doctoral Grant Programme of Riga Technical University.

NOMENCLATURE

1. HTR – Heat Transfer Rate of the body [W].
2. ΔH – Absolute Total Enthalpy Rate [W].
3. HF (avg.) – Surface Heat Flux of the body (average) [W/m^2].
4. ΔP – Flow Pressure Difference [Pa].
5. ΔT – Surface Temperature Difference of the body [°C].
6. T (avg.) – Average Surface Temperature of the body [°C].
7. PMV (avg.) – Predicted Mean Vote (average).
8. PPD (avg.) – Predicted Percentage Dissatisfied (average) [%].

REFERENCES

1. Wang, Y., & Cao, Z. (2017). Industrial Building Environment: Old Problem and New Challenge. *Indoor Built Environ*, *26*: 1035–1039.
2. Xu, C., & Liu, L. (2018). Personalized Ventilation: One Possible Solution for Airborne Infection Control in Highly Occupied Space? *Indoor Built Environ, 27*, 873–876.
3. Janushevskis, A., Vejanand S. R., & Gulevskis, A. (2022). Analysis of Different Shape Ventilation Elements for Protective Clothing. *WSEAS Transactions on Fluid Mechanics, 17*, 140–146.
4. Barry, J., Hill, R., Brasser, P., Sobera, M., Kleijn, C.R., & Gibson, P. W. (2003). Computational Fluid Dynamics Modeling of Fabric Systems for Intelligent Garment Design. *MRS Bulletin,* 28 (08).
5. Udayraj, B. C. (2022). A Coupled CFD-Thermoregulation Model for Air Ventilation Clothing. *Journal of Energy and Buildings, 268*, 112206.
6. Epstein, Y., Shapiro, Y., & Brill, S. (2010). Comparison between Different Auxiliary Cooling Devices in a Severe Hot/Dry Climate. *Ergonomics, 29* (1), 41–48.
7. Pasut, W., Zhang, H., Arens, E., & Zhai, Y. (2015). Energy-efficient Comfort with a Heated/Cooled Chair: Results from Human Subject Tests. *Building and Environment, 84*, 10–21.
8. Lopez, G., Tokuda, T., Isoyama, N., Hosaka, H., & Itao, K. (2016). Development of a Wrist-Band Type Device for Low-Energy Consumption and Personalized Thermal Comfort. *MECATRONICS 2016/17th Int. Conf. Res. Educ. Mechatronics*, 209–212.
9. He, Y., Li, N., He, M., & He, D. (2017). Using Radiant Cooling Desk for Maintaining Comfort in Hot Environment. *Energy and Buildings, 145*, 144–154.
10. Huang, L., Ouyang, Q., Zhu, Y., & Jiang, L. (2013). A Study about the Demand for Air Movement in Warm Environment. *Building and Environment, 61*, 27–33.
11. Udayraj, Wang, F., Song, W., Ke, Y., Xu, P., Chow, C. W. S., & Noor, N. (2019). Performance Enhancement of Hybrid Personal Cooling Clothing in a Hot Environment: PCM Cooling Energy Management with Additional Insulation. *Ergonomics, 62* (7), 928–939.
12. Mneimneh, F., Ghaddar, N., Ghali, K., & Itani, M. (2021). The Effectiveness of Evaporative Cooling Vest with Ventilation Fans on the Thermal State of Persons with Paraplegia during Exercise. *Building and Environment, 206*, 108356.
13. Xu, P., Kang, Z., Wang, F., & Udayraj. (2020). A Numerical Analysis of the Cooling Performance of a Hybrid Personal Cooling System (HPCS): Effects of Ambient Temperature and Relative Humidity. *International Journal of Environmental Research and Public Health, 17* (14), 4995.

14. Wang, F., Ke, Y., Udayraj, Yang, B., Xu, P., & Noor, N. (2020). Effect of Cooling Strategies on Overall Performance of a Hybrid Personal Cooling System Incorporated with Phase Change Materials (PCMs) and Electric Fans. *Journal of Thermal Biology, 92*, 102655.
15. Watkins, S.M. (1995). *Clothing: The Portable Environment* (2nd ed.). Iowa State University Press.
16. Lim, J., Choi, H., Roh, E. K., Yoo, H., & Kim, E. (2015). Assessment of Airflow and Microclimate for the Running Wear Jacket with Slits Using CFD Simulation. *Fashion and Textiles*, *2*, 1.
17. Janushevskis, A., Vejanand, S. R., & Gulevskis, A. (2023). Shape Optimization of Ventilation Elements for Protective Clothing by Using Metamodeling Approach. *22th International Scientific Conference Engineering for Rural Development, 23*, 164–172.
18. Kumar, R., Aggarwal, R.K., Sharma, J.D., & Pathania, S. (2012). Predicting Energy Requirement for Cooling the Building Using Artificial Network. *Journal of Technology Innovations in Renewable Energy, 1* (2), 113–121.
19. Janushevskis, A., Vejanand, S. R., & Gulevskis, A. (2022). Comparative Analysis of Different Shape Ventilation Elements for Protective Clothing. *Engineering for Rural Development,* Jelgava, 25–27 May 2022.
20. Giering, K., Lamprecht, I., & Minet, O. (1996). Specific Heat Capacities of Human and Animal Tissues. *Proceedings of SPIE – The International Society for Optical Engineering*, *2624*, 188–197.

sciendo

LATVIAN JOURNAL OF PHYSICS
AND TECHNICAL SCIENCES
2025, N 2

DOI: 10.2478/lpts-2025-0011

A COMPARATIVE STUDY OF PROPERTY MEASUREMENT FOR ZnO-THIN FILM GROWTH PROCESSES USING HYDROCLORIC ACID (HCl) AND WATER (H_2O) SOLUTION-DEPENDENT ON NOVEL ELECTROSTATIC SPRAY DEPOSITION (ESD)

F. I. Abbas[1,2,3*], M. Sugiyama[1,4]

[1] Department of Electrical Engineering,
Tokyo University of Science,
2641 Yamazaki, Noda, Chiba 278-8510, JAPAN
[2]Department of Theoretical Physics,
University of Dhaka,
Dhaka-1000, BANGLADESH
[3] Department of Electrical Engineering,
City University,
Savar, Birulia, Dhaka, 1216, BANGLADESH
[4]Research Institute for Science and Technology,
Tokyo University of Science,
2641 Yamazaki, Noda-shi, Chiba-ken, 278-8510, JAPAN
*e-mail: fysolibnaabbas1988@gmail.com

This investigation has been carried out utilising the innovative ESD technique for six ZnO nano polycrystalline (NP) samples. The Debye-Scherer model (DSD) is used to study the mechanical elastic properties (MEP) as lattice dislocation density (δ) and the lattice strain (ε %) contribution to the X-ray diffraction line broadening in nanocrystalline ZnO thin film. The average size of the crystallites was determined to be approximately 48 nm. When studying the phenomenon of line broadening, it is critical to take into account MEP anisotropy. This is necessary in order to effectively distinguish between the influences of strain and particle size. The novel ESD technique promotes ZnO growth mechanisms by adding small amounts of HCl into spray solutions on conductive In_2O_3:Sn (ITiO)-coated alkali-free glass substrates while changing the water (H_2O) ratio. XRD pattern characterisation revealed the preferred orientation of

the (002) planes in ZnO thin films. This study represents a significant advancement in the easy understanding of the ZnO growth mechanism and the changes in MEP enabled by ESD-deposited thin film in cost-effective industrial and commercial applications of electronics.

Keywords: *ESD, Debye–Scherrer method, lattice dislocation density, lattice strain, ZnO growth mechanism.*

1. INTRODUCTION

Zinc oxide (ZnO) nanostructure semiconductors have attracted considerable attention in research due to their potential applications in diverse fields such as solar cells [1], light-emitting diodes [2], photocatalysis [3], and so on. However, novel semiconductor materials frequently use strain as a design parameter to increase electron mobility [4]. This phenomenon is now used in a number of applications, including strained metal-oxide semiconductor field-effect transistors (MOSFETs) [5] and piezoelectric resistors [6]. The incorporation of lattice defects intricately links the functionality of semiconductor materials and devices [7]. Their appearance and ability to move around make things less effective and more likely to break after a while of use [8]. Commonly used techniques for creating ZnO thin films include dry methods such as sputtering [9] and pulsed laser deposition [10], as well as wet methods such as chemical bath deposition [11], mist chemical vapor deposition [12], and spray pyrolysis [13].

Additionally, the ESD method is not only easy to use, but it also has important industrial benefits, such as the ability to cover large areas because it is simple and straightforward to understand. This technique allows for non-vacuum deposition, has a low cost, and provides convenient control over the composition ratio and doping [14]. These advantages should lead to the development of inexpensive and simple electronic devices that can transmit visible light without obstruction using the ESD technique. Recently, there has been a dearth of research projects and papers that specifically examine the growth mechanism of oxide-based semiconductors using the ESD approach [14] and concentrate on the chosen solution. Characterisation using the ESD approach is essential for comparing the results with other techniques.

This study aims at investigating the effects of sequential additions of 0.005M and 0.015M HCl, using the ESD method, on the growth process of ZnO, taking into account any changes in mechanical behaviour. The ESD method is used on six different ITiO glass substrates at three different temperatures: 300 °C, 400 °C, and 500 °C, by varying the H_2O ratio in the precursor solutions. In this case, $ZnCl_2$ is used as a starting material and dissolved in CH_3CH_2OH at a concentration of 0.1 M. The experimental sections mention the detailed preparation method for spray solutions. Furthermore, nanoscale-level studies are the focus for how behaviour is changing and affected by ESD with ZnO growth processes. This study represents the initial phase in the development of affordable and uncomplicated devices that are transparent to visible light.

Table 1. Typical Deposition Parameters and Conditions for ESD

S. no.	Parameter	Value
1.	Distance between the nozzle aperture and the hot plate	3.5 cm
2.	Flow rate	2.0 ml/h
3.	Deposition time	5 min
4.	Applied voltage	8 kV

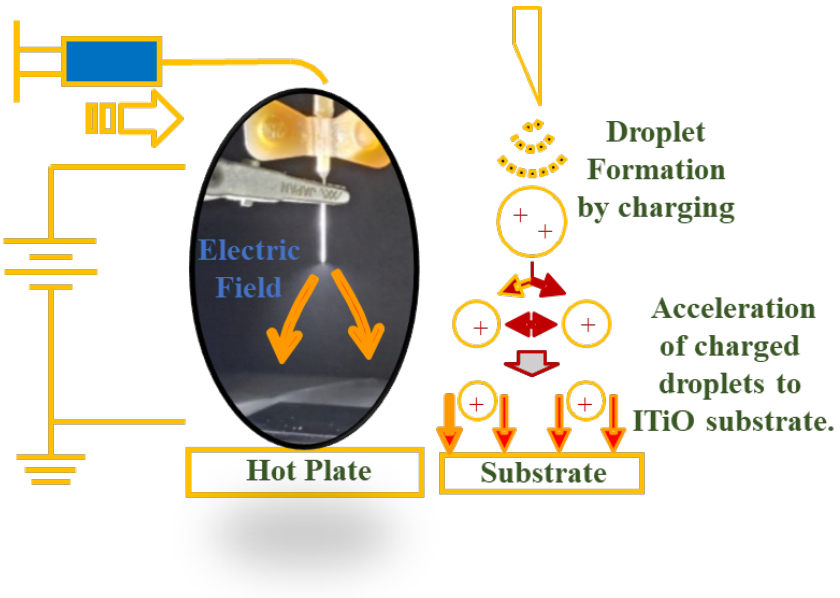

Fig. 1. F. I. Abbas, *Latvian Journal of Physics and Technical Sciences*: Schematic diagram of ESD.

2. EXPERIMENTAL METHODS

The zinc sources used in this study were $ZnCl_2$ (98% Assay, $ZnCl_2$=136.32), Lot. LEH7398, Mfg. Date. 2021.09, FUJIFILM Wako Pure Chemical Corporation). The solutes were ethanol (CH_3CH_2OH (99.5), Cat. No. 14033-70, FW: 46.07, KANTO CHEMICAL CO, INC), and deionized water (H_2O). ZnO films were deposited using ESD on a conductive In_2O_3:Sn (ITiO) coated alkali-free glass substrate. The experimental diagram of ESD is shown in Fig. 1. 20 ml of six (6) different spray solutions were prepared with changing the H_2O ration, and HCl concentrations for the ESD spray technique.

To prepare the ESD solution with 0% of H_2O and a concentration of 0.1 M, separately, 20 ml of CH_3CH_2OH was measured and placed in two glass beakers. The density of CH_3CH_2OH was 0.78945 g/cm^3. Then 0.2726 g $ZnCl_2$ was added with the CH_3CH_2OH in the glass beaker. Then we introduced distinct solutions of HCl at concentrations of 0.005 M and 0.015 M into the ESD solutions, respectively. To make the solution homogeneous, it was heated up

to 20 minutes in the magnetic stirrer with hot plate (ADVANTEC SR/350) (Fig-1 (c)). The temperature was considered to be 150 °C for the magnetic stirrer with hot plate. Similarly, two separate glass beakers were used to prepare the second type ESD spray solutions, which consisted of 80 % CH_3CH_2OH (16 ml) and 20 % H_2O (4 ml), respectively. Next, the same amount of $ZnCl_2$ was added to the separate glass beakers along with 16 ml of CH_3CH_2OH. The same procedures were applied for mixing the 0.005 M and 0.015 M HCl concentrations, and the homogeneous spray solution was prepared. For the third type of ESD spray solution, 50 % CH_3CH_2OH (10 ml of CH_3CH_2OH) and, 50 % H_2O (10 ml of the same procedures were applied for the mixing of the 0.005 M and 0.015 M HCl concentrations, and the homogeneous spray solution was prepared, respectively.

ESD spray was performed for 5 minutes at a solution flow rate of 2.0 ml/h on the substrate surface, and voltage was applied between nozzle and substrate of 8 kV during spraying. Followed by ESD temperature ranged from 300 °C, 400 °C, and 500 °C in air for 5 minutes. For the simplification and understanding the ESD technique, the parameters are listed in Table.1 The crystallographic orientations of the ZnO films were evaluated using X-ray diffraction (XRD; Rigaku Ultima IV, Rigaku SmartLab). MEP of ZnO thin films was investigated using DSD, which was correlated to the basic crystal growth mechanism [15]–[22], by the novel ESD method. The equations involved in this estimation are given below (1)–(3) [15], [20].

$$D = \frac{0.9\,\lambda}{\beta\cos\theta}\mathrm{X}, \tag{1}$$

$$\delta = \frac{1}{D^2}, \tag{2}$$

$$\varepsilon = \frac{\beta_G \cos\theta}{4\sin\theta}, \tag{3}$$

where D, λ, θ, β are crystallite, lambda as the wavelength (1.54 Å), theta as angle (diffraction angle), beta as angle (in radian), respectively.

3. RESULTS AND DISCUSSION

3.1. The XRD Analysis

The XRD experiment was conducted to analyse the structural properties of the ZnO thin film growth mechanism utilising the ESD technique at temperatures of 300 °C, 400 °C, and 500 °C, respectively. Six distinct spray solutions were prepared by dissolving $ZnCl_2$ in CH_3CH_2OH at a concentration of 0.1 M. These solutions were used to investigate the impact of 0.005M and 0.015M HCl on the growth mechanism of ZnO thin films using the ESD method. The H_2O ratio was varied during the experiments. The XRD pattern of the ZnO thin films on an In_2O_3:Sn (ITiO)-coated alkali-free glass substrate is shown in Fig. 2 (a–c), and 2(d–f), for the 0.005M and 0.015M HCl, with varying H_2O rations of 0 %, 20 %, and 50 %, respectively. Figures 2(a) and 2(d) are for 0.005M HCl and 0.015M HCl mixing without the H_2O in the spray solution, respectively. Figure 2 (a) exhibits strong peaks at the (002), and (102) planes. This peak observation

clearly confirms the ZnO thin film growth, without the H_2O mixing into the solution at a concentration of 0.005M HCl. Figure 2(d) also observed a pattern at (002) plane for the ESD spray solution with a 0.015M HCl concentration. Figure 2(d) shows that the peak strength at 500 °C is stronger in the (002) plane compared to the 0.005M HCl solution.

Figures 2 (b) and 2(e) showed the results for 0.005M and 0.015M HCl in the spray solution with a 20 % H_2O ratio, respectively. The peak intensities reveal the appearance of the (002), and (102) planes for the 0.005M HCl added ESD solution at 500 °C ESD performing temperature. However, for the 0.015M HCl solution peak is only seen at (100) plane, which is very weak at 300 °C, 400 °C, and 500 °C, respectively. In addition, the peak at (002) plane is only for 400 °C ESD temperature. In Fig. 2(b), the 0.005 M HCl solution has a stronger peak intensity in the (002) plane at 500 °C than the 0.005 M HCl solution shown in Fig. 2(a). Surprisingly, in Fig. 2(e) for the high-concentration HCl solution of 0.015 M, the peak for the (002) plane at 500 °C has not appeared. This may be due to the complex formation effect in the spray solution caused by H_2O and the high concentration of acid at that temperature [23]. The results for 0.005M and 0.015M HCl in the spray solution with a 50 % H_2O ratio are shown in Figs. 2(c) and 2(f) in sequential order. For 0.005M HCl case, the peak intensities indicate the presence of the (100), (002), (101), and (102) planes where the strong peak appears at (002) plane for 500 °C, ESD performing temperature and weak peak at (102) plane. On the other hand, (100), (102) plane for 400 °C is slightly stronger compared to 20% H_20 ratio ESD sample at 400 °C. For 300 °C, very weak peak intensities were found at (100) and (102) planes. Compared to Figs. 2(a) and 2(b), Figure 2(c) shows a higher peak intensity in the (002) plane at 500 °C for the 0.005 M HCl solution. This behaviour occurs gradually as the H_2O ratio increases in the spray solution with a low-concentration 0.005M HCl. The peak intensity in the (100) plane for the 0.015M HCl solution for both the 50 % and 20 % H_2O ratios has shown very small change. These behaviours can be understood to analyse the results with basic crystal theory [20], [21]. In the following section, it will be discussed elaborately.

Figure 2 (a–c) displays a sequence of successive and gradually increasing peak intensities, which correlate to the formation of ZnO thin films. These peaks were observed at a diffraction angle of around 34.80° for samples containing 0.005 M of HCl, using the ESD method at a temperature of 500 °C. Peaks at the (100) and (102) planes showed low intensities in the range of 300 °C–400 °C, but the appearance of the (002) plane in the observation confirmed the fabrication of ZnO thin films with a hexagonal wurtzite structure [15]. However, Fig. 2 (d–f) for the 0.015M HCl mixing results clearly shows the peaks for the (002) plane. The 20 % H_2O ratio samples exhibit sudden drops in peak intensity. The peaks in the (002) plane are once again prominent for the 0.015 M HCl mixing samples with a 50 % H_2O ratio. Also, the peak intensity for the (100) plane is a little higher for the samples mixed with 0.015 M HCl than for the samples mixed with 0.005 M HCl from the ESD at the temperature ranges that were studied. However, the (002) plane consistently shows rising peak intensity results for the 0.005M of HCl mixing samples, indicating the gradual growth of the ZnO thin film. The XRD results in Fig. 2(a–c) showed that all of the thin films that were deposited had a clear orientation along the c-axis (002) plane and a slightly stronger peak along the (102) plane corresponding

to the ZnO thin film growth. Increasing the temperatures as well as the film thickness of ESD-produced films results in a sharper and more intense (002) plane of diffraction peak [14], accompanied by a decrease in the full width at half maximum (FWHM). According to the fundamental theory, the growth of ZnO thin films is determined by the c-axis orientation [20], [21]. This theory asserts that the (002) plane of ZnO possesses the lowest surface energy, which plays a crucial role in determining the crystal structure.

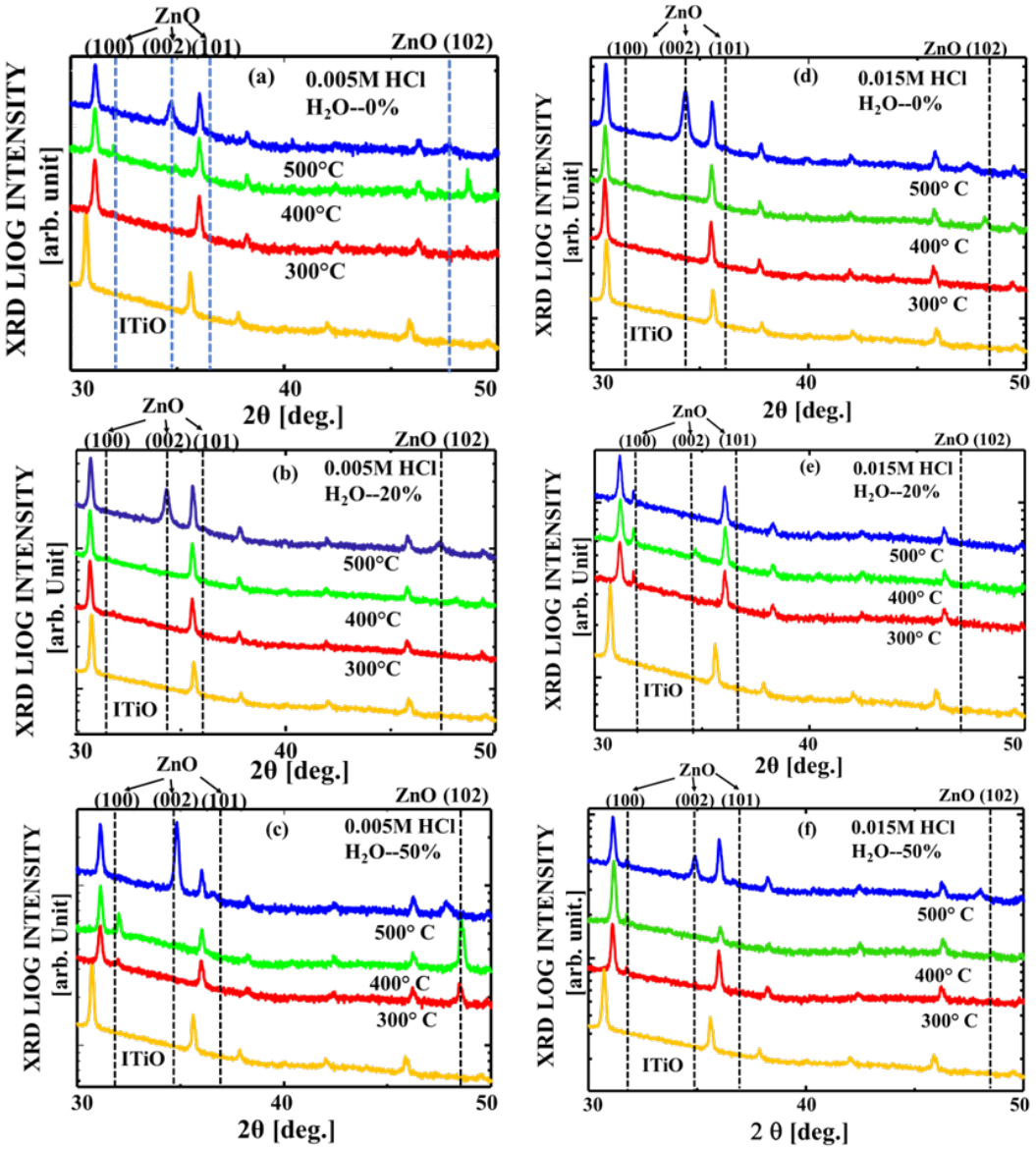

Fig. 2. F. I. Abbas, *Latvian Journal of Physics and Technical Sciences:* XRD patterns of ZnO film according to (a–c) 0.005M HCl, and (d–f) 0.015M HCl weight ratio of H_2O/solvent in the solution deposited by ESD at 300 °C, 400 °C and 500 °C, respectively.

3.2. ESD TEMPERATURE EFFECT ON MEP

A key factor in determining the MEP of thin film materials is δ (*10^{18} m^2), which is the principal method of plastic deformation in these materials. The investigation of the correlation between dislocation behaviour and mechanical reaction has been an important focus of extensive research ever since Taylor initially proposed the concept of dislocation in 1934 [24]. Dislocations play a critical role in determining the mechanical characteristics of materials by influencing the microstructure development. Figures 3 (a–c) and 3 (d–f) show a more detailed look at the ZnO nanoparticle growth mechanism from the mechanical point of view, changing the concentration of the ESD process.

Figures 3(a, b) and 3(d, e) show the results of δ (*10^{18} m^2) for 0.005 M HCl and 0.015 M HCl of the ESD spray solution for 0 % and 20 % H_2O ratio, respectively. These figures show a constantly decreasing trend for δ (*10^{18} m^2) over the entire temperature range of 300 °C to 500 °C. On the other hand, Figs. 3(c) and 3(f) represent the result for δ (*10^{18} m^2) for a 50 % H_2O ratio in the ESD spray technique. In Fig. 3(c), the δ (*10^{18} m^2) increases from 300 °C to 400 °C, and then it decreases from 400 °C to 500 °C. Comparing, in Fig. 3(f), the δ (*10^{18} m^2) decreases from 300 °C to 400 °C, and then it starts increasing from 400 °C to 500 °C.

From the physical point of view, in Fig. 3. (a, b), 0 % and 20 % H_2O ratio mixed sample shows a consecutive and gradually decreasing nature of δ (*10^{18} m^2) for the 0.005 M HCl of the ESD spray sample. This indicates the stabilisation mode of the thin film growth during the ESD process in the micro-level state. Similar behaviour is also observed for the 0 % and 20 % H_2O ratio ESD sample for 0.015 M HCl. However, for the 50 % H_2O ratio (Fig. 3. (c)), rapid increasing and then then decreasing nature were found, which indicated the non-isotropic behaviour of the 0.005 M HCl. Perhaps, this non-isotropic nature is related to the complex formation of the small acid and large H_2O ratio of the ESD sample.

Importantly, the 50 % H_2O ratio with the 0.015 M HCl showed decreasing results from 300 °C to 400 °C and then increasing results found from 400 °C to 500 °C, which was similar to the isotropic in nature. Comparing the results with a 50 % H_2O ratio to 0.005 M HCl, this indicates that low concentrations of HCl mixed ESD spray samples are showing non-isotropic behaviour and high concentrations of HCl samples are showing isotropic behaviour. This dynamic behaviour is very essential for the growth of ZnO thin film on the ITIO substrate surface.

The study of crystal lattice strain, ε (%) is of utmost significance in the field of semiconductor materials and devices. When designing new semiconductor materials, strain is often used as a design feature to make it easier for electrons to move around [24]. Bardeen and Shockley initially emphasised the significant influence of mechanical phenomena in the field of semiconductor physics [25]. Figure 4 (a–c) presents a detailed analysis of the efficiency ε (%), of the ZnO nanoparticles in the ZnO thin film investigated in this study. The analysis focuses on the 0.005M concentration with different H_2O ratios of 0 %, 20 %, and 50 % in the ESD. Figure 4(a, b) consistently showed an increasing trend for ε (%), across the entire temperature range from 300 °C to 500 °C. Besides, Fig. 4(c) represents the result of ε (%), for a 50 % H_2O ratio in the ESD spray technique. Here, in the 300 °C to 400 °C temperature range, ε (%), starts to decrease, then from 400 °C to 500 °C it increases. Remarkably, the behaviour

of this sample is highly dynamic despite a small quantity of HCl being mixed. The dynamic nature of this process facilitates the advancement of ZnO thin film technology through the innovative ESD approach.

Furthermore, Fig. 4 (d–f) demonstrates the responses of ESD spray solution samples with varying H_2O ratios when mixed with 0.015 M HCl. In Fig. 4 (d–f), very small change in the ε (%), behaviour was found. This behaviour may be regarded as stiff features for the highly concentrated acid solution [26]. It is possible that the inflexible strategy for distorting the crystal lattice suggests that the large amount of HCl in the sample does not facilitate ZnO formation through the ESD mechanism. The limited quantity of HCl may be deemed appropriate for facilitating the growth mechanism of zinc oxide thin film by altering the H_2O ratio in the ESD technology. Further research is required to understand the mechanism of thin film growth and its fundamentally changing nature, using the convenient and innovative ESD technique for the development of semiconductor studies.

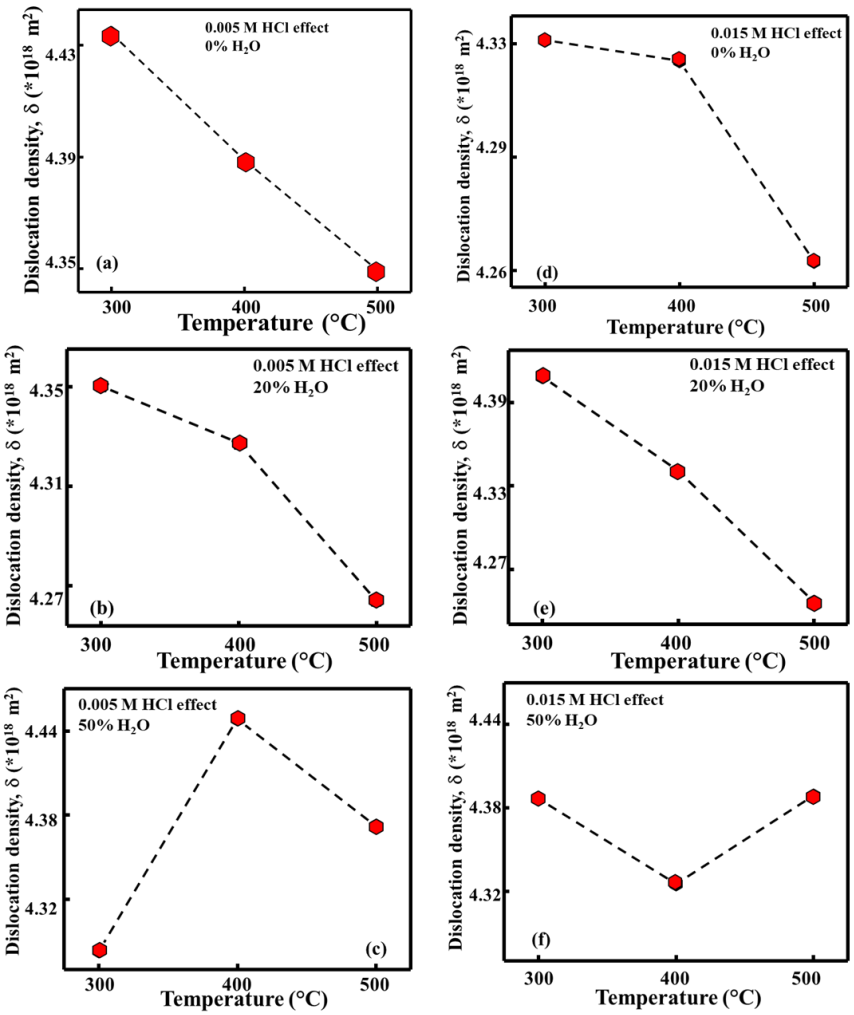

Fig. 3. F. I. Abbas, *Latvian Journal of Physics and Technical Sciences:* Dislocation density, δ (*10^{18} m^2) of ZnO film according to (a–c) 0.005M HCl, and (d–f) 0.015M HCl weight ratio of H_2O/solvent in the solution deposited by ESD at 300 °C, 400 °C and 500 °C, respectively.

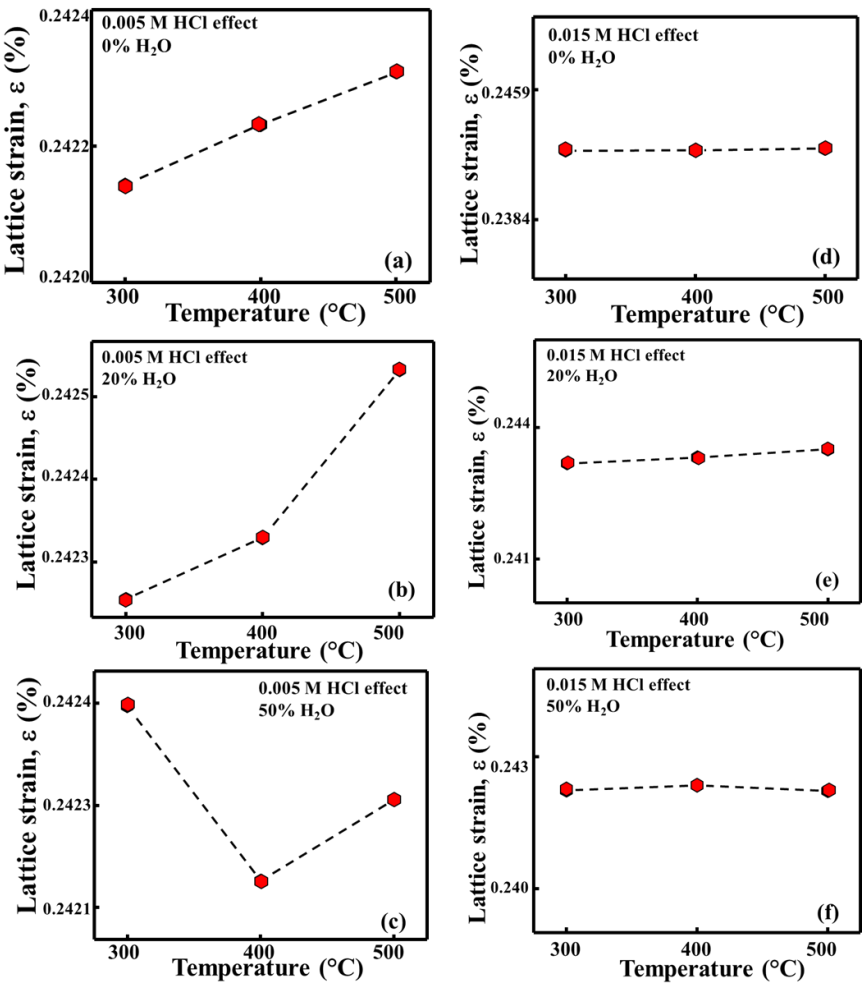

Fig. 4. F. I. Abbas, *Latvian Journal of Physics and Technical Sciences:* Lattice strain, ε (%) of ZnO film according to (a –c) 0.005M HCl, and (d–f) 0.015M HCl weight ratio of H_2O/solvent in the solution deposited by ESD at 300 °C, 400 °C and 500 °C, respectively.

Finally, this study investigated the HCl acid mixed solution-dependent growth mechanism of ZnO semiconductor thin film by varying the H_2O ratio solution through the novel ESD method on a conductive In_2O_3:Sn (ITiO)-coated alkali-free glass substrate from the temperature range of 300 °C, 400 °C, 500 °C. Compared to other dry processes [9], [10], and wet processes [11]–[13], crystal quality is not very high, and XRD analysis shows that adding a little HCl (0.005 M) makes the growth process enhancement of ZnO thin films made with the novel ESD technology quantitatively good. In the area of a defect (dislocation) is elastically distorted (strained). Elastic fields cause the diffraction peaks to broaden. This phenomenon is sometimes referred to as microstrain and is contingent upon the presence of non-uniform lattice distortions. Here, it is also found that there is a possible correlation with the growth mechanism and the MEP by ESD.

Still, the results obtained from this study of ZnO thin film growth mechanism were quantitatively good in agreement to consider the cost effectiveness. This method can also be used for other purposes of semiconductor thin films growth mechanism study. Further investigation on other microstructural properties is also needed for clear visualisation on ZnO growth mechanism by the novel ESD technique. For our upcoming study, we will further explore the structural characteristics of this research.

4. CONCLUSIONS

This study found that ESD can develop the oxide-based semiconductor thin film growth technique cost-effectively. The possible correlation between the growth mechanism of semiconductor thin films and their MEP can be easily realised. Importantly, future studies on thin-film semiconductor growth mechanisms may apply using the ESD method.

Altogether, these findings indicate that employing ESD for depositing the ZnO film is advantageous for creating stacked thin film devices. This study is important as it is the primary stage in developing cost-effective and uncomplicated devices that are transparent to visible light using the ESD method for semiconductor oxide-based materials.

ACKONWLEDGEMENTS

The authors express their sincere appreciation to Mr. Keisuke Tomono, Mr. Keito Okubo, and Mr. Kohta Hori for their support in completing the experiments and for the constructive discussions. The research has been sponsored by MEXT for the scholarship of supporting international student (Fysol Ibna Abbas), JSPS KAKENHI (Grant number: 21K04696), and the Renewable Energy Science and Technology Research Division of the Tokyo University of Science.

REFERENCES

1. Bitenc, M., & Orel, C. (2009). Synthesis and Characterization of Crystalline Hexagonal Bipods of Zinc Oxide. *Mat. Res. Bulletin, 44* (2), 381–387. DOI:10.1016/j.materresbull.2008.05.005
2. Choi, Y., Kang, J., Hwang, D., & Park, S. (2010). Recent Advances in ZnO-Based Light-Emitting Diodes. *IEEE. Trans. Elec. Devices,* 57 (1), 26-41. DOI:10.1109/TED.2009.2033769
3. Baruah, S., & Dutta, J. (2009). Hydrothermal Growth of ZnO Nanostructures. *Sci. Tech. Advan. Materials, 10* (1), 013001(1–18). DOI:10.1088/1468-6996/10/1/013001
4. Dolabella, S., Borzì, A., Dommann, A., & Neels, A. (2022). Lattice Strain and Defects Analysis in Nanostructured Semiconductor Materials and Devices by High-Resolution X-Ray Diffraction: Theoretical and Practical Aspects. *Small Methods, 6* (2), 1-31. DOI:10.1002/smtd.202100932
5. Zhu, L., & Zeng, Z. (2017). Room-Temperature Gas Sensing of ZnO-Based Gas Sensor: A Review. *Sensors and Act. A: Physical, 267,* 242–261. DOI:10.1016/j.sna.2017.10.021

6. Alim, A., Fonoberov, V., & Balandin, A. (2005). Origin of the Optical Phonon Frequency Shifts in Quantum Dots. *Appl. Phys. Lett., 86* (5), 053103(1–3). DOI:10.1063/1.1861509
7. Tennyson, E. M., Doherty, T. A. S., & Stranks, S. D. (2019). Heterogeneity at Multiple Length Scales in Halide Perovskite Semiconductors. *Nat. Rev. Mater., 4*, 573–587.
8. Ram, S. D. G., Kulandainathan, M. A., & Ravi, G. (2010). Aqueous Chemical Growth of Free Standing Vertical ZnO Nanoprisms, Nanorods and Nanodiskettes with Improved Texture Coefficient and Tunable Size Uniformity, *Appl. Phys. A,* 105, 881–890. DOI:10.1007/s00339-011-6518-6
9. Ada, K., Goekgoez, M., Oenal, M., & Sankaya, Y. (2008). Preparation and Characterization of a ZnO Powder with the Hexagonal Plate Particles. *Powder Technology, 181*, 285–291. DOI:10.1016/j.powtec.2007.05.015
10. Thomas, D. G. (1960). The Exciton Spectrum of Zinc Oxide. *J. Phys. Che. Solids, 15* (1–2), 86–96. DOI:10.1016/0022-3697(60)90104-9
11. Nakai, H., Sugiyama, M., & Chichibu, S. F. (2017). Ultraviolet Light-Absorbing and Emitting Diodes Consisting of a p-type Transparent-Semiconducting NiO Film Deposited on an n-type GaN Homoepitaxial Layer. *Appl. Phys. Letter, 110* (18), 181102(1–5). DOI:10.1063/1.4982653
12. Dutta, T., Gupta, P., Gupta, J., & Narayan, J. (2010). Effect of Li Doping in NiO Thin Films on its Transparent and Conducting Properties and its Application in Heteroepitaxial p-n Junctions. *J. Appl. Phys., 108* (8), 083715 (1–7). DOI:10.1063/1.3499276
13. Xia, X. H., Tu, J. P., Zhang, J., Wang, X. L., Zhang, W. K., & Huang, H. (2008). Morphology Effect on the Electrochromic and Electrochemical Performances of NiO Thin Films. *Elec. Acta, 53* (18), 5721–5724. DOI:10.1016/j.electacta.2008.03.047
14. Tomono, K., & Sugiyama, M. (2024). Investigating Electrical Properties and Crystal Growth in NiO Thin Films by Spray Pyrolysis and Electrostatic Spray Deposition. *J. J. A. Physics,* 63, 025504(1–5). DOI:10.35848/1347-4065/ad1f09
15. Cullity, B. D. (1956). *Element of X-Ray Diffraction*. Upper Saddle River: Prentice Hall.
16. Pope, C. G. (1997). X-Ray Diffraction and the Bragg Equation. *J. Chem. Educ., 74* (1), 129–131. DOI:10.1021/ed074p129
17. Pal, U., Serrano, J. G., Santiago, P., Xiong, G., Ucer, K. B., & Williams, R. T. (2006). Synthesis and Optical Properties of ZnO Nanostructures with Different Morphologies. *Optical Materials, 29* (1), 65–69. DOI:10.1016/j.optmat.2006.03.015
18. Saleem, M., Fang, L., Ruan, H. B, Wu, F., Huang, Q. L., Xu, C. L., & Kong, C. Y. (2012). Effect of Zinc Acetate Concentration on the Structural and Optical Properties of ZnO Thin Films Deposited by Sol-Gel Method. *Intl. J. Phy. Sci., 7,* (23), 2971–2979. DOI:10.5897/IJPS12.219
19. Bindu, P., & Thomas, S. (2014). Estimation of Lattice Strain in ZnO Nanoparticles: X-ray Peak Profile Analysis. *J. Theor. Appl Phys., 8*, 123–134. DOI:10.1007/s40094-014-0141-9
20. Kumar, V., Sharma, H., Singh, S. K., Kumar, S., & Vij, A. (2019). Enhanced Near-band Edge Emission in Pulsed Laser Deposited ZnO/c-sapphire Nanocrystalline Thin Films. *App. Physics A, 125*, 212 (1–7). DOI:10.1007/s00339-019-2485-0
21. Singh, S. K., & Singhal, R. (2018). Thermal-Induced SPR Tuning of Ag-ZnO Nanocomposite Thin Film for Plasmonic Applications. *Appl. Surf. Sci., 439*, 919–926. DOI:10.1016/j.apsusc.2018.01.112
22. Raoufi, D. (2013). Synthesis and Microstructural Properties of ZnO Nanoparticles Prepared by Precipitation Method. *Renewable Energy, 50*, 932–937. DOI:10.1016/j.renene.2012.08.076
23. Uno, K., Yamasaki, Y., & Tanaka, I. (2017). Growth Mechanisms of Zinc Oxide and Zinc Sulfide Films by Mist Chemical Vapor Deposition. *APEX 10*, 015502 (1–5). DOI:10.7567/APEX.10.015502

24. Dommann, A., & Neels., A. (2009). The Role of Strain in New Semiconductor Devices. *Adv. Eng. Materials, 11* (4), 275–277. DOI:10.1002/adem.200800343

25. Bardeen, J., & Shockley, W. (1950). Deformation Potentials and Mobilities in Non-Polar Crystals. *Phys. Rev., 80* (1), 72–80.

26. Dunne, F. P. E., Kiwanuka, A, R., & Wilkinson, A. J. (2012). Crystal Plasticity Analysis of Micro-deformation, Lattice Rotation and Geometrically Necessary Dislocation Density. *Proc. R. Soc. A, 468*, 2509–253. DOI:10.1098/rspa.2012.0050

sciendo

LATVIAN JOURNAL OF PHYSICS
AND TECHNICAL SCIENCES
2025, N 2

DOI: 10.2478/lpts-2025-0012

INFLUENCE OF ECO-DESIGN POLICY AND ENERGY LABELING ON THE LEVEL OF ENERGY EFFICIENCY AND FUNCTIONALITY OF LED LAMPS

S. Baghirov[1]*, V. Kharchenko[2], S. Shpak[3], O. Pitiakov[4],
S. Kyslytsia[5], T. Sakhno[6], H. Kozhushko[5]

[1]Azerbaijan Technical University,
25 H.Javid Ave., Baku, 1073, AZERBAIJAN
[2]O.M.Beketov National University of Urban Economy,
17 Chornoglazivska Str., Kharkiv, 61002, UKRAINE
[3]State Enterprise "Poltava Regional Research and Technical Center
of Standardization, Metrology and Certification",
16 Henerala Dukhova Str., Poltava, 36014, UKRAINE
[4]Poltava Polytechnic Professional College,
Separated Structural Unit of National Technical University
"Kharkiv Polytechnic Institute",
83A Pushkina Str., Poltava, 36000, UKRAINE
[5]Poltava National Technical Yuri Kondratyuk University,
24 Pershotravnevyj Ave., Poltava, 36011, UKRAINE
[6]Poltava State Agrarian University,
1/3 Skovorody Str., Poltava, 36003, UKRAINE
*e-mail: sabirbagirov4@gmail.com

Considering the light engineering and environmental advantages of light-emitting diode (LED) light sources, lighting systems using LEDs should provide a decisive impact on increasing the energy efficiency of lighting and reducing greenhouse gas emissions. One of the priority directions of the energy saving policy is eco-design, which involves measures to reduce negative impacts on the environment and increase the functionality of LED light sources. The article presents the results of the study of commercial samples of non-directional LED lamps of various brands for compliance with the Commission Regulation European Union (EU) 2019/2020 on establishing requirements for the eco-design of light sources and the Commission Delegated Regulation EU 2019/2015 on energy labelling, which came into force in 2021. It is shown that the light output of the studied batches of lamps with a power of 5–12 W is in the range of 90–120 lm/W, which corresponds to energy efficiency classes, accord-

ing to the new rating scale of the Commission Delegated Regulation EU 2019/2015, F and E. Over the past decade, the luminous efficiency of lamps supplied to Ukraine has increased by more than 30 %. Quality indicators of light are also improved: all tested lamps have a general colour rendering index of Ra>80; in five of the 8 batches of lamps, the colour unevenness does not exceed the 3-steps Mac-Adam ellipses, and only in one batch individual lamps exceed the 6-steps ellipse; all tested lamps meet the requirements for the level of flickering (<1) and the level of visibility of the stroboscopic effect (SVM<0.4). Individual inconsistencies of the lamps with the established requirements have also been noted, in particular lamps with a power of 11 and 12 W do not meet the power factor $\cos\varphi_1$, a number of manufacturers do not fully declare the characteristics of their products; most of the lamps have a low special colour rendering index R_9. Conclusions have been made about the effectiveness of the eco-design policy and energy labelling in increasing the energy efficiency, quality and safety of LED lamps.

Keywords: *Energy efficiency, energy labelling, LED lamps, regulation of the EU Commission*.

1. INTRODUCTION

Lighting consumes 15 % of global electricity consumption, which accounts for 4.6 % of total greenhouse gas emissions during its production [1]. The EU aims at building an economy with zero greenhouse gas emissions by 2050, and to achieve this aim, the task is to increase the energy efficiency of lighting equipment by at least 32.5 % by 2030 [2]. Considering the energy and environmental advantages of LED products, lighting systems using LED technology should have a decisive impact on increasing the energy efficiency of lighting and reducing greenhouse gas emissions. One of the priority areas of the energy saving policy is eco-design, which involves measures to reduce negative impacts on the environment. As a result of the implementation of the EU Commission's regulations on eco-design and energy labelling over the past decades, significant results have been obtained in terms of increasing the efficiency of light sources. The requirements for the eco-design of light sources are becoming stricter regarding the establishment of minimum values of efficiency and functionality parameters, which is confirmed by the constant adoption of new directives and regulations in the EU.

In 2019, the European Commission announced a new EU Commission Regulation 2019/2020 on establishing eco-design requirements for light sources and separate start-up control devices in accordance with Directive 2019/125/EU of the European Parliament and of the Council and on the repeal of EU Commission Regulations No. 244/2009, 245/ 2009 and 1194/2012 [3]. The peculiarity of this regulation is that, in addition to energy efficiency requirements, a number of new indicators for light quality and functionality of LED light sources have been established. In particular, the declared value of energy consumption should not exceed the maximum allowed power, which is determined as a function of the declared useful luminous flux and colour rendering index; established requirements for the quality of colour rendering and colour uniformity (changes in colour coordinates within the 6-steps or smaller Mac-Adam ellipse); new

requirements have been established for the level of flickering brightness of LED light sources, characterised by the short-term and the level of SVM, etc.

The new Commission Delegated Regulation EU 2019/2015 on the energy labelling of light sources [4] entered into force on 1 March 2021. The most important change in this Regulation of the EU Commission has been the return to the A-G rating scale, which sets the maximum and minimum energy efficiency. The scale is designed in such a way that initially only a small number of products have high energy efficiency in order to introduce more efficient products in the future. At present, more and more LED light sources in accordance with the scale established by the previous regulation of the EU Commission [5] have reached classes A, A+, A++, and it is difficult for consumers to evaluate the difference, for example, between classes A and A++. According to the new scale of the EU Regulation Commission [4], the highest indicators of light sources correspond to class D and there is a large margin for adding more efficient products to this scale in the future.

Given that the requirements for energy efficiency and functionality of LED light sources are constantly increasing, and production technologies are being improved, researching commercial samples of products according to established mandatory requirements is crucial. Additionally, informing consumers about the current technical level of products from various manufacturers is also a pressing concern.

This study involves analysing the requirements for the eco-design of LED light sources, conducting experimental studies on non-directional LED lamps entering Ukraine, complying with EU Commission Regulation 2019/2020, and determining the energy efficiency classes of these lamps in accordance with Commission Delegated Regulation EU 2019/2015.

2. ANALYSIS OF REQUIREMENTS FOR ENERGY EFFICIENCY AND FUNCTIONALITY OF LED LIGHT SOURCES

The EU Commission Regulation 2019/2020 [3] sets eco-design requirements for light sources used for general lighting with a luminous flux of 60–82.000 lm and a luminous flux from the projection area of the light-emitting surface of more than 500 lm/mm^2. The regulation applies to incandescent lamps, low-and high-pressure discharge lamps, inorganic (LED) and organic (OLED) light-emitting diode lamps and luminaires. The regulation contains requirements for energy efficiency and functionality, as well as requirements for providing information and permissible deviations of product parameters from declared values. In this study, only those issues that concern LED lamps of non-directional radiation are considered.

The Regulation of the Commission Delegated Regulation EU 2019/2015 [4] establishes requirements for the calculation of energy efficiency classes of light sources based on the overall efficiency of the network η_{TM}, as well as for the provision of additional information about light sources.

In the EU, starting from 1 September 2021, the declared energy consumption value of LED light sources P_{on} should not exceed the maximum allowed power $P_{on\ max}$ (W), which is determined as a function of the declared useful luminous flux Φ_{use} (lm) and the declared colour rendering index R_a accordingly [3]:

$$P_{on\max} = C \cdot (L + \frac{\Phi_{use}}{F \cdot \eta}) \cdot R_a \quad (1)$$

where C is the basic values of the correction factor (plus allowances to C for special characteristics of light sources). For mains powered non-directional LED light sources (NDLS), the base C value is 1.08, and for mains powered directional light sources (DLS) it is 1.23. Additions to the correction factor C for LED light sources are applied only to sources with an anti-glare screen (+0.2) and sources with the ability to change the colour of light (+0.1);

η is luminous efficiency (lm/W). For LED light sources η=120 lm/W;

L is the coefficient of final losses (W). For LED light sources L=1.5 W (Table 1);

F is the efficiency factor. For LED non-directional light sources F=1.0, and for directional sources F=0.85;

R_a is the coefficient; it is 0.65 for $R_a \leq 25$ and $(R_a + 80)/160$ for $R_a > 25$.

The requirements for the functionality of LED light sources are given in Table 1.

Table 1. Requirements for the Functionality of LED Light Sources [3]

Colour rendering index (R_a)	$R_a \geq 80$
Displacement factor (DF, cos φ_1) at power input P_{on}	No limit at $P_{on} \leq 5$ W, $\cos\varphi_1 \geq 0.5$ at 5 W < $P_{on} \leq 10$ W, $\cos\varphi_1 \geq 0.7$ at 10 W < $P_{on} \leq 25$ W, $\cos\varphi_1 \geq 0.9$ at 25 W < P_{on}
Lumen maintenance factor X_{LMF}, %	The luminous flux retention coefficient X_{LMF}% after endurance tests shall be at least X_{LMFmin}%, calculated as follows: $X_{LMFmin}\% = 100 \cdot e^{\frac{(3000 \cdot \ln(0,7))}{L_{70}}}$, where L_{70} is the declared $L_{70}B_{50}$ life time (in hours). If the calculated value for $X_{LMF,MIN}$ exceeds 96.0 %, an $X_{LMF,MIN}$ value of 96.0 % shall be used.
Survival factor (SF)	The light sources must be functional after the test.
Colour consistency for LED and OLED light sources	Variation of chromaticity coordinates within a six-step Mac-Adam ellipse or less.
Flicker for LED and OLED MLS	≤ 1.0 at full-load
SVM for LED and OLED MLS	SVM ≤ 0.4 at full-load

In this Regulation, displacement factor ($\cos\varphi_1$) means the cosine of the phase angle φ1 between the first harmonic of the network voltage and the first harmonic of the network current; lumen maintenance factor (X_{LMF}) – the ratio of the luminous flux at a given time of the life cycle of the light source to the initial value of the luminous flux; survival factor (SF) is a defined fraction of the total number of light sources that continue to function for a given time under defined conditions.

The method of testing LED light sources for determining X_{LMF} and SF involves the steps described below.

1. Initial measurement of light flux before switching cycles.
2. Switching cycles: The source must be operated for 1200 complete continuous cycles. One complete switching cycle consists of 150 minutes of turning on the light source at full power, after which the source is turned off for 30 minutes. The total operating time (i.e., 3000 hours) includes only the periods of the switching cycle when the source is on. The total test time is 3600 hours.
3. Measurement of light flux after 1200 switching cycles.

4. For each of the sample units that did not fail, you need to divide the measured final luminous flux by the initial one. Determine the average value of all tested samples that did not fail, and calculate the average value of the luminous flux retention coefficient X_{LMF}% according to the formula given in Table 1.
5. The SF after 1200 switching cycles is determined as the number of functioning light sources to the total number of tested ones.

In order to shorten the test period, accelerated methods for estimating the service life of LED light sources have been recommended for the first time in [3]. The service life for these light sources means the time (in hours) from the start of their use until 50 % of the light sources under test have gradually reduced their luminous flux conservation factor (X_{LMF}) to 70 % of the initial value. It is also called $L_{70}B_{50}$ service life. The service life is estimated based on the experimentally determined X_{LMF} retention coefficient after 1200 switches (3000 hours of lamp burning).

"Colour consistency" means the maximum deviation of the initial spatially averaged chromaticity coordinates (x, y) of a separate light source from the central chromaticity point (cx, cy) declared by the manufacturer, expressed as the size (in steps)) of the Mac-Adam ellipse formed around the central chromaticity point (cx, cy). The size of the Mac-Adam ellipse is determined by the number of standard deviation colour matching (SDCM) units between the centre of the ellipse and its border. The method of determining colour uniformity is established in [6], [7].

The indicator of flicker level used in this Regulation is the parameter "P_{st}^{LM}", where "st" stands for short-term, and "LM" stands for the flicker measurement method defined in standards establishing measurement methods and requirements for devices for accurate perception of voltage fluctuations. Flicker in the frequency range of 0.05 Hz–80 Hz is assessed by the short-term according to [8]. The interpretation of test results is as follows:

- at $P_{st}^{LM} = 1$, the investigated light source has a flickering level that the observer detects with a probability of 50 %, such as in incandescent lamps with a power of 60 W;
- at $P_{st}^{LM} < 1$, the light source has a flickering level lower than that of incandescent lamps with a power of 60 W;
- at $P_{st}^{LM} > 1$, the level of flickering is higher than that of incandescent lamps and it is easy to detect.

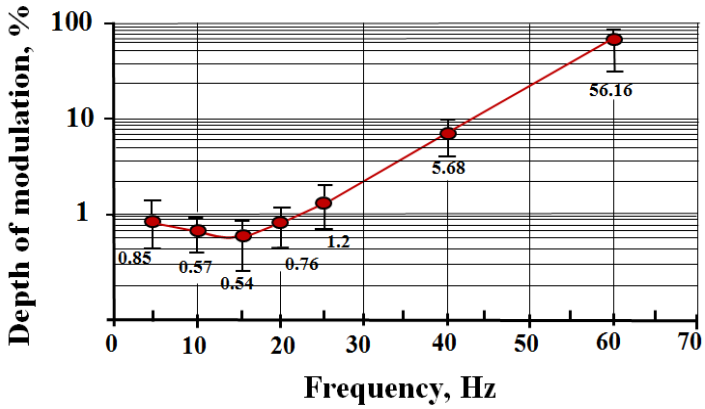

Fig. 1. Threshold values of the depth of brightness modulation at different frequencies [9].

Figure 1 shows the threshold values of the modulation depth depending on the detection frequency with a probability of 50 % [9]. As can be seen from Fig. 1, at a frequency of 15 Hz, an observer can detect a flicker with a relative modulation depth of 0.5 %, while at a frequency of 60 Hz, a modulation depth of almost 60 % is required to detect a flicker.

The resulting modulation values for each frequency are expressed in terms of detection thresholds and denoted as M_{pk}. The perceived modulation corresponding to the threshold value (detected with a probability of 50 %) is taken as one.

At values smaller than one, it is not possible to detect blinking, and at significantly higher values, it is easy to detect. If the blinking in the interval 3–60Hz has different frequencies, then the resulting perception of modulation M_p is determined as:

$$M_p = \sqrt{\sum_k (M_{pk})^2} \qquad (2)$$

where k=1, 2, 3 …

The resulting value of M_p is interpreted in the same way as M_{pk} for individual frequencies: at M_p=1, threshold values are detected with a probability of 50 %; at M_p<1, blinks are not visible; at M_p > 1, blinking is easy.

As for the estimation of the SVM, the objective method of measuring the indicator of the SVM is proposed in the standard [10]. The conditions for the appearance of the SVM considered in this document are limited to the assessment at illuminances of more than 100 lux and at moderate object velocities (< 4 m/s). SVM does not assess the health effects of flickering and is not a measure to assess unwanted SVM in industry. The method is designed to estimate light flickering at offices, residential premises etc.

Numerical values of SVM can range from 0 to 9. At SVM = 0, there is no light modulation of any kind, while at SVM ≈ 9, rectangular modulation (with infinitesimal pulse duration) is 100 %. SVM is an objective indicator obtained on the basis of laboratory studies and studies on the detection of thresholds for the perception of the SVM by people. The sensitivity to the detection of the SVM at different frequencies is shown in Fig. 2 [10].

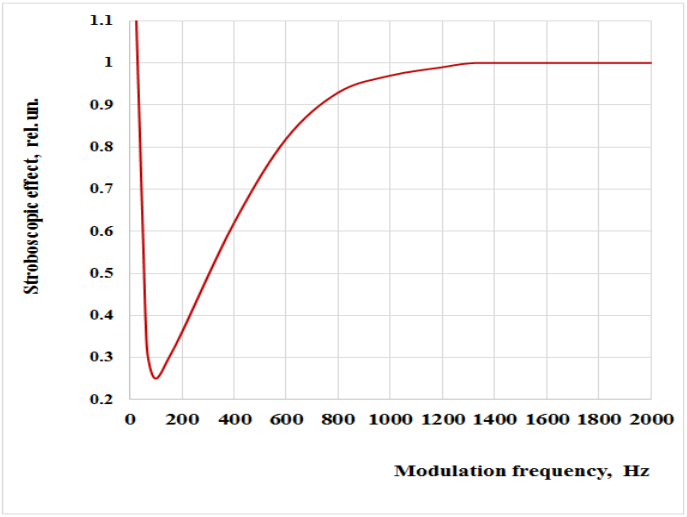

Fig. 2. Dependence of the relative sensitivity of the perception of the SVM on the light modulation frequency [10].

The SVM measurement results can be interpreted as follows:

at SVM =1, the SVM created by light modulation is on the threshold of visibility. This means that the average observer can detect the SVM with a probability of 50 %. If the value of SVM<1, then the detection probability is less than 50 %, and if SVM >1, then the match will be higher than 50 %.

The energy efficiency classes of light sources according to [4] are determined on the basis of the overall network efficiency coefficient η_{TM}, which is calculated by dividing the declared useful luminous flux Φ_{use} (expressed in lm) by the declared power in full burning mode P_{on} (expressed in W) and multiplied by the F_{TM} coefficient, which takes into account the type of directional and non-directional light sources, as well as types that work in the power network and without it, as follows:

$$\eta_{TM} = (\frac{\Phi_{use}}{P_{on}}) \cdot F_{TM} \quad (3)$$

The energy efficiency classes of light sources for different network efficiency coefficients η_{TM} are given in Table 2, and F_{TM} coefficients – in Table 3.

Table 2. Energy Efficiency Classes of Light Sources [4]

Energy efficiency class	**Total network efficiency η_{TM}, lm/W**
A	$210 \le \eta_{TM}$
B	$185 \le \eta_{TM} < 210$
C	$160 \le \eta_{TM} < 185$
D	$135 \le \eta_{TM} < 160$
E	$110 \le \eta_{TM} < 135$
F	$85 \le \eta_{TM} < 110$
G	$\eta_{TM} < 85$

Table 3. F_{TM} Coefficients for Different Types of Light Sources [4]

Light source type	F_{TM}
Non-directional (NDLS) operating on mains (MLS)	1.000
Non-directional (NDLS) not operating on mains (NMLS)	0.926
Directional (DLS) operating on mains (MLS)	1.176
Directional (DLS) not operating on mains (NMLS)	1.089

Energy labelling complements the Ecodesign Directive by providing information on the product energy efficiency. The new energy labeling labels (Fig. 3) have a QR code, by scanning which consumers can find additional information on the energy-consuming product.

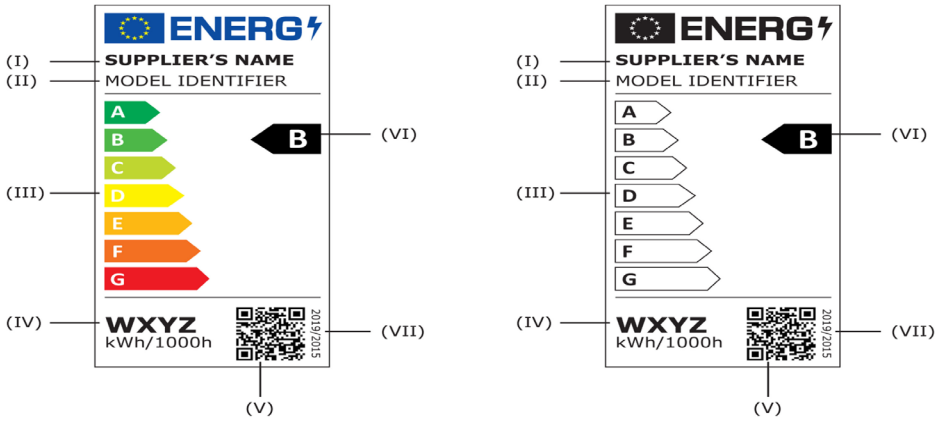

Fig. 3. The general appearance of the label: I – name or trademark of the supplier; II – provider model identifier; III – scale of energy efficiency classes from A to G; IV – energy consumption of the light source in the switched-on mode, expressed in kW of electricity consumption for 1000 hours; V – QR code; VI – energy efficiency class of the source; VII – the number of this regulation is 2019/2015.

In 2019, the European Commission launched a new publicly available database that allows consumers to compare the energy efficiency class of various household products and their other characteristics. The European Register of Energy Product Labelling (EPREL) is breaking new ground by helping EU consumers improve energy efficiency with detailed information on energy-labelled products. Now that the EPREL database is publicly available, consumers have a free online tool that can help them easily find the most energy-efficient lamp models they want to buy and get key information about them in all EU languages.

Energy efficiency and light quality of commercial LED light sources have been studied in many works [13]–[19]. To accelerate the process of saving electricity for lighting, the CALiPER [11] test programme for LED lamps was planned to provide the market with reliable information about the technical level of products. Tests within the framework of this programme showed that already at the first stages of the introduction of LED light sources, most commercial samples demonstrated high energy efficiency indicators, although a significant part of them (more than 30 %) did not fully correspond to the data declared by the manufacturer. At the end of 2013, the maximum efficiency of the best samples of non-directional LED lamps (categories up to 800 lm) included in the LED Light Facts database [12] was 90 lm/W. In 90 % of such lamps, the total colour rendering index R_a exceeded the value of 80 units, and almost 90 % of the lamps met the new requirements of the ENERGY STAR standard.

The improvement of LED lamp production technology and the introduction of international standards and regulations of the EU Commission regarding eco-design and energy-efficient labelling of light sources contributed to the further rapid increase in energy efficiency and functionality of these lamps. Today, the best commercial samples of non-directional LED lamps have already exceeded the luminous efficiency of 140 lm/W, and the general colour rendering index R_a of almost all manufacturers' lamps exceeds 80 units. The results of the study of energy efficiency and colour parameters are given in [13]–[15], and works [16]–[19] present the results of the study of brightness flickering and the SVM, the photobiological

safety of the light of LED lamps, and the assessment of the compliance of the lamp service life declared by the manufacturer with the test results.

Taking into account that the level of parameters of LED light sources is constantly increasing, the paper presents relevant studies, which relate to LED lamps of non-directional light and the assessment of their compliance with the requirements of the new EU Commission Regulation 2019/2020 on eco-design and the determination of energy efficiency classes according to the EU Commission Regulation 2019/2015.

3. RESEARCH RESULTS

Commercial samples of non-directional LED lamps that were delivered to Ukraine in the period 2021–2023 were studied. The following indicators of LED lamps, regulated by EU Commission Regulations 2019/2020 and 2019/2015, were measured: power consumption, power factor, useful luminous flux, correlated colour temperature, chromaticity coordinates and chromaticity uniformity (change in chromaticity coordinates within 6 SDCM), total color rendering index and special R_9 index, short-term flicker index and SVM index.

Based on the measurements and the data declared by the manufacturer, the maximum permissible power was calculated (which was determined as a function of the useful light flux and the declared colour rendering index), the light output and the overall efficiency of the network, the energy efficiency class according to the EU Commission Regulation 2019/2015. In order to estimate the service life for a batch of LED lamps with a power of 5 W, the luminous flux retention coefficients after testing up to 3000 hours of lamp operation (1200 switching cycles) and SF durability coefficients were determined according to [3]. Measurements of electrical, photometric and colorimetric parameters of LED light sources were carried out in accordance with recommendations [6], [7], [20].

The short-term blinking index and SVM index were determined in accordance with the standards [8], [10]. A spectroradiometer MK350S was used to measure colorimetric parameters and indicators of blinking and SVM [21]. The results of measurements and calculations are shown in Tables 4–6.

Table 4. Results of Measuring Electrical, Light Parameters and Energy Efficiency of Commercial Samples of Non-directional LED Lamps Entering the Market of Ukraine

n/p	Brand, model	Power, W		Maximum permissible power (calculated), P_{onmax}, W	$\cos\varphi_1$, rel.un.		Luminous flux, lm		Luminous efficiency, lm/W		Energy efficiency class	
		declared	measured		declared	measured	declared	measured	declared	measured	declared	measured
1	2	3	4	5	6	7	8	9	10	11	12	13
1	PHILIPS 5W 4000K 470lm 44 mA E14	5	4.74	5.85	0.5	0.56	470	567	94	119.6	F	E
2	PHILIPS 5W 4000K 470lm 44 mA E14	5	4.70	5.85	0.5	0.55	470	559	94	118.9	F	E

n/p	Brand, model	Power, W		Maximum permissible power (calculated), P_{onmax}, W	$\cos\varphi_1$, rel.un.		Luminous flux, lm		Luminous efficiency, lm/W		Energy efficiency class	
		declared	measured		declared	measured	declared	measured	declared	measured	declared	measured
3	PHILIPS 5W 4000K 470lm 44 mA E14	5	4.69	5.85	0.5	0.55	470	563	94	120.0	F	E
4	PHILIPS 5W 4000K 470lm 44 mA E14	5	4.73	5.85	0.5	0.56	470	567	94	119.9	F	E
5	PHILIPS 5W 4000K 470lm 44 mA E14	5	4.70	5.85	0.5	0.55	470	563	94	119.8	F	E
6	OPTONICA 6W 6000K 480lm E27	6	6.31	5.94	0.5	0.56	480	654	80	108.3	G	F
7	OPTONICA 6W 6000K 480lm E27	6	6.18	5.94	0.5	0.56	480	618	80	104.0	G	F
8	OPTONICA 6W 6000K 480lm E27	6	6.31	5.94	0.5	0.56	480	654	80	108.3	G	F
9	OPTONICA 6W 6000K 480lm E27	6	6.31	5.94	0.5	0.56	480	658	80	108.8	G	F
10	OPTONICA 6W 6000K 480lm E27	6	6.31	5.94	0.5	0.56	480	658	80	104.7	G	F
11	LightMaster 7W 2700K 540lm 56mA GU10	7	5.95	6.48	---	0.55	540	547	77	91.9	---	F
12	LightMaster 7W 4000K 560lm 56mA GU10	7	5.83	6.66	---	0.55	560	580	80	99.5	---	F
13	ECONOMKA 7W 4200K 580lm 52mA E27	7	6.56	6.84	---	0.58	580	718	83	109.5	---	F
14	ECONOMKA 7W 4200K 580lm 52mA E27	7	6.57	6.84	---	0.58	580	722	83	109.5	---	F
15	ECONOMKA 7W 4200K 580lm 52mA E27	7	6.63	6.84	---	0.57	580	729	83	110.0	---	F
16	NEOMAX NX8B 8W 4000K E27	8	6.13	8.10	---	0.51	720	685	90	111.7	---	E
17	NEOMAX NX8B 8W 4000K E27	8	6.36	8.10	---	0.51	720	697	90	109.6	---	F
18	NEOMAX NX8B 8W 4000K E27	8	6.17	8.10	---	0.51	720	693	90	112.3	---	E

n/p	Brand, model	Power, W		Maximum permissible power (calculated), P_{onmax}, W	$\cos\varphi_1$, rel.un.		Luminous flux, lm		Luminous efficiency, lm/W		Energy efficiency class	
		declared	measured		declared	measured	declared	measured	declared	measured	declared	measured
19	NEOMAX NX8B 8W 4000K E27	8	6.34	8.10	---	0.51	720	705	90	111.2	---	E
20	NEOMAX NX8B 8W 4000K E27	8	6.29	8.10	---	0.51	720	697	90	110.8	---	E
21	PHILIPS 9W 3000K 900lm 75 mA E27	9	8.38	9.72	0.5	0.59	900	927	100	110.6	F	F
22	PHILIPS 9W 3000K 900lm 75 mA E27	9	8.76	9.72	0.5	0.60	900	939	100	107.2	F	F
23	PHILIPS 9W 3000K 900lm 75 mA E27	9	8.42	9.72	0.5	0.59	900	892	100	105.5	F	F
24	PHILIPS 9W 3000K 900lm 75 mA E27	9	8.85	9.72	0.5	0.60	900	972	100	104.8	F	F
25	PHILIPS 9W 3000K 900lm 75 mA E27	9	9.03	9.72	0.5	0.60	900	950	100	105.2	F	F
26	MAGNUM BL60 10W 860lm 4100K	10	8.82	9.07	---	0.58	860	797	86	90.4	---	F
27	MAGNUM BL60 10W 860lm 4100K	10	8.70	9.07	---	0.57	860	773	86	88.9	---	F
28	MAGNUM BL60 10W 860lm 4100K	10	8.83	9.07	---	0.57	860	833	86	94.3	---	F
29	MAGNUM BL60 10W 860lm 4100K	10	8.71	9.07	---	0.57	860	781	86	89.7	---	F
30	MAGNUM BL60 10W 860lm 4100K	10	8.74	9.07	---	0.58	860	785	86	89.8	---	F
31	IEK LLE-A60-11-230-65-E27	11	8.98	10.53	---	0.55	990	1021	90	113.7	---	E
32	IEK LLE-A60-11-230-65-E27	11	9.22	10.53	---	0.55	990	1047	90	113.6	---	E
33	IEK LLE-A60-11-230-65-E27	11	9.23	10.53	---	0.55	990	1021	90	110.6	---	E
34	IEK LLE-A60-11-230-65-E27	11	9.22	10.53	---	0.55	990	1026	90	111.3	---	E

n/p	Brand, model	Power, W		Maximum permissible power (calculated), P_{onmax}, W	$\cos\varphi_1$, rel.un.		Luminous flux, lm		Luminous efficiency, lm/W		Energy efficiency class	
		declared	measured		declared	measured	declared	measured	declared	measured	declared	measured
35	IEK LLE-A60-11-230-65-E27	11	9.20	10.53	---	0.55	990	1009	90	109.7	---	F
36	jazzway A60 12W E27 3000K	12	7.98	11.34	---	0.57	1080	741	90	92.9	---	F
37	jazzway A60 12W E27 3000K	12	7.97	11.34	---	0.56	1080	721	90	90.5	---	F
38	jazzway A60 12W E27 3000K	12	7.98	11.34	---	0.57	1080	741	90	92.9	---	F
39	jazzway A60 12W E27 3000K	12	8.25	11.34	---	0.56	1080	757	90	91.8	---	F
40	jazzway A60 12W E27 3000K	12	8.15	11.34	---	0.56	1080	757	90	92.9	---	F

Table 5. Results of Measurement of Colorimetric Parameters and Indicators of Flickering and SVM of Commercial Samples of Non-directional LED Lamps Entering the Market of Ukraine

n/p	Brand, model	CCT, K		Colour coordinates (measured)		SDCM, rel. un.		Colour rendering index R_a, rel.un.		Special colour rendering index R_9, rel.un.	SVM, rel. un.	P_{st}^{LM}, rel. un.
		declared	measured	*x*	*y*	declared	measured	declared	measured			
1	2	3	4	5	6	7	8	9	10	11	12	13
1	PHILIPS 5W 4000K 470lm 44 mA E14	4000	4015	0.3805	0.3794	6	0.6	80	84.3	15.7	0.0136	0.1757
2	PHILIPS 5W 4000K 470lm 44 mA E14	4000	3978	0.3813	0.3771	6	2.1	80	84.8	18.3	0.0140	0.1237
3	PHILIPS 5W 4000K 470lm 44 mA E14	4000	4018	0.3799	0.3775	6	1.2	80	84.6	17.1	0.0146	0.3005
4	PHILIPS 5W 4000K 470lm 44 mA E14	4000	4026	0.3796	0.3773	6	1.2	80	84.4	16.6	0.0141	0.1961
5	PHILIPS 5W 4000K 470lm 44 mA E14	4000	3763	0.3918	0.3847	6	6.1	80	84.0	15.0	0.1380	0.1600
6	OPTONICA 6W 6000K 480lm E27	6000	5961	0.3220	0.3451	---	6.3	80	83.4	6.7	0.0060	0.0403
7	OPTONICA 6W 6000K 480lm E27	6000	6133	0.3186	0.3410	---	4.0	80	83.6	7.9	0.0060	0.0697

n/p	Brand, model	CCT, K		Colour coordinates (measured)		SDCM, rel. un.		Colour rendering index R_a, rel.un.		Special colour rendering index R_9, rel.un.	SVM, rel. un.	P_{st}^{LM}, rel. un.
		declared	measured	*x*	*y*	declared	measured	declared	measured			
8	OPTONICA 6W 6000K 480lm E27	6000	5940	0.3225	0.3450	---	6.7	80	82.7	5.6	0.0049	0.0565
9	OPTONICA 6W 6000K 480lm E27	6000	5693	0.3279	0.3512	---	11.5	80	82.6	4.5	0.0045	0.0648
10	OPTONICA 6W 6000K 480lm E27	6000	6030	0.3206	0.3430	---	5.4	80	83.1	6.8	0.0045	0.0649
11	LightMaster 7W 2700K 540lm 56mA GU10	2700	2949	0.4393	0.4028	---	0.4	80	82.8	7.5	0.0216	0.2399
12	LightMaster 7W 4000K 560lm 56mA GU10	4000	4135	0.3745	0.3726	---	2.9	80	84.0	12.4	0.0161	0.0179
13	ECONOMKA 7W 4200K 580lm 52mA E27	4200	3873	0.3889	0.3896	---	4.3	80	82.3	4.1	0.0249	0.3580
14	ECONOMKA 7W 4200K 580lm 52mA E27	4200	3787	0.3908	0.3843	---	5.6	80	83.1	10.0	0.0250	0.2433
15	ECONOMKA 7W 4200K 580lm 52mA E27	4200	3847	0.3889	0.3860	---	4.2	80	83.0	8.6	0.0256	0.1838
16	NEOMAX NX8B 8W 4000K E27	4000	4078	0.3768	0.3738	---	2.4	---	83.4	7.2	0.0087	0.1127
17	NEOMAX NX8B 8W 4000K E27	4000	4069	0.3771	0.3736	---	2.4	---	83.4	7.2	0.0012	0.0804
18	NEOMAX NX8B 8W 4000K E27	4000	4064	0.3774	0.3742	---	2.2	---	83.3	6.8	0.0062	0.1623
19	NEOMAX NX8B 8W 4000K E27	4000	4064	0.3774	0.3742	---	2.2	---	83.2	6.4	0.0013	0.1577
20	NEOMAX NX8B 8W 4000K E27	4000	4025	0.3791	0.3753	---	2.1	---	83.3	6.9	0.0070	0.0751
21	PHILIPS 9W 3000K 900lm 75 mA E27	3000	2937	0.4424	0.4076	6	2.0	80	82.1	5.8	0.0013	0.1183
22	PHILIPS 9W 3000K 900lm 75 mA E27	3000	2977	0.4378	0.4030	6	1.4	80	82.3	5.7	0.0116	0.1024
23	PHILIPS 9W 3000K 900lm 75 mA E27	3000	2895	0.4440	0.4056	6	2.0	80	81.6	2.9	0.0053	0.2003
24	PHILIPS 9W 3000K 900lm 75 mA E27	3000	2929	0.4424	0.4065	6	1.5	80	81.8	4.1	0.0130	0.1963

n/p	Brand, model	CCT, K		Colour coordinates (measured)		SDCM, rel. un.		Colour rendering index R_a, rel.un.		Special colour rendering index R_9, rel.un.	SVM, rel. un.	P_{st}^{LM}, rel. un.
		declared	measured	*x*	*y*	declared	measured	declared	measured			
25	PHILIPS 9W 3000K 900lm 75 mA E27	3000	3002	0.4363	0.4031	6	2.4	80	82.0	4.9	0.0106	0.2205
26	MAGNUM BL60 10W 860lm 4100K	4100	4102	0.3761	0.3742	---	2.3	75	82.5	6.2	0.0402	0.0318
27	MAGNUM BL60 10W 860lm 4100K	4100	4114	0.3760	0.3756	---	2.0	75	82.4	6.0	0.0038	0.0210
28	MAGNUM BL60 10W 860lm 4100K	4100	4067	0.3790	0.3807	---	0.9	75	81.6	2.9	0.0140	0.0324
29	MAGNUM BL60 10W 860lm 4100K	4100	4091	0.3764	0.3139	---	2.3	75	82.8	7.3	0.0055	0.0298
30	MAGNUM BL60 10W 860lm 4100K	4100	4100	0.3764	0.3753	---	1.9	75	82.8	7.1	0.0236	0.0236
31	IEK LLE-A60-11-230-65-E27	6500	6573	0.3102	0.3373	---	2.8	80	84.0	10.2	0.0156	0.0602
32	IEK LLE-A60-11-230-65-E27	6500	6707	0.3081	0.3343	---	3.6	80	84.6	12.5	0.0150	0.0337
33	IEK LLE-A60-11-230-65-E27	6500	6673	0.3088	0.3343	---	3.1	80	84.7	12.6	0.0121	0.0607
34	IEK LLE-A60-11-230-65-E27	6500	6926	0.3047	0.3311	---	6.0	80	84.7	13.0	0.0124	0.0623
35	IEK LLE-A60-11-230-65-E27	6500	6716	0.3081	0.3333	---	3.5	80	85.0	15.0	0.0114	0.0314
36	jazzway A60 12W E27 3000K	3000	2962	0.4399	0.4054	---	1.3	80	80.7	-1.1	0.2046	0.0840
37	jazzway A60 12W E27 3000K	3000	2986	0.4378	0.4042	---	1.8	80	80.4	-2.0	0.2836	0.0789
38	jazzway A60 12W E27 3000K	3000	2961	0.4409	0.4074	---	2.0	80	80.5	-2.1	0.2179	0.0852
39	jazzway A60 12W E27 3000K	3000	2959	0.4414	0.4081	---	2.3	80	80.2	-3.2	0.2242	0.0807
40	jazzway A60 12W E27 3000K	3000	2951	0.4405	0.4054	---	1.1	80	80.5	-1.6	0.2465	0.0835

To evaluate the service life of LED lamps, a batch of lamps with a power of 5 W was tested in accordance with the methodology provided in [3]. The average values of the results of measuring the luminous flux after zero hours and after 3000 hours of operation, the coefficient of preservation of the luminous flux are determined by measurements, and also calculated on the basis of the service life of the lamps declared by the manufacturers (see Table 6).

Table 6. Results of Measurement and Calculation (Based on the Declared Service Life) of the Coefficient of Preservation of the Luminous Flux X_{LMF} for a Batch of Lamps with a Power of 5 W.

The average value of the luminous flux, lm		The coefficient of preservation of the luminous flux X_{LMF}, rel.un.		SF, rel.un.	Service life of L_{70}, declared by the manufacturer, hours
Initial, Φ_0	After test, Φ_{3000}	Determined by measurement	Calculated on the basis of L_{70} declared by the manufacturer according to [3]		
560	530	0.946	0.931	1.0	15000

If the calculated value of the luminous flux conservation coefficient is the same as that determined experimentally or less, then there are reasons to assert that the average service life of the lamps declared by the manufacturer is real. If the calculated value exceeds the value of the coefficient of preservation of the luminous flux determined experimentally, then the declared service life of the lamps is overestimated. In our case, the stated term for lamps with a power of 5 W is real and it can be expected that it will be even higher than the declared value. The coefficient of durability at 3000 hours of lamp operation is 1.0 (there were no lamp failures).

As can be seen from the results obtained for all the investigated batches, the power of the lamps determined by measurements does not exceed the maximum allowed power $P_{on\ max}$ (for the declared luminous flux and colour rendering index). The measured luminous fluxes (for all batches except 12 W lamps) are with tolerances of ±10 %, not lower than the declared values. The luminous efficiency is in the range of approximately 90–120 lm/W, which corresponds to the energy efficiency classes according to the rating scale of the EU Commission Regulation 2019/2015 F and E. Over the past 10 years, the luminous efficiency of non-directional LED lamps has increased by more than 30 %. Quality indicators of light have also been improved, in particular the quality of colour rendering and colour uniformity. The total colour rendering index R_a in all the studied batches exceeds 80 units, the colour unevenness in only one batch (6 W) exceeds Mac-Adam's 6-steps ellipse (SDCM > 6), and in five of the eight batches it does not exceed 3-steps. All batches of lamps meet the requirements for the level of flickering (<1) and the level of visibility of the stroboscopic effect (SVM< 0.4).

Among the tested lamps, the highest indicators are those of the PHILIPS trade mark.

As for inconsistencies, 11 and 12 W lamps have an understated $\cos\varphi_1$ ($\cos\varphi_1 < 0.7$), the luminous flux of 12 W lamps is lower than the declared one, and 6 W lamps do not meet the level of colour unevenness. It is also necessary to note the rather low level of the special index R_9 (red colour) in almost the majority of the studied lamps and the lack of declared information about the lamps in a number of manufacturers of batches (energy efficiency classes declared

on the A^{+++} – G scale are not included in Table 4).

Despite the mentioned shortcomings, significant progress in improving the parameters of LED lamps over the past decade should be noted.

4. CONCLUSIONS

1. The policy of eco-design and energy-efficient labelling is an important mechanism for increasing the energy efficiency, safety and quality of LED light sources.
2. The EU Commission Regulation 2019/2020 for the first time has established requirements for the maximum power as a function of the declared useful luminous flux and colour rendering index, introduced mandatory requirements for the level of light flickering and the indicator of the SVM, colour uniformity (within 6-steps or smaller ellipses Mac-Adam), as well as estimated the service life based on the measurement and calculation of the luminous flux retention coefficient after 3000 hours of lamp operation.
3. EU Commission Regulation 2019/2015 returned the energy efficiency rating scale A–G instead of A^{+++} – G and established a new method of calculating energy efficiency classes. The European register of energy labelling of EPREL products was created.
4. Studies were conducted on LED lamps entering Ukraine for compliance with the requirements of the EU Commission Regulations 2019/2020 and 2019/2015, which entered into force in the EU in 2021. It has been established that most of the parameters of LED lamps meet the requirements of the new regulations of the EU Commission.
5. The following negative aspects were noted:
   - manufacturers of LED lamps do not fully declare the parameters of their products, as required by the regulations;
   - the colour coordinates of the lamps of individual manufacturers go beyond the 6-steps of the Mac-Adam ellipse (SDCM > 6);
   - the power factor of 11W and 12W lamps does not meet the requirements of the Ecodesign Regulation;
   - most of the tested lamps have a low special index R_9.
6. Thanks to the implementation of the requirements of the regulations on ecodesign and energy labelling, over the ast decade, a significant increase in energy efficiency and quality of LED lamps of non-directional light has been obtained.

REFERENCES

1. UNEP. (2017). *Accelerating the Global Adoption of Energy-Efficient Lighting*. Available at: https://united4efficiency.org/resources/acceleratingglobal-adoption-energy-efficient-lighting/
2. European Commission. (2020). *2030 Climate and Energy Framework Climate Action*. Available at: https://ec.europa.eu/clima/policies/strategies/2030_en
3. Regulation 2019/2020. *Commission Regulation (EU) 2019/2020 of 1 October 2019 laying down ecodesign requirements for light sources and separate control gears pursuant to Directive 2009/125/EC of the*

European Parliament and of the Council and repealing Commission Regulations (EC) No 244/2009, (EC) No 245/2009 and (EU), No. 1194/2012, 32. Available at: https://eur-lex.europa.eu/eli/reg/2019/2020/oj/eng

4. Regulation 2019/2015. *Commission Delegated Regulation EU 2019/2015 of 11 March 2019 supplementing Regulation EU 2017/1369 of the European Parliament and of the Council with regard to energy labelling of light sources and repealing Commission Delegated Regulation EU No 874/2012.(2019).34.*__ Available at: https://eur-lex.europa.eu/eli/reg_del/2019/2015/oj
5. Regulation 874/2012. *Commission Delegated Regulation (EU) No 874/2012 of 12 July 2012 supplementing Directive 2010/30/EU of the European Parliament and of the Council with regard to energy labelling of electrical lamps and luminaires. (2012).* Official Journal of the European Union, 20.https://eur-lex.europa.eu/legal-content/EN/TXT/?uri=celex%3A32012R0874
6. European Standard 13032-4. (2019). *EN 13032-4:2015+A1:2019 Light and lighting. Measurement and Presentation of Photometric Data of Lamps and Luminaires – Part 4: LED Lamps, Modules and Luminaires.* Available at: https://standards.iteh.ai/catalog/standards/cen/6344ba8a-85f9-42d3-b0a1-6f10e39beaa3/en-13032-4-2015a1-2019
7. International Commision on Illumination. (2014). CIE TN 001-2014 Chromaticity Difference Specification for Light Sources. Available at: https://files.cie.co.at/738_CIE_TN_001-2014.pdf
8. International Electrotechnical Commission. (2020). *IEC TR 61547-1:2020 Equipment for General Lighting Purposes – EMC Immunity Requirements – Part 1: Objective Light Flickermeter and Voltage Fluctuation Immunity Test Method*. Available at: https://webstore.iec.ch/publication/64795
9. ASSIST. (2015). *Recommended Metric for Assessing the Direct Perception of Light Source Flicker.* Available at: https://www.lrc.rpi.edu/programs/solidstate/assist/pdf/AR-FlickerMetric.pdf
10. International Electrotechnical Commission. (2018). *IEC TR 63158:2018 Equipment for General Lighting Purposes – Objective Test Method for Stroboscopic Effects of Lighting Equipment*. Available at: https://webstore.iec.ch/en/publication/61455
11. US Department of Energy. (n.d.). *CALiPER*. Available at: https://www.energy.gov/eere/ssl/caliper
12. Energy Star. (n.d.) *Learn about LED Lighting.* Available at: https://www.energystar.gov/products/light_bulbs/learn-about-led-lighting
13. Luis, A., Fernando, H., Omar, P., & Francisco, A. (2022). Application of the MEPS policy and European Union labeling on interior lighting products in the Colombian market. In *Book of Minutes of XVI Ibero-American Illumination Congress (Luxamerica)*, (pp. 155–161). Chile.
14. Neyezhmakov, P., Pitiakov, O., Shpak, S., Kyslytsia, S., & Kozhushko, G. (2022). The Current State of Energy Efficiency and Light Quality of LED Products. *Ukrainian Metrological Journal*, *1*, 12–19. Available at: https://doi.org/10.24027/2306-7039.1.2022.258690
15. Junior, B., Melero, E., Santos, J., & Roberto, E. (2023). Performance from SSL lamps used in the Brazilian residential sector. *In Proceedings of International Conference on Energy Efficiency in Domestic Appliances and Lighting*, (pp. 547–563). 1–3 June 2022, Toulouse, France.
16. Gil-de-Castroa, A., Rönnberg, S., & Bollen, M., (2017). Light Intensity Variation (Flicker) and Harmonic Emission Related to LED Lamps. *Electric Power Systems Research*, *146*, 107–114.
17. Baghirov, S., Pitiakov, O., Shpak, S., Kyslytsia, S., Sakhno, T., & Kozhushko, H. (2023). Research of Problems Flicker Level of LED Lamps and Luminaires for General Lighting *Przeglad Elektrotechniczny*, 119–123. DOI:10.15199/48.2023.12.22
18. Shpak, S., Kozhushko, G., Kyslytsia S., Sakhno, T., & Pitiakov, O. (2020). Research of the Photobiological Safety of LED Lamps and Luminaires for General Lighting. *Ukrainian Metrological Journal*, *4*, 29–35. Available at: https://doi.org/10.24027/2306-7039.4.2020.224278

19. Baghirov, S., Basova, Y., Guba, L., & Kozhushko, H. (2024). Prediction of the Service Life of LED Lamps Based on the Extrapolation of the Luminous Flux Conservation Factor. *Przeglad Elektrotechniczny*, 119–123. DOI:10.15199/48.2024.02.38

20. International Commision on Illumination. (1995). CIE 013.3–1995*: Method of Measuring and Specifying Colour Rendering Properties of Light Sources*. Vienna, Austria.

21. UPRtek. (n.d.). *MK350S Premium Spectrometer*. Available at: https://www.uprtek.com/en/product/spectrometers/mk350s-premium

sciendo

LATVIAN JOURNAL OF PHYSICS
AND TECHNICAL SCIENCES
2025, N 2

DOI: 10.2478/lpts-2025-0013

DEFORMATION BEHAVIOUR OF ORIENTED ELECTROSPUN PAN NANOFIBER MATS

J. V. Sanchaniya*, G. Moothedath

Riga Technical University,
Institute of Mechanical and Biomedical Engineering,
6B Kipsala Str., Riga, LV-1048, LATVIA
*e-mail: jaymin.sanchaniya@rtu.lv

The research addresses the limited understanding of the deformation behaviour in mechanically loaded orientated electrospun nanofiber mats, which are crucial for applications such as filtration, catalysis, and sensing. Focussing on polyacrylonitrile (PAN) as a reference polymer, we investigated the mechanical properties of PAN nanofiber membranes with aligned fibre orientations, specifically examining their response to mechanical stresses introduced by notches and punch holes. Mechanical testing revealed that these membranes showed a consistent deformation pattern at the macroscale until fracture. In particular, we observed significant variations in key parameters such as elastic modulus, ultimate strength, and critical stress in different membrane samples, which were also compared with an analytical model. The presence of a notch in the nanofiber mat reduced the strength by 48 %, indicating a remarkable fracture resistance, even in pre-damaged membranes. Furthermore, elongation of fibres along the loading direction was observed to cause the tip of the crack to not grow, providing local reinforcement to the membrane by undamaged nanofibers and enhancing its overall mechanical robustness.

Keywords: *Critical stress, deformation of nanofibers, hole, notch, tensile strength.*

1. INTRODUCTION

Electrospinning emerges as a cost-effective method for the production of nanofiber mats. This technique facilitates the fabrication of a relatively new class of materials characterised by a non-woven assemblage of nanofibers, typically from 100 to 500 nm [1]. The diminutive fibre diameter, coupled with the nonwoven structure of these mats, imparts them with distinct properties, such as an elevated internal surface area and significant porosity, whilst maintaining flexibility. Consequently, these materials have immense potential for application in areas demanding high performance, including

gas and water filtration [2], tissue scaffold engineering [3], [4], wound healing [5], [6], catalysis [7], composites [8], [9], antibacterial textiles [10] and food packaging [11]. However, the successful deployment of these materials often requires robust mechanical performance and durability.

Recent research has turned towards aligned nanofibers [12], [13] attributed to their improved strength and the consistency of their mechanical properties, yielding highly repeatable results. Although these are commonly classified as nanofiber mats in numerous studies, they are often evaluated against the standards of polymeric films [14]. This comparison is justified, given that the overall mechanical properties of nanofiber mats are calculated and these materials are treated as polymeric films in analytical and numerical calculations [8]. Fundamentally, a nanofiber mat usually has a large number of interconnected fibres.

In this context, the deformation behaviour of nanofiber mats is anticipated to diverge from that of conventional polymeric films. Notably, in the presence of an initial crack, the propagation within the nanofiber mat is expected to follow a different trajectory, influenced by the remaining nanofibers. Comprehending this deformation behaviour is crucial to understanding the performance of nanofiber mats in practical applications.

In the present study, the authors prepared nanofiber mats incorporating holes and notches, comparing them with their undamaged counterparts. The testing of these pre-damaged nanofiber mats aids in elucidating the deformation behaviour, particularly of orientated polyacrylonitrile (PAN) nanofiber mats, thereby contributing valuable insights into their structural integrity under various conditions.

2. MATERIALS AND METHODOLOGY

To investigate the deformation behaviour of orientated polyacrylonitrile (PAN) nanofibers, we used electrospun nanofibers employing PAN powder and N,N-Dimethylformamide (DMF). Polyacrylonitrile (average molecular weight: 150,000 (typical); CAS number: 25014-41-9) and N, N-dimethylformamide (DMF; ACS reagent grade, solvent; ≥ 99.8% purity; CAS number: 68-12-2) were procured from Sigma-Aldrich Chemicals, Merck KGaA, Darmstadt (64287), Germany.

Following the production of nanofiber mats as mentioned in [12], [13], [15], samples measuring 10 mm in width and 50 mm in length were precisely incised in the centre using a sharp blade, resulting in a cut length of 5 mm (half the total width). To create holes in the samples, a 5 mm diameter punch was used, ensuring precise puncturing in the centre of each sample. Figure 1 delineates the methodology for fabricating nanofiber mat samples with notches and holes.

Tensile properties were measured using a Mecmesin Multi-Test 2.5-i tensile testing machine equipped with a 250 N sensor (PPT Group UK Ltd., t/a Mecmesin, Newton House, Spring Copse Business Park, Slinfold, UK). The samples were conditioned at room temperature according to ISO 139:1973 “Standard Environments for Conditioning and Testing’, which stipulates a temperature of 21 ± 1 °C, a relative humidity of 60 %, and an atmospheric pressure of 760 mm Hg. The dimensions of the sample were conformed to ASTM D882-18, measuring 50 mm × 10 mm (length × width). To

determine the tensile properties, a quintet of measurements was conducted. The thickness of the nanofiber mats was determined using a digital micrometre (range: 0 to 25 mm; Digimatic micrometre, MDC-25PX, code No. 293-240-30, serial No. 71912410, Mitutoyo, Japan). For testing in the longitudinal direction, the specimens were cut parallel to the nanofiber orientation. A paper template was prepared, measuring 50 mm × 40 mm with an interior cut of 30 mm × 20 mm. Using double-sided thin Scotch tape (3M Scotch Magic Tape (Matte Finish) 3/4" × 36 yard desk dispenser refills), the specimen's ends were affixed to the paper template. Subsequent to attachment of the paper and sample to the tensile testing apparatus, the sides of the paper template were meticulously removed with scissors, according to the protocol detailed in [8], [12], [13].

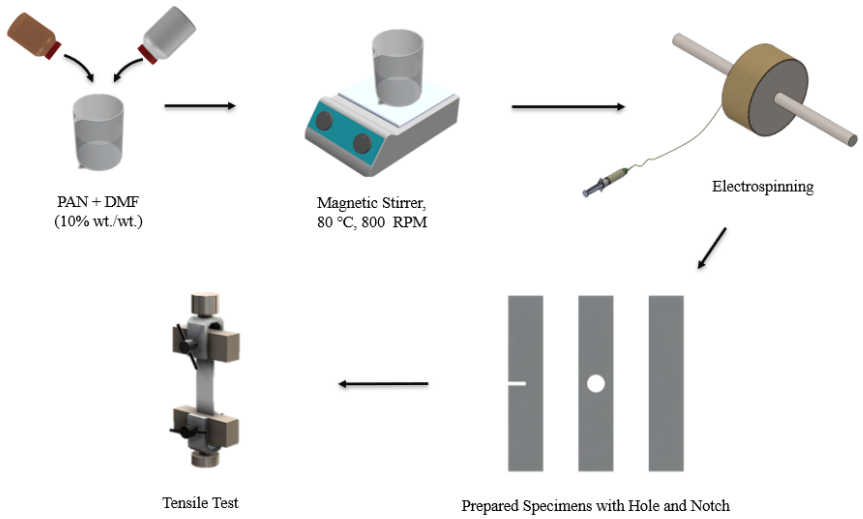

Fig. 1. Fabrication process of PAN nanofiber mats and specimens.

3. RESULTS AND DISCUSSION

Figure 2 presents representative of the stress strain curves: of the plain nanofiber mat, nanofiber mat with a hole, and nanofiber mat with a notch. The thickness found was 154±8 um of all specimens. The ultimate tensile strength on the plain nanofiber mat was 16.5±2 MPa while for the nanofiber mat with a hole was 9.1±1 and with a notch was 8.5±1. The elastic modulus of the PAN nanofiber mat was found 570±18 MPa and for the nanofiber mat with a hole it was 357±27 and for the nanofiber mat with a notch it was 368±21 MPa. The elongation at break for the entire specimen was obtained almost similarly. For the PAN nanofiber mat, the elongation at break was 15±1, for the nanofiber mat with a hole it was 13±2 and for the nanofiber mat with a notch it was 15±1. The summary of the mechanical properties of the plain nanofiber mat, the nanofiber mat with a hole, and the nanofiber mat with a notch is shown in Table 1.

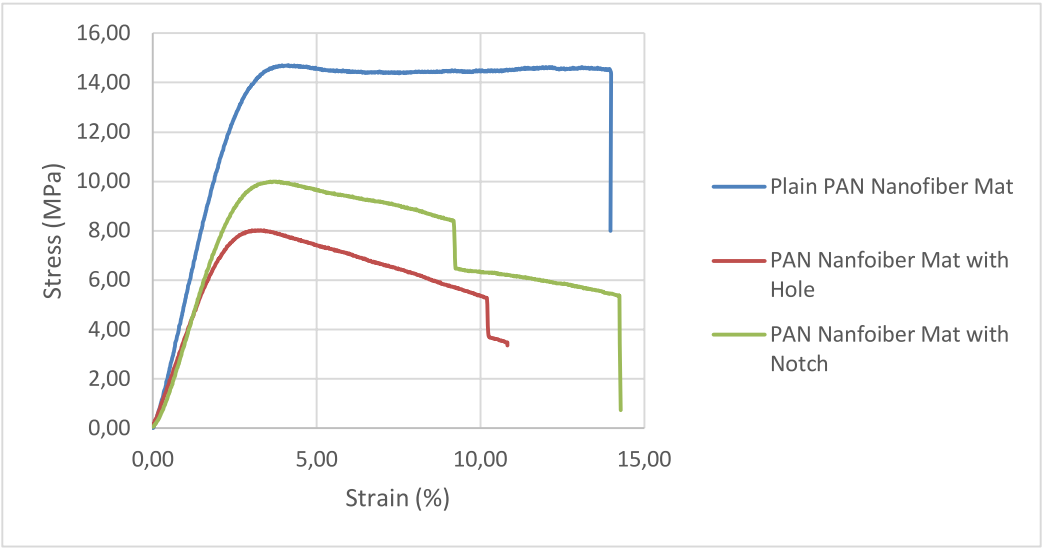

Fig. 2. Representative stress-strain curve of plain nanofiber mat, nanofiber mat with a hole, and nanofiber mat with a notch.

Table 1. Summary of the Mechanical Properties of the Plain Nanofiber Mat, the Nanofiber Mat with a Hole, and the Nanofiber Mat with a Notch.

Specimen	Thickness, t (μm)	Tensile Strength σ at Break (MPa)	Young's modulus, E (MPa)	Elongation at break, ε at Break (%)
Plain nanofiber mat	154 ± 8	16.5 ± 2	570 ± 18	15 ± 1
Nanofiber mat with hole	154 ± 8	9.1 ± 1	357 ± 27	13 ± 2
Nanofiber mat with notch	154 ± 8	8.5 ± 1	368 ± 21	15 ± 1

Figure 3 shows the deformation behaviour of the PAN nanofiber mats with a notch and a hole under loading conditions. It is evident from the figure that only the undamaged nanofibers in the mat are subjected to the load, elongating until rupture.

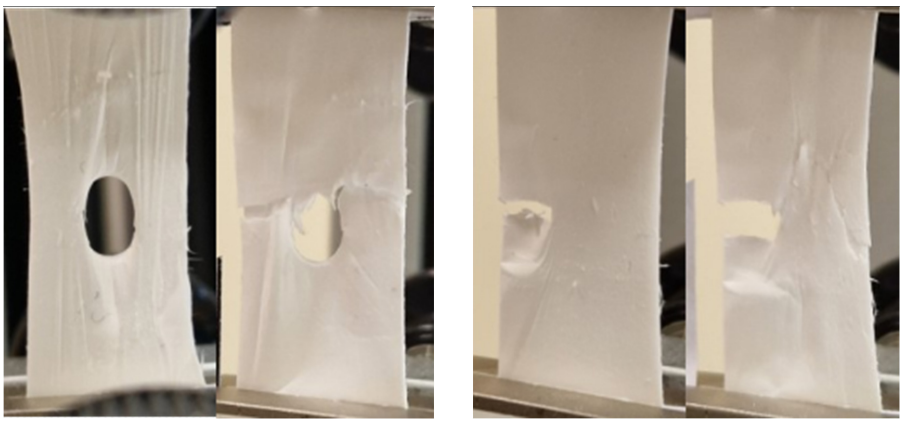

(a) (b)

Fig. 3. Deformation behaviour of nanofiber mats with a hole and a notch under load.

The experimental results indicate a significant reduction in both the elastic modulus and the ultimate tensile strength, approximately halving in value. This suggests that regardless of the presence of a notch or hole, the undamaged nanofibers within the nanofiber mat carry the load, elongating and eventually breaking, which was observed when the nanofibers were aligned in a single direction [16].

Given that all nanofibers on the mat are aligned in one loading direction, the material does not conform to traditional crack propagation theories, where a crack grows leading to failure. Instead, when the fibres are aligned in a singular direction, all undamaged nanofibers collectively sustain the load until failure. This finding also implies that, when the mechanics are at the individual nanofiber level, it cannot be equated to a thin polymeric film, where crack growth is typically expected. When considering the mechanical and numerical behaviour of nanofiber mats at the microscale, it is imperative to treat nanofibers as separate entities that do not behave analogously to a film, particularly in the context of fracture and plasticity, while considering at the macroscale when polymeric film is considered, it predicts elasticity very precisely [8], [17].

4. CONCLUSIONS

The research has comprehensively explored the deformation behaviour of orientated polyacrylonitrile (PAN) nanofiber mats, with a particular focus on understanding the impact of introduced defects such as notches and holes. The findings from this study are pivotal in elucidating the mechanical properties and response characteristics of these nanofiber mats under stress conditions.

It has been observed that the presence of holes or notches significantly influences the ultimate tensile strength and elastic modulus of the nanofiber mats. In particular, both of these mechanical parameters exhibited a marked reduction in defects in mats compared to plain mats. This reduction highlights the critical role of the structural integrity of the nanofiber network in determining the overall strength and flexibility of the material. However, the elongation at break remained relatively consistent across all samples, suggesting that the deformation capacity of the nanofiber mats is largely unaffected by the presence of small-scale damage.

Furthermore, the research findings challenge conventional notions in polymer science, particularly concerning crack propagation and failure in polymeric films. Unlike traditional polymeric films, where cracks tend to propagate, leading to failure, orientated PAN nanofiber mats demonstrated a different failure mechanism. In these mats, the undamaged nanofibers bear the load and elongate until rupture, indicating a unique interaction between the nanofibers within the mat. This behaviour underscores the need to consider each nanofiber as an individual entity in mechanical assessments, especially when considering the fracture and plasticity properties of nanofiber mats.

In conclusion, this investigation into the deformation behaviour of PAN nanofiber mats contributes valuable knowledge to the field of material science, particularly for applications where mechanical resilience and durability are paramount. The findings suggest potential for these materials in various high-demand applications, although further research is required to fully understand the long-term behaviour

and performance under diverse environmental conditions. Ultimately, this study lays the groundwork for future exploration and exploitation of the unique properties of electrospun nanofiber mats, paving the way for innovative uses in various scientific and industrial domains.

ACKNOWLEDGEMENTS

This research/publication has been supported by the Doctoral Grant Programme of Riga Technical University.

REFERENCES

1. Li, S., Guo, H., He, S., Yang, H., Liu, K., Duan, G., & Jiang, S. (2022). Advanced Electrospun Nanofibers as Bifunctional Electrocatalysts for Flexible Metal-Air (O2) Batteries: Opportunities and Challenges. *Mater. Des.*, *214*, 110406. DOI: 10.1016/j.matdes.2022.110406
2. Zhou, Y., Liu, Y., Zhang, M., Feng, Z., Yu, D. G., & Wang, K. (2022). Electrospun Nanofiber Membranes for Air Filtration: A Review. *Nanomaterials*, *12* (7). DOI: 10.3390/nano12071077
3. Arun, A., Malrautu, P., Laha, A., & Ramakrishna, S. (2021). Gelatin Nanofibers in Drug Delivery Systems and Tissue Engineering. *Eng. Sci.*, *16*, 71–81. DOI: 10.30919/es8d527
4. Hanumantharao, S. N., & Rao, S. (2019). Multi-functional Electrospun Nanofibers from Polymer Blends for Scaffold Tissue Engineering. *Fibers*, *7* (66), 1–35.
5. Ambekar, R. S., & Kandasubramanian, B. (2019). Advancements in Nanofibers for Wound Dressing: A Review. *Eur. Polym. J.*, *117*, 304–336. DOI: 10.1016/j.eurpolymj.2019.05.020
6. Kulkarni, D., Musale, S., Panzade, P., Paiva-Santos, A. C., Sonwane, P., Madibone, M., … & Cavalu, S. (2022). Surface Functionalization of Nanofibers: The Multifaceted Approach for Advanced Biomedical Applications. *Nanomaterials*, *12* (21), 3899. DOI: 10.3390/nano12213899
7. Guerrero-Pérez, M. O. (2022). Research Progress on the Applications of Electrospun Nanofibers in Catalysis. *Catalysts*, *12* (1). DOI: 10.3390/catal12010009
8. Lasenko, I., Sanchaniya, J. V., Kanukuntla, S. P., Ladani, Y., Viluma-Gudmona, A., Kononova, O., … & Selga, T. (2023). The Mechanical Properties of Nanocomposites Reinforced with PA6 Electrospun Nanofibers. *Polymers*, *15* (3), 673. DOI: 10.3390/polym15030673
9. Sanchaniya, J. V., Lasenko, I., Vijayan, V., Smogor, H., Gobins, V., Kobeissi, A., & Goljandin, D. (2024). A Novel Method to Enhance the Mechanical Properties of Polyacrylonitrile Nanofiber Mats: An Experimental and Numerical Investigation. *Polymers*, *16* (7), 992. DOI: 10.3390/polym16070992
10. Grauda, D., Butkauskas, D., Vyšniauskienė, R., Ranèelienė, V., Krasņevska, N., Miķelsone, A., … & Ļašenko, I. (2023). Establishment of Biotesting System to Study Features of Innovative Multifunctional Biotextile. *Proc. Latv. Acad. Sci. Sect. B Nat. Exact, Appl. Sci.*, *77* (3–4), 186–192. DOI: 10.2478/prolas-2023-0026
11. Zhu, W., Zhang, D., Liu, X., Ma, T., He, J., Dong, Q., … & Cai, J. (2022). Improving the Hydrophobicity and Mechanical Properties of Starch Nanofibrous Films by Electrospinning and Cross-linking for Food Packaging Applications. *LWT*, *169*, 114005. DOI: 10.1016/j.lwt.2022.114005

12. Sanchaniya, J. V., Lasenko, I., Kanukuntla, S. P., Mannodi, A., Viluma-Gudmona, A., & Gobins, V. (2023). Preparation and Characterization of Non-Crimping Laminated Textile Composites Reinforced with Electrospun Nanofibers. *Nanomaterials*, *13* (13), 1949. DOI: 10.3390/nano13131949
13. Sanchaniya, J. V., Lasenko, I., Kanukuntala, S. P., Smogor, H., Viluma-Gudmona, A., Krasnikovs, A., … & Gobins, V. (2023). Mechanical and Thermal Characterization of Annealed Oriented PAN Nanofibers. *Polymers*, *15* (15), 3287. DOI: 10.3390/polym15153287
14. Sanchaniya, J. V., Kanukuntla, S. P., & Senyurt, K. B. (2023). Fabrication and Mechanical Properties of Polymer Composite Nanofiber Mats. *Eng. Rural Dev.*, 85–90. DOI: 10.22616/ERDev.2023.22.TF014
15. Sanchaniya, J. V., Lasenko, I., Gobins, V., & Kobeissi, A. (2024). A Finite Element Method for Determining the Mechanical Properties of Electrospun Nanofibrous Mats. *Polym.*, *16* (6), 852. DOI: 10.3390/polym16060852
16. Verschatse, O., Loccufier, E., Swanckaert, B., De Clerck, K., & Daelemans, L. (2023). Microscale and Macroscale Deformation Behavior of Electrospun Polymeric Nanofiber Membranes Using In Situ SEM during Mechanical Testing. *Polymers (Basel).*, *15* (7). DOI: 10.3390/polym15071630
17. Sanchaniya, J. V., Kanukuntla, S.-P., Modappathi, P., & Macanovskis, A. (2022). Mechanical Behaviour Numerical Investigation of Composite Structure, Consisting of Polymeric Nanocomposite Mat and Textile. *21st Int. Sci. Conf. Eng. Rural Dev. Proc.*, *21*, 720–726. DOI: 10.22616/erdev.2022.21.tf225

sciendo

LATVIAN JOURNAL OF PHYSICS
AND TECHNICAL SCIENCES
2025, N 2

DOI: 10.2478/lpts-2025-0014

AN EFFICIENCY STUDY OF FOAMED POLYISOCYANURATE (PIR) MATERIALS AS BUILDING INSULATORS

D. Adilova[1], A. Tukhtamisheva[1], R. Bliudzius[2],
I. Geipele[3*], L. Jansons[3], S. Lapuke[3]

[1]International Educational Corporation,
28 Ryskulbekova Str., Almaty, 050043, KAZAKHSTAN
[2]Kaunas University of Technology,
73 K. Donelaičio St., Kaunas, 44249, LITHUANIA
[3]Riga Technical University,
Faculty of Engineering Economics and Management,
6 Kalnciema Str., Riga, LV-1048, LATVIA
*e-mail: ineta.geipele@rtu.lv

Polymeric foams are one of the most efficient thermal insulation materials because of the extra low thermal conductivity blowing agent gases trapped inside of the closed porous structures. Thermal conductivity is one of the most exclusive properties of foamed polyisocyanurate (PIR) materials. The blowing agent gases are selected based upon their characteristics of low thermal conductivity and slow diffusion rates through the foam polymers. The atmospheric gases have a greater thermal conductivity and are typically much smaller molecules with much faster diffusion rates through the foam. PIR gains much of its thermal resistance value from the blowing agents, often a pentane gas mixture, which is trapped in the foam cells. Pentane isomers are commonly used in Europe in manufacturing rigid insulating polyurethane foams. Since the thermal conductivities of the pentanes (between 0.010 and 0.014 W/(m·K)) fall significantly below that of air, polyurethane insulation panels may achieve thermal conductivity as low as 0.024 W/(m·K). This paper analyses results of the thermal conductivity study and measurements according to two different parameters: the initial value of thermal conductivity and the rate of aging, i.e., the rate of increase in thermal conductivity over time. The initial thermal conductivity value is influenced by the thermal conductivity of the gas inside the cell and the average diameter of the cell.

Keywords*: Blowing agents, insulation materials, polyisocyanurate (PIR) materials, PIR aging, thermal conductivity.*

1. INTRODUCTION

Energy efficient renovation of public and private buildings is an important part of the European Green Deal, and its key initiative is to significantly increase energy efficiency in real estate sector throughout the European Union (EU). As an element of the European Green Deal, the building renovation initiative aims at increasing energy performance and efficiency in up to 35 million buildings by 2030, at least doubling the annual rate of energy renovations in the EU [1].

Polyurethanes (PU), a diverse group of polymers with a wide range of applications as adhesives, coatings, elastomers, and foams [2], were invented in 1937 by the German scientists, who recognised that the polyaddition of liquid polyester or polyether diols with liquid diisocyanates yielded products that were superior to existing polyolefin plastics [3]. In 1954, the accidental introduction of water to the reaction mixture was shown to produce flexible foams. Later, this chemistry was modified to produce rigid foams and elastomers. Today, several types of "polyols" and "polyisocyanates" are used to produce polyurethane materials that yield varying properties.

In 1967, the class of materials known as urethane modified polyisocyanurate (PIR) foams was introduced. These compounds are essentially an improvement on PU insulations, offering improved thermal stability, flame resistance, chemical resistance, and dimensional stability [4]. During PIR production, the polyol and polyisocyanate reaction takes place at higher temperatures when compared to PU production. This allows for excess isocyanate to react with itself in what is called trimerization, producing strong chains of isocyanurate crosslinks. These crosslinks are stronger than normal PU bonds. Therefore, they are more difficult to break, resulting in improved properties.

During the manufacture of PIR insulation, the ratio of polyisocyanate to polyol (index) helps determine the final properties of the foam, and, therefore, plays a key role in determining the foam application. The low-index foam insulations exhibit behaviour closely resembling urethanes, since urethanes are produced at close to a 1/1 polyisocyanate/polyol ratio. As this ratio is increased, the trimerization reaction occurs, and the improved properties associated with PIR insulations become evident [5]. Although all these properties are important for certain applications, the improvements in dimensional stability, flame resistance, and thermal stability provide the biggest fundamental differences between PU and PIR foams [6], [7].

Polyisocyanurate insulations are produced in bunstock form, either continuously or individually box poured. Because of better consistency, performance, and quality, PIR insulation produced via the continuous process is usually preferred. These large, rectangular buns are then fabricated into various shapes, including flat boards and pipe shells, which are typically 3 to 4 feet in length. These pipe shells are designed to fit directly over nominal pipe size (NPS) pipe and tubing. Complex shapes can be fabricated to fit tightly around valves, fittings, and other equipment.

2. MATERIALS AND METHODS

The understanding of the cellular microstructure of foams is important for their thermal and mechanical performance. In fact, the cell geometry and cell parameters can be used to study heat transfer and gas permeability through analytical models. The earliest analysis of foam cellular microstructure using microscopic techniques was performed in the 1980s to observe the cellular structure of polyurethanes. The purpose of the imaging was to develop an analytical model to predict the diffusion coefficients of polyurethane gasses during the foam aging [8].

The imaging of foams was also done to compare alternative blowing agents when CFCs were being phased out. Spray and laminated polyurethane foams prepared with various blowing agents were imaged using optical microscopy to perform their cellular characterisation. Samples were analysed to determine the distribution of cell areas, aspect ratio, cell wall thickness, and cell strut thickness.

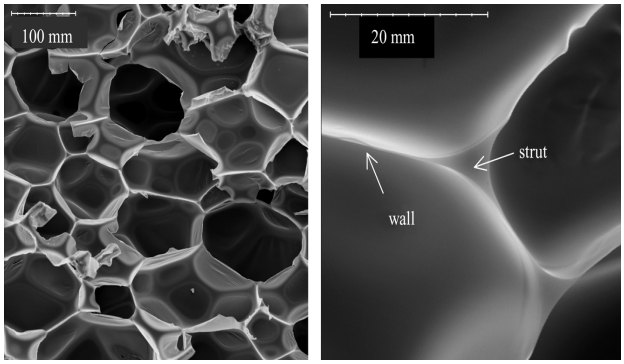

Fig. 1. Scanning electron microscope imaging of PIR foam cells [9].

PIR is a thermoset polymeric material that combines isocyanates and polyols. The manufacturing process creates a cross-linking chemical reaction that results in a robust, rigid material that does not melt when heated. By comparison, a thermoplastic material, such as polystyrene or polyethylene, will soften and become liquid on heating.

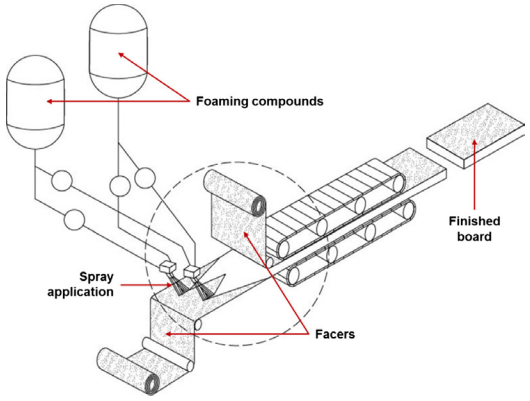

Fig. 3. PIR board production process [10].

PIR is mainly produced in the form of panels – coated panels are used in construction as thermal insulation of partitions; they can be used in refrigerators, fuel pipelines and elsewhere. PIR coatings are used to stabilise the thermal resistance of a product and to slow down the drift of thermal conductivity. In the corners of the building where these products need to join, the coatings can be arranged in the direction of heat flow, and heat transfer can be increased by thermal bridges formed in the corner of the building wall, which should be discussed further.

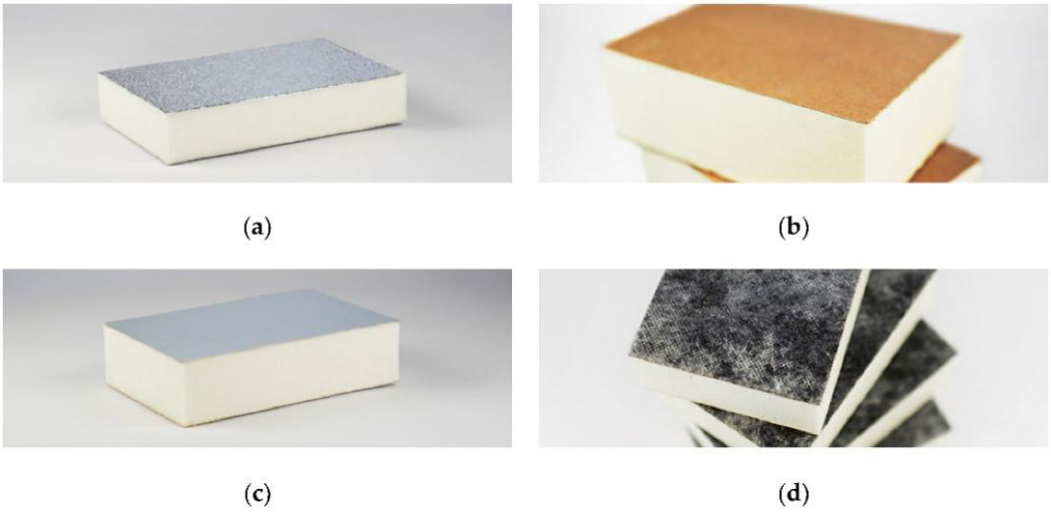

Fig. 4. PIR facing types: (a) aluminium foil; (b) composite paper foil; (c) multilayer aluminized facing; (d) bitumen facing.

2.1. Analysis of Heat Transfer through Materials

In porous foams, such as PIR, heat is transferred through a solid material by conductivity, through cells by radiation, conductivity and convection, which can be described by the following formula:

$$\lambda = \lambda_p + \lambda_g + \lambda_c + \lambda_r, \quad (1)$$

where λ_p – thermal conductivity through solid;
λ_g – thermal conductivity in gas;
λ_c – convection in cells;
λ_r – radiation through cell walls and cell itself.

When the cell size is small, heat transfer by convection through the cells is negligible, i.e., $\lambda_c = 0$.

In the production of PIR, many small, closed cells are formed, which means that the foaming agent evaporated during the foaming reaction fills these small cells as a gas. It is proposed that the total effective thermal conductivity of porous foam should have the following four inputs: thermal conductivity through solids, thermal conductivity through gas, thermal convection in cells, and thermal radiation through the cell walls and through the cells themselves. Thermal conductivity of PUR foam is tended to increase during the first 15 years after production, which is shown in Fig. 5.

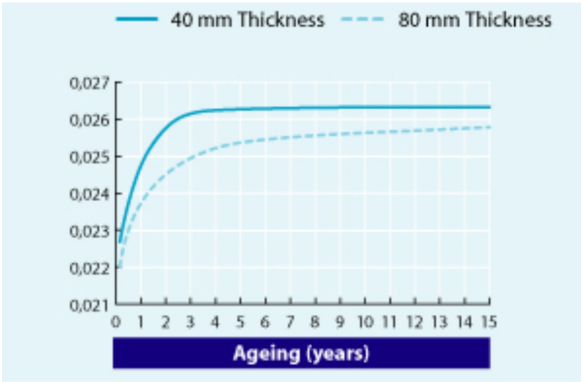

Fig. 5. Increase in thermal conductivity (W/m.K) of PUR foam during the first 15 years after production [11].

In addition to the diffusion, the blowing agent and the infusion of air, condensation affects the thermal conductivity of foams, as it creates the presence of a liquid phase and a reduction in the lowing pressure. Spray foams are prepared under high heat and high-pressure conditions.

The high vapour pressure of the blowing agent increases the total pressure inside the cell leading to expansion and initially prevents condensation risks. However, for closed cell foams, the following risks of condensation of the blowing agent result in an increase in the thermal conductivity. The impact of the condensation process on the thermal conductivity was described as a process that occurs in three regions: the first region is where the thermal conductivity decreases with the temperature up to the boiling point of the cell gas mixture; the second region is where the thermal conductivity increases as temperature decreases because the gaseous blowing agent condenses into its liquid phase; and the third region shows again a reducing thermal conductivity with the decrease of temperature, coherently with the kinetic gas theory.

Over time, when the blowing agents are absorbed into the solid polymer or escape from the material, the thermal conductivity of foams increases. The absorption of the blowing agents into the polymer cell wall is dictated by the Fick's law, and depends on the effective diffusion constant, gas concentration and time. In particular, the diffusion constant is dictated by the ratio of the gas permeation rate and solubility of the gas on the polymer surface.

When placed in the building envelope of each specific building, thermal insulating materials are exposed to temperature and humidity levels, and their actual thermal performance differs from that predicted under standard laboratory conditions. Thermal conductivity is often reported to decrease at low temperatures, although this aspect is rarely considered. However, this is usually beneficial, as it increases heat savings. Although studies show that most fibrous insulation materials have a linear relationship between their thermal conductivity and operating temperature, for some foam materials this relationship is nonlinear and difficult to predict because they have shown increased thermal conductivity at low temperatures [12].

Over time, the thermal properties of polymeric materials deteriorate as atmospheric gases rapidly penetrate the cells and expel foaming gases from them, causing the so-called aging. Finally, the foaming gas is replaced by air and the thermal efficiency

of the foam reaches a steady state, so only aged thermal conductivity values should be used [13].

The aging process takes place in two stages. During the first stage, the gas composition in the pores changes very rapidly due to diffusion. This stage of aging is called primary, and when atmospheric gas diffusion stops, the thermal conductivity changes more slowly and this stage is called secondary.

The thermal conductivity dependence on temperature is close to linear for most of insulation materials: it increases with increasing material temperature; however, the thermal conductivity of polyisocyanurate (PIR) thermal insulation material increases in the lower temperature range. The thermal conductivity of PIR also increases over the aging process, especially during the later service life, which is not covered by the standard aging procedures used to determine the declared thermal conductivity coefficient values for this material [14].

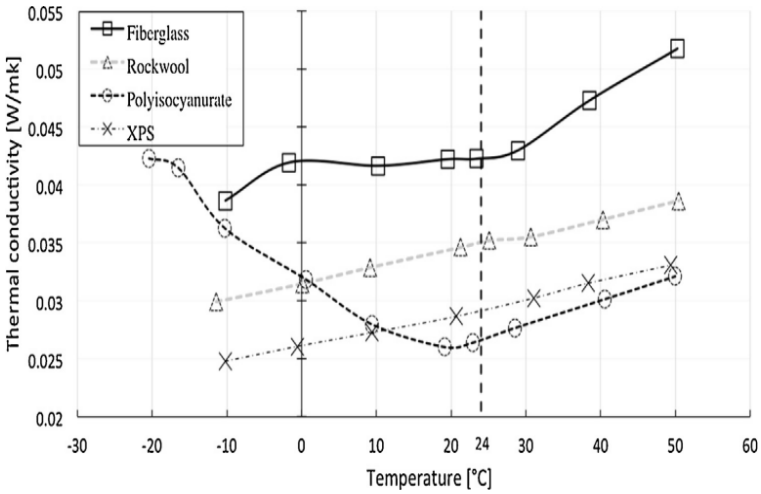

Fig. 6. Thermal conductivity dependence on temperature of thermal insulation materials [15].

2.2. Analysis of Standards for Determining Thermal Properties of Materials and Practical Measurements in the Laboratory

The main standard for rigid polyurethane foam (PUR/PIR) products is EN 13165:2012+A2:2016 [16], and the aged value can be determined in one of two ways according to this standard:

- the first is the thermal conductivity measured after 175 days of aging at 70 °C, with the addition of safety factor, which depends on the type of coating, the blowing agent of 1the foam and the thickness of the product. The safety factor may be adjusted based on a comparison between the aged values at 23 °C and 70 °C;
- the second is the thermal conductivity measured after 21 days of exposure at 70 °C with addition of a fixed increment. Fixed increment depends mainly on the type of coating and is different for different blowing agents.

The results of thermal conductivity measurements are analysed according to two different parameters: the initial value of

thermal conductivity and the rate of aging, i.e., the rate of increase of thermal conductivity over time. The initial thermal conductivity value is influenced by the thermal conductivity of the gas inside the cell and the average diameter of the cell.

Aging procedures are performed differently depending on the standard used. According to the North American standard, accelerated aging is performed by cutting the product into thin slices, and according to the standard used in Europe, aging is performed by cutting a thin sample from the core of the product. There are some limitations in both standards: with increasing temperature, the diffusion coefficients of all the different gases involved in the aging process do not change at the same rate and slicing does not consider the density of the PIR board, and the initial thermal conductivity is greatly influenced by cell filling gas composition and cell diameter.

When the temperature drops below the condensation point of the foaming gas, condensate forms in the cells and the value of the thermal conductivity coefficient increase due to the higher conductivity of the liquid phase compared to the gas phase of the foaming gas.

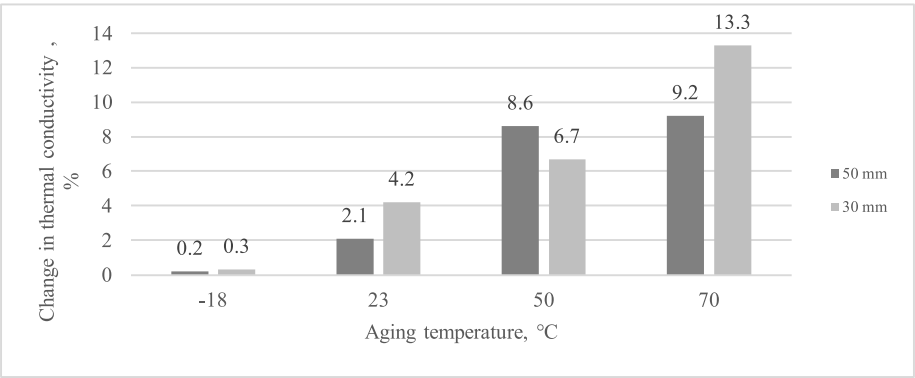

Fig. 7. Changes in thermal conductivity dependence on thickness and aging temperature.

The increase in thermal conductivity is mainly influenced by the samples stored at +70 °C. For 30 mm thick samples this change was on average 13 %, for 50 mm – about 9 %. Changes in thermal conductivity of samples stored at negative temperature were insignificant. This shows that at negative temperatures, the diffusion of the foaming gas takes place very slowly and does not change the composition of the gas to such an extent as to affect the changes in the value of thermal conductivity. For both thicknesses studied, an increase in the thermal conductivity of all types of specimens was recorded, especially in thinner specimens with removed facings. The thermal conductivity of the thicker, covered from all sides specimens increased slightly compared to the specimens with the factory-made facing, and was lower than that of the specimens with the facings removed. This confirms the influence of the compacted surface layers on the reduced gas diffusion intensity. The differences in thermal conductivity obtained are likely to be more related to the structure of the samples or their facings than to the effects of diffusion of the foaming gas. In the case of negative temperatures, neither the facing nor the negative temperature has virtually any effect on the changes in thermal conductivity.

3. RESULTS

3.1. Analysis of the Use of Materials in Building Projects

A study was conducted to evaluate the extent to which facings can affect heat transfer through partitions, especially when the facing is made of aluminium foil. The construction of a ventilated wall used for numerical modelling is shown in Fig. 7. The thicknesses and thermal properties of the components making up the structure are given in Table 1. The heat transfer coefficient of the linear thermal bridge of the modelled wall of the building was compared with the joint of the same wall corner insulated with PIR without facings and adhesive between two boards in the corner joint. The increase in heat flow through a wall corner of 1 metre due to the influence of the facings was calculated using the given equation presented in the standard EN ISO 10211:2017 [17]:

$$\Psi = L_{2D} - \sum_{j=1}^{N_j} U_j \cdot l_j, \text{ W/(m·K)}, \qquad (2)$$

where

L_{2D} – specific heat losses of the longitudinal thermal bridge, determined by calculating the two-dimensional temperature field for the component that separates two environments (inside and outside), W/(m·K);

U_j – the heat transfer coefficient calculated in the one-dimensional temperature field for component i, which separates the two environments, W/(m²·K);

l_j – the length of the two-dimensional geometric module for which the value of the heat transfer coefficient Uj is calculated, m;

N_j – 1D number of components.

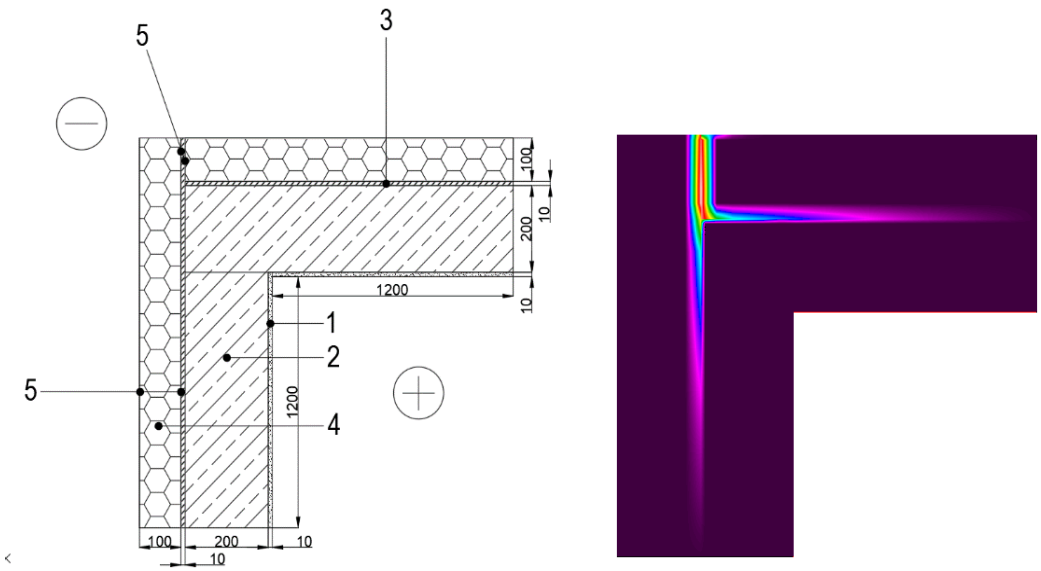

Fig. 8. Wall corner fragment (drawing and thermal imaging):
1 – plaster, 2 – aerated concrete block masonry, 3 – PU adhesive, 4 – PIR thermal insulation, 5 – PIR facing (see Table 1) (all dimensions are in millimetres).

Table 1. Materials of Wall Construction

No.	Material	Thickness, mm	Declared thermal conductivity λ, W/(m·K)
1	Plaster	10	0,9
2	Aerated concrete block masonry	200	0.13
3	PU adhesive	≤10	0.04
4	PIR board with facing:	100	0.022
	a) Aluminium foil	100 μm	211
	b) Aluminised multilayer facing	155 μm	0.125
	c) Composite paper facing	132 μm	0.066
	d) Plastic facing	103 μm	0.125

The value of the thermal bridge when using PIR with an aluminised multilayer, composite paper or plastic facing was the same. It was observed that wall corners with PIR without facings and with facings other than aluminium foil had the same values for thermal bridges, so it was not necessary to evaluate PIR facings if it was not aluminium foil. Another modelled wall corner structure was insulated with PIR with a removed aluminium foil facing in the joint between the boards and using a polyurethane adhesive in the joint. The difference in heat flow between these two structures can be of little significance. For comparison, another simulation was performed when the PIR is unfaced and without adhesive in the joint. The difference in heat flow between the two options means that without the use of glue in the joint, the heat flow through the corner of the wall is increased. To reduce the heat flux to the outside that increases through the aluminium foil facing at the PIR connection, the facings on this connection must be removed. In this case, the difference in heat flow between the PIR with the aluminium foil facing removed in the joint and the adhesive in the joint, and PIR without the facing and without the adhesive in the joint is nine times smaller than the structures shown in Fig. 8.

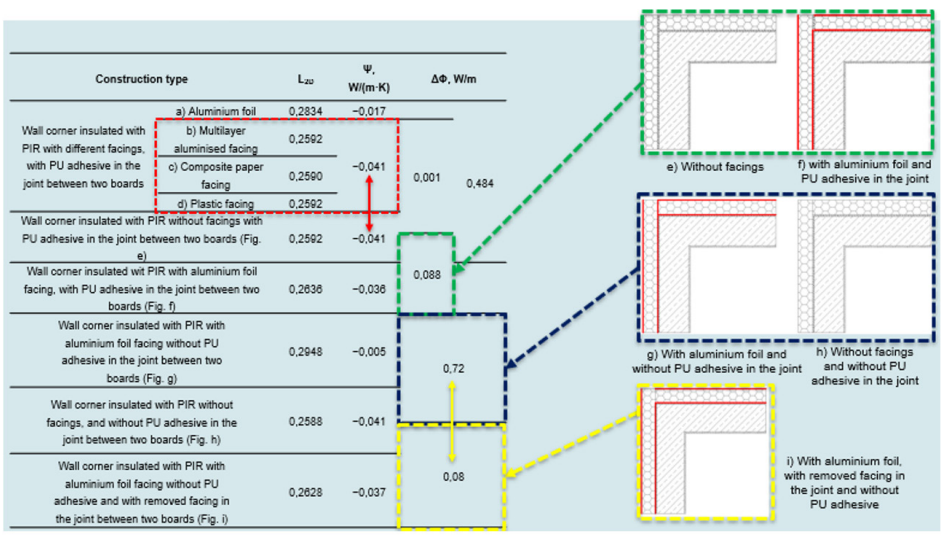

Fig. 9. Heat flux in wall corners with different facings of PIR.

After determining the possible changes in the thermal conductivity of PIR in comparison with the standard value of thermal conductivity, the effect of these differences on the heat transfer of the selected wall was analysed. The selected conditions and the calculation results showed that the thermal conductivity of the PIR determined using the standard procedure met the conditions for the calculation of the seasonal heat loss and cooling energy loss of the building. When calculating the heat loss of a building in the coldest months of the year, a lower thermal conductivity of 0.002 can be used, which would give about 8 % less heat loss through the specified enclosure. A higher value of 0.002 should be used to calculate energy losses in refrigerator buildings, which would reduce the estimated annual energy consumption for refrigeration but would not have a significant impact on actual energy consumption.

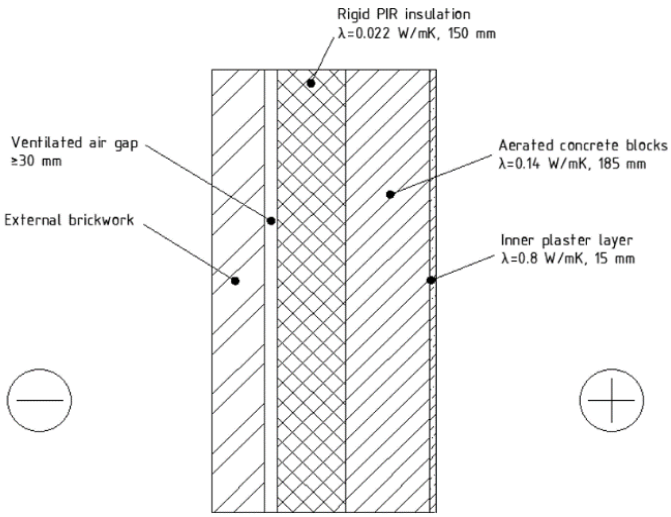

Fig. 10. A fragment of the wall of a nearly-zero energy building.

Table 2. Dependence of Wall Heat Transfer Changes on PIR Thermal Conductivity Changes

Exterior temp., °C	Interior temp., °C	Mean temp of PIR., °C	Purpose of calculation	Thermal conductivity		Heat transfer. U, W/(m^2·**K)**
				Method of determination	λ, W/(m·K)	
0	+20	+10	Heating	Declared	0.022	0.120
0	+20	+10	Heating	Heat flow meter, + 10 °C	0.021	0.116
+30	+20	+25	Cooling	Heat flow meter, extrapolated	0.022	0.120
-10	+20	+5	Heating, the coldest month	"Hot box"	0.020	0.111
-5	-15	-10	Freezing	"Hot box", extrapolated	0.024	0.129

3.2. The Use of PIR Panels to Increase the Tightness of the Building

When installing a pitched roof or a frame wall, mineral wool is often used, which is sandwiched between the rafters. In such a structure, it is necessary to install a vapour insulating layer from the inside. By using a single layer of FF-PIR insulation from the inside, it is possible not only to form a tight and reliable vapour barrier, but also to additionally insulate the structure.

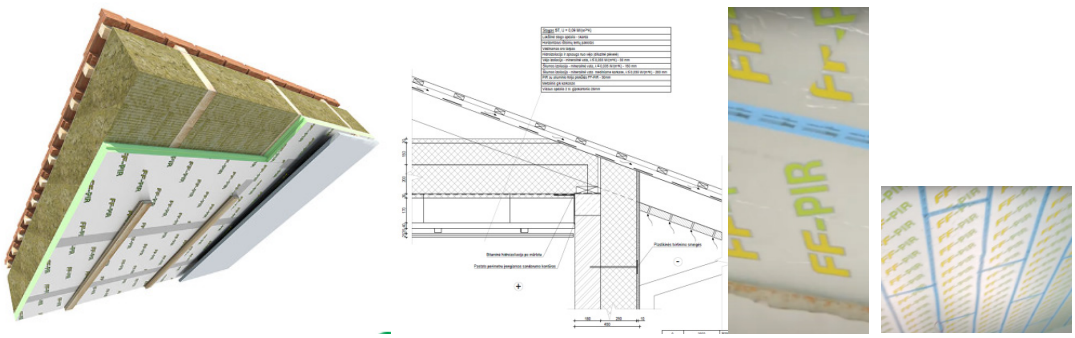

Fig. 11. Thermal insulation of ceiling and roof for improved air tightness [18].

Sandwich panels are manufactured in a wide range of thickness, with different thermal insulation cores, panel joints and profiling of the steel facings, all of which have a significant influence on the performance characteristics and the appearance of the structure.

Sandwich panels with polyisocyanurate foam (PIR) core are particularly suitable for the structures with very high thermal performance and fire safety requirements, as well as for the structures with the risk of water condensation in the thermal insulation [19].

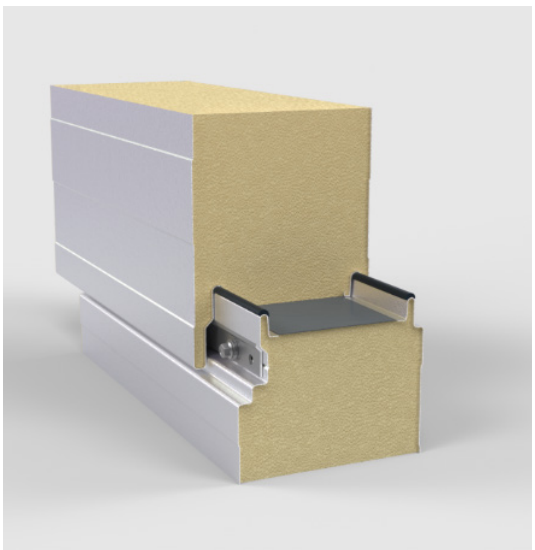

Fig. 12. Sandwich panels with polyisocyanurate foam (PIR) core [20].

4. CONCLUSIONS

1. The use of PIR products in negative temperature environments does not change their thermal conductivity measured under standard conditions, but specimens measured at low medium temperatures may increase the thermal conductivity by up to 20 % due to changes in blowing gas state: gas condenses, the distance between the molecules decreases; they form compounds which increase heat transfer between the surfaces of the material cells.
2. The largest increase in thermal conductivity of PIR products (~15 %) was found after their conditioning at +70 °C, when conditions are created for intensive diffusion of blowing gases. The thermal conductivity of the specimens with factory-made facings changed the least, and that of the thin specimens the most.
3. The standard procedure for determining the declared thermal conductivity of PIR when a specimen is cut from the core of a product does not meet the conditions for use of products with diffusion-proof facings and needs to be adjusted. The thermal conductivity of specimens aged in a high temperature environment after removal of their facings changes by more than 8 % compared to samples faced with factory-made facings. Subsequently, diffusion-proof films applied to the open sides of the specimen do not reduce the changes in thermal conductivity after aging, as they do not form such a barrier to the diffusion of blowing gases as the factory-made facings.
4. Numerical modelling and experimental measurements of wall corner joints insulated with PIR thermal insulation with contacting aluminium facing show that the increase of heat flow through the joint of walls with U value of 0.15 W/(m^2·K) compared to continuous PIR insulation is 0.72 W/m wall height, which increases the heat loss of a medium-sized (up to 150 m²) single-family home by 30–40 kWh per year.
5. The accuracy of the measurement of the thermal conductivity of PIR products by the heat flow meter method depends on the difference between the average ambient temperatures of the specimen and the measuring device. With a very low thermal conductivity of the material, a small heat flux is generated during the measurement, which can be distorted due to the lateral heat exchange between the environment, the specimen, and the measurement plates. When measuring the thermal conductivity of the specimens in a “hot box” with additional one or two heat flow sensors, the measurement accuracy can be increased by up to 5 % compared to the heat flow meter method.
6. The results of this research show that the changes in PIR are significantly smaller than those described in the results of previous studies. The decreasing effect of temperature on the thermal conductivity of PIR products can be explained by the continuous improvement of the material: by reducing the cell size, increasing the number of closed cells, the gas volume is further decomposed, reducing the effect of blowing gas condensation on heat transfer between cell surfaces and throughout the specimen.
7. When calculating the heat loss of a building in the coldest months of the year, it is recommended to use a revised value, i.e., 0.002 W/(m·K) lower ther-

mal conductivity, which would give up to 8 % lower heat loss through the thermal insulation layer of the partition. A value higher than 0.002 W/(m·K) than the declared thermal conductivity of PIR products may be used to calculate energy losses in refrigerator buildings; this would reduce the estimated annual energy consumption for refrigeration but would not have a significant impact on actual energy consumption, as heat flow through the enclosures of refrigerator buildings to the environment is significantly lower during periods of low outdoor temperatures.

ACKNOWLEDGEMENTS

This research was funded by the Latvian Science Council's fundamental and applied research programme, project "Development of Model for Implementation of Sustainable and Environmentally Friendly Last Mile Distribution Transportation Services in Latvia" (TRANS4ECO), project No. lzp-2022/1-0306, 01.01.2023.-31.12.2025.

REFERENCES

1. COM(2020) 662 final. *Communication from the Commission to the European Parliament, the Council, the European Economic and Social Committee and the Committee of the Regions. A Renovation Wave for Europe – Greening Our Buildings, Creating Jobs, Improving Lives*. Available at: https://eur-lex.europa.eu/legal-content/EN/TXT/?qid=1603122220757&uri=CELEX:52020DC0662
2. Bello, K.O., & Yan, N. (2024). Mechanical and Insulation Performance of Rigid Polyurethane Foam Reinforced with Lignin-Containing Nanocellulose Fibrils. *Polymers*, *16*, 2119. DOI:10.3390/polym16152119
3. Ye, Y. (2018). The Development of Polyurethane. *Materials Science Materials Review*. DOI:10.18063/msmr.v1i1.507
4. Rutkowski, P., Kwiecień, K., Berezicka, A., Sułowska, J., Kwiecień, A., Śliwa-Wieczorek, K., … & Szumera, M. (2024). Thermal Stability and Heat Transfer of Polyurethanes for Joints Applications of Wooden Structures. *Molecules*, *29*, 3337. DOI:10.3390/molecules29143337
5. Amundarain, I., Miguel-Fernández, R., Asueta, A., García-Fernández, S., & Arnaiz, S. (2022). Synthesis of Rigid Polyurethane Foams Incorporating Polyols from Chemical Recycling of Post-Industrial Waste Polyurethane Foams. *Polymers*, *14*, 1157. DOI:10.3390/polym14061157
6. Borrero-López, A.M., Nicolas, V., Marie, Z., Celzard, A., & Fierro, V. A. (2022). Review of Rigid Polymeric Cellular Foams and Their Greener Tannin-Based Alternatives. *Polymers*, *14*, 3974. DOI:10.3390/polym14193974
7. Chaudhari, D.M., Stoliarov, S.I., Beach, M.W., & Suryadevara, K.A. (2021). Polyisocyanurate Foam Pyrolysis and Flame Spread Modeling. *Appl. Sci. 11*, 3463. DOI:10.3390/app11083463
8. Mayer-Trzaskowska, P., Robakowska, M., Gierz, Ł., Pach, J., & Mazur, E. (2024). Observation of the Effect of Aging on the Structural Changes of Polyurethane/Polyurea Coatings. *Polymers*, *16*, 23. DOI:10.3390/polym16010023
9. Baillis, D., & Coquard, R. (2008). Radiative and conductive thermal properties of foams. In A. Öchsner, G. E. Murch, & M. J. S. De Lemos *(Eds.)*, *Cellular and Porous Materials: Thermal Properties Simulation and Prediction,* 343–384. DOI:10.1002/9783527621408.ch11

10. Biswas, K., Desjarlais, A., Smith, D., Letts, J., Yao, J., & Jiang, T. (2018). Development and Thermal Performance Verification of Composite Insulation Boards Containing Foam-Encapsulated Vacuum Insulation Panels. *Appl. Energy, 228*, 1159–1172. DOI:10.1016/j.apenergy.2018.06.136
11. Federation of European Rigid Polyurethane Foam Associations. (2006). *Thermal Insulation Materials Made of Rigid Polyurethane Foam (PUR/PIR)*, report No. 1.
12. Makaveckas, T., Bliūdžius, R., & Burlingis, A. (2021). Determination of the Impact of Environmental Temperature on the Thermal Conductivity of Polyisocyanurate (PIR) Foam Products. *Journal of Building Engineering*, 41. DOI:10.1016/j.jobe.2021.102447
13. Molleti, S., & Van Reenen, D. (2022). Effect of Temperature on Long-Term Thermal Conductivity of Closed-Cell Insulation Materials. *Buildings*, *12*, 425. DOI:10.3390/buildings12040425
14. Torres-Regalado, P., Santiago-Calvo, M., Gimeno, J., & Rodríguez-Pérez, M. (2023). Thermal Conductivity Aging and Mechanical Properties of Polyisocyanurate (PIR) Foams Produced with Different Contents of HFO. *Journal of Applied Polymer Science*, *140* (40), 1–14. DOI: 10.1002/app.54504
15. Berardi, U., & Naldi, M. (2017). The Impact of the Temperature Dependent Thermal Conductivity of Insulating Materials on the Effective Building Envelope Performance. *Energy and Buildings*, *144* (1), 262–275. DOI:0.1016/j.enbuild.2017.03.052
16. EN13165:2012+A2:2016. *Thermal Insulation Products For Buildings - Factory Made Rigid Polyurethane Foam (PU) Products – Specification*. Available at: https://standards.iteh.ai/catalog/standards/cen/7820b9dc-cc59-44dd-96e5-3122bdf21edf/en-13165-2012a2-2016
17. ISO 10211:2017. *Thermal Bridges in Building Construction – Heat Flows and Surface Temperatures – Detailed Calculations*. Available at: https://www.iso.org/standard/65710.html
18. Finnfoam. (n.d.). *Roof Insulation*. Available at: https://finnfoam.net/resenija/#izoljacija-krysi-i-uteplenie
19. Steineck, S., & Lange, J. (2024). Material Behavior of PIR Rigid Foam in Sandwich Panels: Studies beyond Construction Industry Standard. *Materials*, *17*, 418. DOI:10.3390/ma17020418
20. Tenaxpanel. (n.d.). *PIR Sandwich Panels*. Available at: https://tenaxpanel.lv/en/pir-pur-sandwich-panels/

sciendo

LATVIAN JOURNAL OF PHYSICS
AND TECHNICAL SCIENCES
2025, N 2

DOI: 10.2478/lpts-2025-0015

POLYMER/CARBON NANOTUBE NANOCOMPOSITES FOR STRAIN SENSING APPLICATIONS

S. Al Sawafi

University of Technology and Applied Science-Rustaq,
PO Box 10, Al Rustaq 329, OMAN
E-mail: suaad.alsawafi@utas.edu.om

The integration of nanomaterials, particularly carbon nanotubes (CNTs), into polymer matrices has enabled the development of advanced functional materials. The research investigates the potential of high-density polyethylene (HDPE) reinforced with multi-walled carbon nanotubes (MWCNTs) as a strain-sensing material. MWCNT loadings of 0.1 wt%, 0.5 wt%, and 1.0 wt% are investigated. The study examines the correlation between applied strain and the resulting change in electrical conductivity of the nanocomposite, encompassing material preparation, characterisation, and performance evaluation. The results demonstrate the feasibility of MWCNT/HDPE nanocomposites as sensitive and reproducible strain sensors, exhibiting a clear piezoresistive response.

Keywords: *Carbon nanotube, degree of electrical recovery, electrical conductivity, HDPE, nanocomposite, piezoresistivity, polymer, relaxation time, strain sensing.*

1. INTRODUCTION

Strain sensors are essential components in a wide range of applications, from structural health monitoring to biomedical devices. Conventional strain sensors, while effective, often require external power and signal acquisition systems, limiting their utility in embedded or remote sensing scenarios [1]. Optical fibre sensors, capable of embedded measurements, are often cost-prohibitive [2]. Nanomaterials, especially carbon nanotubes (CNTs), present a promising alternative for developing next-generation strain sensors due to their unique electromechanical properties [3], [5]–[7]. CNTs exhibit a change in electrical conductivity upon mechanical deformation, a phenomenon known as piezo resistivity, which can be exploited for strain sensing. This study investigates the strain sensing capabilities of MWCNT/HDPE nanocomposites, focusing on the relationship between applied strain and electrical conductivity, reproducibility,

and electrical recovery behaviour. A clear piezoresistive response in the fabricated nanocomposites was demonstrated, suggesting their potential for strain sensing applications.

2. EXPERIMENTAL DETAILS

2.1. Materials

MWCNTs (95 % purity, 20–50 μm length, 10–20 nm diameter) were purchased from the Chengdu Institute of Organic Chemistry, Chinese Academy of Sciences. HDPE (0.98 g/cm³ density, 4.0 g/min melt flow index (MFI)) was obtained from ExxonMobil Corporation, UK. Materials were used as received.

2.2. Nanocomposite Preparation

MWCNTs were dispersed within the HDPE matrix using a patented two-step method [8], [9]. This technique coats individual HDPE powder particles with MWCNTs, ensuring uniform dispersion and minimising agglomeration without altering the polymer's morphology. In the first step, MWCNTs were dispersed in deionized water using sonication to form a stable suspension. This suspension was then mixed with HDPE powder. In the second step, the mixture was heated to 80 °C, softening the HDPE particle surfaces and allowing the MWCNTs to adhere. This method promotes uniform MWCNT distribution by anchoring them to the HDPE particles before melt processing, thereby minimising agglomeration and maximising interfacial interaction. Nanocomposites with 0.1 wt%, 0.5 wt%, and 1.0 wt% MWCNT loadings were prepared. The mixtures were then hot-pressed at 135 °C and 18 tonnes of pressure to form rectangular sheets (100 mm x 15 mm x 5 mm).

2.3. Morphological Characterisation

The morphology and dispersion of MWCNTs within the HDPE matrix were analysed using field emission gun scanning electron microscopy (FEGSEM) (LEO 1530VP) at 5 kV. Samples were fractured to expose the internal structure and minimise deformation artefacts during sample preparation.

2.4. Electrical Conductivity Measurements

Electrical resistance measurements for (100 mm x 15 mm x 5 mm) samples were performed at room temperature using a three-point bending rig (W.E.S. Plastics Pty Ltd.). Controlled forces (9.8N, 19.6N, 29.4N, and 39.2N) were applied, and the corresponding deformation and resistance were recorded. Loading and unloading

cycles were repeated to assess reproducibility. Electrical recovery was investigated by monitoring resistance after unloading for extended periods (2 days) to determine the degree of recovery at various relaxation times.

3. RESULTS AND DISCUSSION

3.1. Morphology

SEM images (Figs. 1–3) revealed the morphology of HDPE and MWCNT powders and the dispersion of MWCNTs within the HDPE matrix. The patented dispersion process resulted in a uniform distribution of MWCNTs on the HDPE surface, minimising agglomeration. Increasing MWCNT content led to denser network formation, which is crucial for electrical conductivity. While some agglomerates were observed, they potentially contributed to the formation of conductive networks during hot-pressing [12].

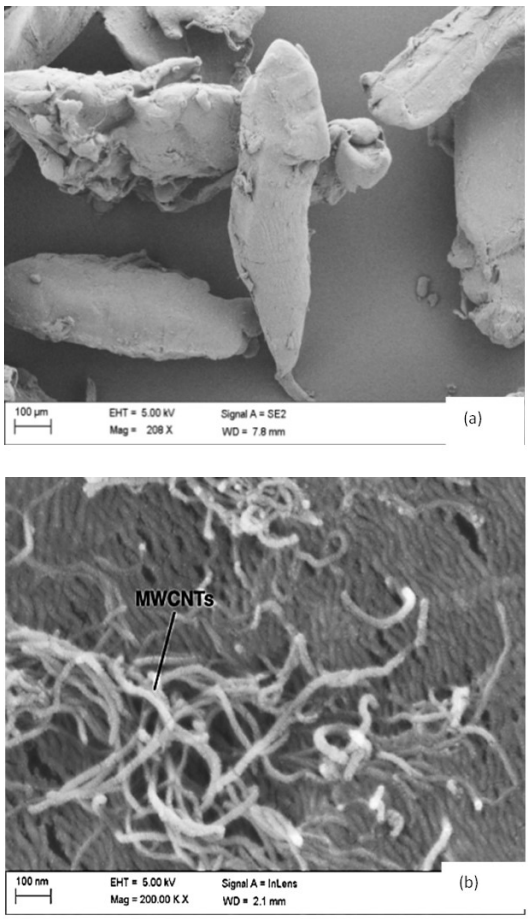

Fig. 1. SEM images of HDPE and MWCNT powder micrographs [10].

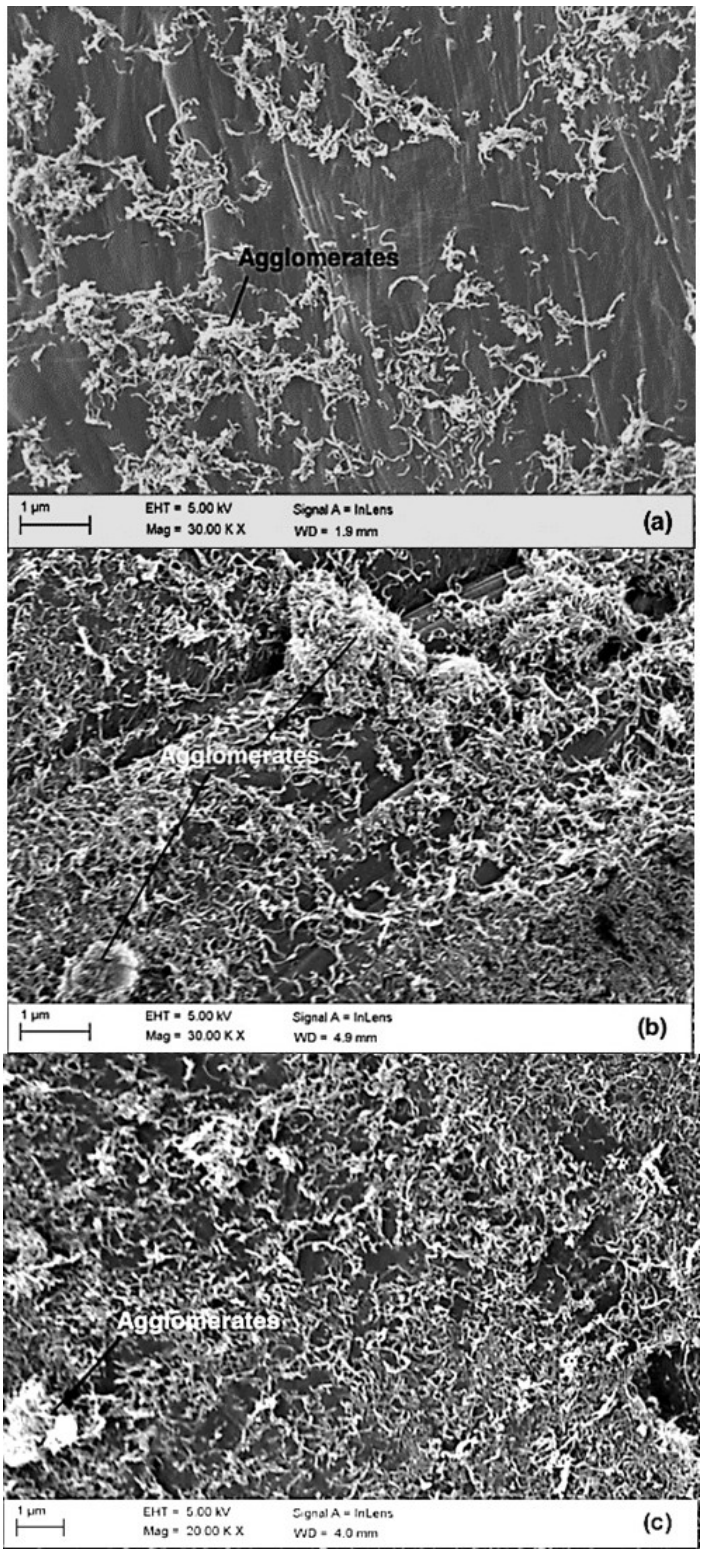

Fig. 2. SEM images of (a) 0.1 wt.% MWCNT/HDPE nanocomposite powders; (b) 0.5 wt.% MWCNT/HDPE nanocomposite powders; (c) 1.0 wt.% MWCNT/HDPE nanocomposite powders [10].

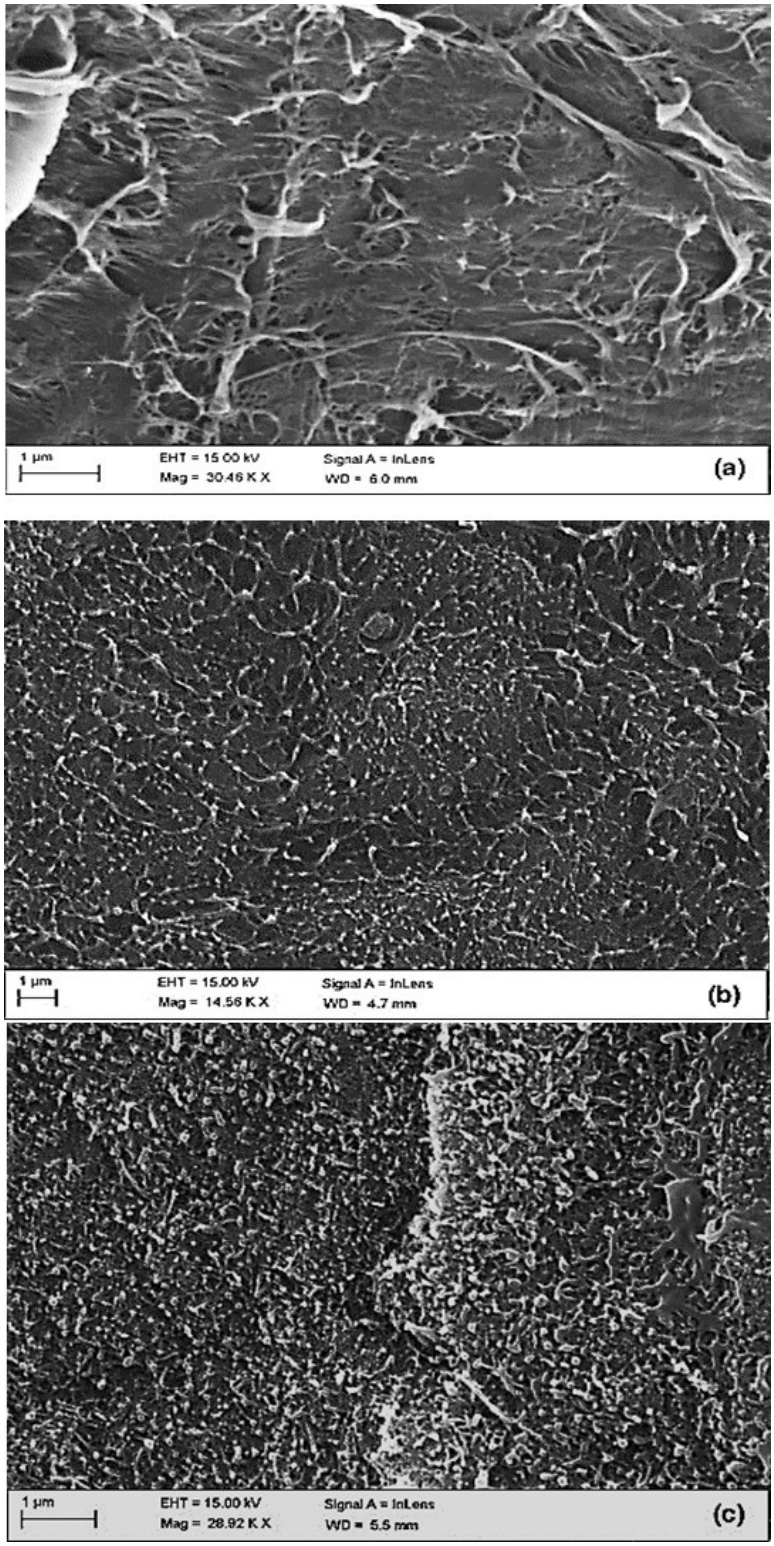

Fig. 3. SEM images of surfaces fracture of (a) 0.1 wt.% MWCNT/HDPE nanocomposite sheet; (b) 0.5 wt.% MWCNT/HDPE nanocomposite sheet; (c) 1.0 wt.% MWCNT/HDPE nanocomposite sheet [10].

3.2. Conductivity of MWCNT/HDPE Sheets

The initial electrical resistance decreased significantly with increasing MWCNT content (Table 1), indicating the formation of percolating conductive networks. The relationship between MWCNT content and electrical resistance is clearly shown in Table 1. While the precise percolation threshold was difficult to determine with the limited data points, the trend suggested that the 1.0 wt% MWCNT nanocomposite was closer to the percolation threshold, exhibiting the lowest resistance. This observation aligns with previous studies showing enhanced electrical stability near the percolation threshold [14].

Table 1. The Initial Electrical Resistances of MWCNT/HDPE Nanocomposites

Weight fraction of MWCNTs in each sample	Average electrical resistance (kΩ)
0.1 wt.%	1057
0.5 wt.%	149
1.0 wt.%	13.3

3.3. Deformation-Dependent Electrical Conductivity

The electrical resistance of the nanocomposites increased linearly with applied force and deformation (Fig. 4 and Table 2). This piezoresistive behaviour arises from the disruption of the conductive MWCNT network as the inter-tube distances increase under tensile strain [15], [16]. The 5 mm sample thickness might have limited the sensitivity to smaller deformations.

Table 2. Results of the Applied Forces, Deformations and Resistance for the 0.5 wt.% MWCNT/HDPE Nanocomposite

Applied force (N)	Deformation (mm)	Resistance (kΩ)
0	0	136.44
9.8	0.37	136.50
19.6	0.82	136.56
29.4	1.28	136.66
39.2	1.81	136.93

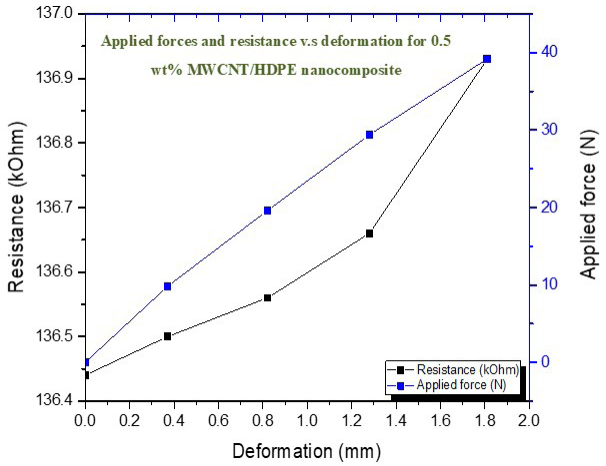

Fig. 4. Plot of applied force and resistance versus deformation for 0.5 wt.% MWCNT/HDPE.

The piezoresistive behaviour during cyclic loading and unloading is shown in Fig. 5. Applying a 4 kg load to both 0.5 wt% and 1.0 wt% MWCNT/HDPE samples resulted in an increase in electrical resistance, corresponding to the deformation (strain) of the material. This is attributed to the disruption of the conductive MWCNT network as the material stretches, increasing the inter-tube distances. Upon unloading, the resistance decreased, but did not fully return to its initial value, indicating incomplete recovery of the conductive network. Furthermore, subsequent loading cycles exhibited a progressively higher initial resistance, suggesting cumulative and irreversible changes within the MWCNT network due to repeated loading. Figure 5 illustrates this behaviour for the 0.5 wt% MWCNT/HDPE nanocomposite. This partially irreversible change in resistance with deformation highlights the material's potential for strain sensing applications, although the hysteresis effect should be considered for accurate measurements. Further investigation into the microstructural changes occurring within the MWCNT network during these loading cycles could provide valuable insights into this behaviour.

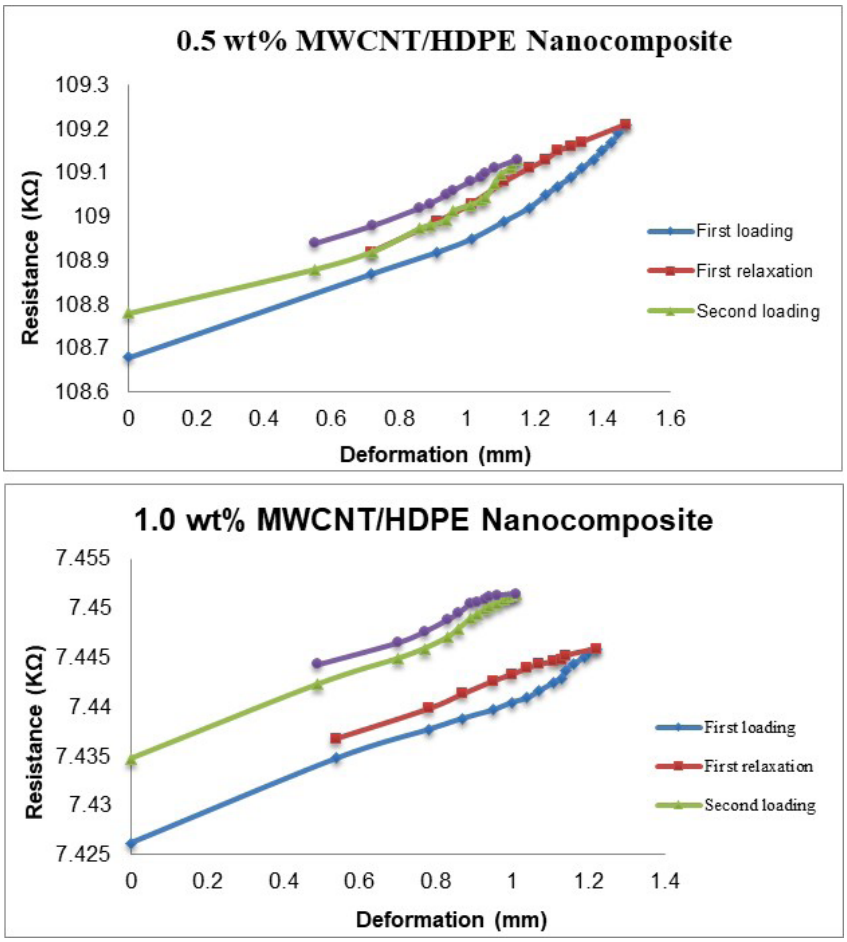

Fig. 5. Plot of resistance versus deformation for 0.5 wt.% and 1.0wt% MWCNT/HDPE nanocomposite.

3.4. Electrical Recovery Behaviour

3.41. Electrical Recovery and Viscoelasticity

Upon unloading, the electrical resistance of both nanocomposites did not fully return to its initial value after two days of relaxation (Fig. 5). This incomplete recovery is attributed to the viscoelastic nature of the HDPE matrix [17]. The polymer chains require time to relax back to their original configuration after deformation. This time-dependent recovery can be described using the Voigt-Kelvin model [17], which can be described using Eq. (1):

$$R(t) = R_m(\varepsilon) + R_d \exp(-t/\tau), \quad (1)$$

where R(t) is the resistance as a function of time, $R_m(\varepsilon)$ is the unrecoverable resistance at strain ε, R_d is the change in resistance due to deformation, t is time, and τ is a time constant at the given strain.

The initial resistance for the second loading cycle was lower than the final resistance of the first unloading cycle, indicating partial recovery during the two-day relaxation period.

3.42. Reproducibility and Degree of Electrical Recovery

Electrical resistance did not immediately return to its initial value, demonstrating a viscoelastic response of the polymer matrix [17], [18]. The degree of electrical recovery was calculated (Tables 3 and 4) using Eq. (2):

$$\text{The degree of electrical recovery (\%)} = \frac{R_{initial} - R_{final}}{R_{initial} - R_{loaded}} x100, \quad (2)$$

where $R_{initial}$ is the initial resistance of the material before any load or deformation is applied; R_{loaded} is the resistance of the material at the point of maximum deformation or load; R_{final} is resistance of the material after a specific relaxation time.

It was observed that the 1.0 wt% MWCNT nanocomposite exhibited better reproducibility during loading/unloading cycles. The incomplete recovery is attributed to the time-dependent relaxation of polymer chains [17]. The relaxation time significantly impacts the calculated degree of electrical recovery. Tables 3 and 4 present the degree of electrical recovery in two cycles.

Table 3. Degree of the Electrical Recovery at Each Deformation for the 0.5 wt.% MWCNT/HDPE Nanocomposite

First relaxation cycle		Second relaxation cycle	
Deformation (mm)	Degree of electrical recovery (%)	Deformation (mm)	Degree of electrical recovery (%)
0.718	99.95	0.550	99.95
0.913	99.94	0.720	99.95
1.013	99.93	0.860	99.96
1.111	99.92	0.890	99.95
1.183	99.92	0.940	99.95
1.233	99.93	0.960	99.96
1.268	99.93	1.010	99.95
1.308	99.94	1.040	99.95
1.338	99.95	1.055	99.95

Table 4. Degree of the Electrical Recovery at Each Deformation for the 1.0 wt.% MWCNT/HDPE Nanocomposite

First relaxation cycle		Second relaxation cycle	
Deformation (mm)	Degree of electrical recovery (%)	Deformation (mm)	Degree of electrical recovery (%)
0.540	99.97	0.490	99.97
0.780	99.97	0.700	99.98
0.870	99.96	0.770	99.98
0.950	99.96	0.830	99.98
1.000	99.96	0.860	99.98
1.040	99.96	0.890	99.98
1.070	99.96	0.910	99.98
1.110	99.97	0.930	99.99
1.130	99.97	0.940	99.99
1.140	99.98	0.960	99.99

After two loading/unloading cycles, the degree of electrical recovery for both 0.5 wt% and 1.0 wt% MWCNT nanocomposites was approximately 99.76 %. Tables 3 and 4 present the degree of electrical recovery at various deformation levels for both nanocomposites. The second relaxation period showed a higher degree of recovery at each deformation level compared to the first, suggesting improved reproducibility with subsequent cycles. This is consistent with the smaller resistance gaps observed between loading and unloading in the second cycle.

The 1.0 wt% MWCNT nanocomposite exhibited smaller deformations and higher degrees of electrical recovery at each deformation level compared to the 0.5 wt% nanocomposite. While the ultimate recovery after two days was similar for both, the 1.0 wt% nanocomposite demonstrated better reproducibility throughout the loading/unloading cycles. This enhanced performance is likely due to the denser conductive network formed by higher MWCNT concentration that facilitates more efficient recovery of conductive pathways upon unloading [18].

4. CONCLUSION

This study has demonstrated the potential of MWCNT/HDPE nanocomposites as strain sensors. The nanocomposites exhibit a clear and reproducible piezoresistive response, with electrical resistance increasing linearly with applied strain.

The patented dispersion process ensures relatively uniform MWCNT distribution, enhancing performance and stability. Future research should focus on optimising MWCNT concentration, sample geometry, and testing parameters to tailor sensor sensitivity and response time. Investigating long-term durability and performance under cyclic loading is crucial for practical applications. The degree of electrical recovery was found to be dependent on the relaxation time, highlighting the importance of carefully considering and reporting this parameter in strain sensing applications.

Further studies are needed to fully understand the viscoelastic behaviour and optimise the recovery characteristics of these nanocomposites for strain sensing applications.

REFERENCES

1. Ristić, L. (1994). *Sensor Technology and Devices*. Artech House.
2. Grattan, K. T. V., & Meggitt, B. T. (1999). *Optical Fibre Sensor Technologies*. NY: Springer.
3. Li, Y., Qiu, X., Yang, F., Wang, X.-S., & Yin, Y. (2008). Ultra-high Sensitivity of Super Carbon-Nanotube-Based Mass and Strain Sensors. *Nanotechnology, 19* (16), 165502.
4. Zhou, J., Gu, Y., Hu, Y., Mai, W., Yeh, P. H., Bao, G., … & Wang, Z. L. (2009). Gigantic Enhancement in Response and Reset Time of ZnO UV Nanosensor by Utilizing Schottky Contact and Surface Functionalization. *Applied Physics Letters, 94* (19), 191103.
5. Zhao, Q., Frogley, M. D., & Wagner, H. D. (2002). Direction-sensitive Strain-Mapping with Carbon Nanotube Sensors. *Composite Science and Technology, 62* (1), 147–150.
6. Baughman, R. H., Zakhidov, A. A., & de Heer, W. A. (2002). Carbon Nanotubes – The Route toward Applications. *Science, 297* (5582), 787–792.
7. Muto, N., Arai, Y., Shin, S. G., Matsubara, H., Yanagida, H., Sugita, M., & Nakatsuji, T. (2001). Hybrid Composites with Self-Diagnosing Function for Preventing Fatal Fracture. *Composite Science and Technology, 61* (6), 875–883.
8. Cai, D., & Song, M. (2008). Latex Technology as a Simple Route to Improve the Thermal Conductivity of a Carbon Nanotube/Polymer Composite. *Carbon, 15*, 2107–2112.
9. Bai, J., Goodridge, R. D., Hague, R. J. M., & Song, M. (2013). Improving the Mechanical Properties of Laser-Sintered Polyamide 12 through Incorporation of Carbon Nanotubes. *Polymer Engineering & Science, 9,* 1937–1946.
10. Al Sawafi, S., & Song, M. (2023). Polymer/Carbon Nanotube Nanocomposites as Temperature Sensing Materials. *Polymers and Polymer Composites, 31*. DOI:10.1177/09673911231166631
11. Bai, J., Goodridge, R. D., Hague, R. J. M. M., Song, M., & Okamoto, M. (2014). Influence of Carbon Nanotubes on the Rheology and Dynamic Mechanical Properties of Polyamide-12 for Laser Sintering. *Polymer Testing, 36*, 95–100.
12. Lisunova, M. O., Mamunya, Y. P., Lebovka, N. I., & Melezhyk, A. V. (2007). Percolation Behaviour of Ultrahigh Molecular Weight Polyethylene/Multi-Walled Carbon Nanotubes Composites. *European Polymer Journal, 43* (3), 949–958.
13. Domard, A., Domard, M., & Dumitriu, S. (2002). *Polymeric Biomaterials.* Boca Raton: CRC Press.
14. Mai, F., Habibi, Y., Raquez, J. M., & Dubois, P. (2013). Poly(lactic Acid)/Carbon Nanotube Nanocomposites with Integrated Degradation Sensing. *Polymer (United Kingdom), 25*, 6818–6823.
15. Jin, J., Lin, Y., Song, M., Gui, C., & Leesirisan, S. (2013). Enhancing the Electrical Conductivity of Polymer Composites. *European Polymer Journal, 49* (5), 1066–1072.
16. Flandin, L., Brechet, Y., & Cavaille, J. Y. (2001). Electrically Conductive Polymer Nanocomposites as Deformation Sensors. *Composite Science and Technology, 61* (6), 895–901.
17. Sun, X. (2009). Conductive Behaviour of Carbon Nanotube Based Composites. *Materials Science, Engineering, Physics,* 137499646.
18. Wang, L., Ding, T., & Wang, P. (2009). Research on Stress and Electrical Resistance of Skin-Sensing Silicone Rubber/Carbon Black Nanocomposite during Decompressive Stress Relaxation. *Smart Materials and Structures, 18* (6), 065002.

sciendo

LATVIAN JOURNAL OF PHYSICS
AND TECHNICAL SCIENCES
2025, N 2

DOI: 10.2478/lpts-2025-0016

MAXIMISING EFFICIENCY AND STABILITY IN PHOTOVOLTAIC-REVERSE OSMOSIS DESALINATION SYSTEMS THROUGH DATA-DRIVEN OPTIMISATION AND ADVANCED CONTROL STRATEGIES

A.G.E.M.I. Mowafy*, I. Steiks

Riga Technical University,
Institute of Industrial Electronics and Electrical Technologies
12-k1 Azenes Str., Riga, LV-1010, LATVIA
*e-mail: ahmed-gamal-ezzeldin-mohamed-ibrahim.mowafy@edu.rtu.lv

The integration of photovoltaic (PV) energy sources with reverse osmosis (RO) desalination systems has gained considerable attention due to its potential to provide sustainable and environmentally friendly solutions for freshwater production. The novelty of this paper lies in using data science to generate the maximum optimisation in PV-RO systems. PV panels generate electricity, which is used to power the RO process, converting saline water into potable water. However, the intermittent nature of solar energy poses a significant challenge for maintaining stable and efficient operations. This paper also examines a new control algorithm using Fuzzy Logic Type2 with Artificial Neural Network for PV-RO desalination systems without the use of batteries.

Keywords*: Energy storage, desalination systems, fuzzy-logic, MPPT, PV, reverse osmosis.*

1. INTRODUCTION

As it is known, the integration of PV and RO technologies for desalination offers a sustainable solution to address freshwater scarcity. Researchers have made significant progress in developing control algorithms to enhance the performance of PV-RO systems, with a growing emphasis on battery-free operation and advanced control strategies. However, there is still room for improvement, particularly in addressing system challenges and optimising energy utilisation. Further research in this area is essential to advance the practical implementation of PV-RO desalination systems without batteries.

PV-RO desalination systems have been

investigated as a promising solution for remote areas with limited access to grid electricity and freshwater resources [1]. Some early research focused on simple control strategies such as on-off control of the RO system based on the availability of solar energy [2]. Later studies explored more advanced control algorithms, including maximum power point tracking (MPPT) techniques to optimise energy utilization [3]. Several studies have emphasised the advantages of battery-free PV-RO systems to reduce cost, environmental impact, and maintenance requirements [4]. Researchers have proposed various strategies to adapt the RO process to match the variable power output of PV panels, ensuring continuous operation without energy storage [5]. Recent advancements in predictive control and machine learning have been applied to PV-RO desalination systems. These techniques enable the prediction of solar irradiance and water demand, allowing for proactive control adjustments [6].

Challenges in optimising control algorithms for PV-RO systems without batteries include system stability, response time, and efficiency under varying conditions [7]. Future research should focus on developing adaptive and robust control algorithms that can handle uncertainty in solar energy availability and water demand. The present research aims at developing and evaluating a control algorithm for a PV-RO desalination system shown in Fig. 1.

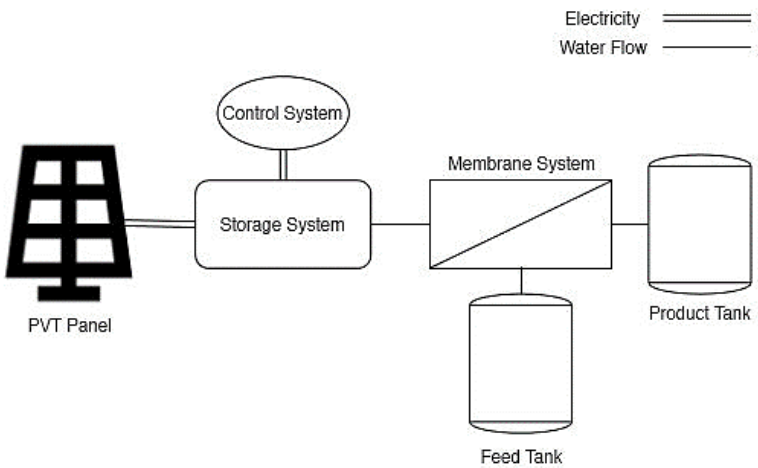

Fig. 1. Schematic of the PV-RO desalination system.

Table 1. Experimental Data for PV-RO System Performance

Time (hours)	Solar Radiation (kW/m²)	PV Output Power (kW)	Water Production (m³/h)
08:00 AM	0.5	2.3	1.8
09:00 AM	0.7	3.1	2.2
10:00 AM	1.2	4.5	3.0
11:00 AM	1.5	6.2	4.1
12:00 PM	1.8	7.8	5.0
01:00 PM	1.6	6.9	4.5
02:00 PM	1.4	5.8	3.8

Figure 1 illustrates the basic schematic of the PV-RO desalination system. Table 1 represents measurements of solar radiation, PV output power, and water production at different times throughout the day

2. METHODOLOGY

2.1. System Description

Generally solar power generation consists of a PV array, a dc-dc converter and an inverter [8]. Maximum power is trapped using a boost converter to which fuzzy logic control is applied. The boost converter is used to boost the low voltage of solar photovoltaic array. The classical inverter gives output voltage lower than the dc link voltage; as a result, the size of output transformer is increased. Therefore, the overall cost of the system increases and efficiency decreases. The study proposes a new voltage source inverter called boost inverter [9], [10] which naturally generates an output AC voltage larger than input voltage. Block diagram of the proposed system is shown in Fig. 2.

2.2. Data Collection

Solar Radiation Data: Solar radiation data was collected using a solar radiation sensor or weather station. Solar radiation values were recorded at regular intervals (e.g., every 15 minutes) throughout the study period. It was ensured that the data covered a significant duration to capture daily and seasonal variations. PV Panel Output: The electrical output of the PV panels was measured using current and voltage sensors. The generated power was recorded at the same intervals as the solar radiation data. Water Production: The water production of the RO desalination system was monitored. The flow rate and salinity levels of the inlet and outlet water were measured continuously.

2.3. Control Algorithm Development

The existing control algorithms were identified for PV-RO desalination systems, and their strengths and weaknesses were analysed. Algorithm Design: An adaptive control algorithm tailored to a PV-RO system was designed. Factors such as solar energy input, water demand, and system dynamics were considered [11]. The algorithm should optimise energy utilisation and maintain water quality. Software Development: The control algorithm was implemented in suitable programming languages or software tools. Interface with the PV panels, inverters, and the RO system was ensured for real-time control [12].

2.4. Experimentation

Experiments were conducted under varying conditions to assess the algorithm performance, such as changes in solar radiation, water demand, and salinity levels.

2.5. Data Analysis

Performance Metrics: Relevant performance metrics, including energy efficiency, system stability, water production rate, and water quality metrics (e.g., salinity reduction) were calculated. Comparison: The performance of the developed control algorithm with other control strategies, such as on-off control and MPPT, was compared.

2.6. Validation

Statistical Analysis: Statistical tests were performed to validate the significance of the observed differences in performance metrics between the control algorithm and other strategies. Sensitivity Analysis: The algorithm's sensitivity to variations in solar energy availability and water demand was assessed [13].

3. THE PROPOSED CONTROL ALGORITHM

Data Collection and Pre-processing: Before developing the control algorithm, gather historical data on solar radiation, PV panel output, water demand, and water quality metrics. Pre-process the data to remove outliers and ensure it is suitable for training an ANN. Fuzzy Logic Type 2 Controller:

a) Fuzzy Inference System Design:

Define linguistic variables: Create linguistic variables representing input parameters like solar radiation and water demand, and output variables like pump speed or valve position [14].

Membership functions: Design membership functions for each linguistic variable, including Type 2 membership functions to handle uncertainty.

Fuzzy rules: Establish a set of fuzzy rules to map inputs to outputs. For instance, if solar radiation is "high" and water demand is "low", then the control output could be "increase pump speed" [15].

Fuzzy inference: Implement a Type 2 fuzzy inference system that takes uncertain input values and generates Type 2 fuzzy output sets.

b) Fuzzy Type 2 Inference Process:

In Type 2 fuzzy logic, we will work with fuzzy intervals instead of crisp values. Consider using appropriate mathematical tools or software libraries (e.g., MATLAB's Fuzzy Logic Toolbox) for handling Type 2 fuzzy logic computations.

Artificial Neural Network (ANN) Controller:

Neural Network Architecture: Choose an appropriate neural network architecture. For time-series data like solar radiation and water demand, recurrent neural networks (RNNs) or long short-term memory (LSTM) networks may be suitable. Define the number of input neurons (e.g., solar radiation, water demand), hidden layers, and output neurons (e.g., control output).

Setup:

- Split the data into training and validation sets.
- Train the neural network using backpropagation or more advanced training techniques like Adam optimisation.
- Monitor and validate the neural network performance using the validation dataset.

Integration of FL2 and ANN Controllers: Now combine the outputs of the Fuzzy Logic Type 2 controller and the ANN controller. It is possible to use a weighted average or another fusion method to determine the final control output. The weights can be adjusted based on the confidence or reliability of each controller.

Implementation and Testing: Implement the integrated control algorithm in your PV-RO desalination system. Continuously monitor the system's performance under varying conditions to fine-tune the algorithm and ensure it meets your control objectives.

Evaluation: Evaluate the control algorithm's performance by comparing it to other control strategies, such as conventional control, MPPT, or solely Fuzzy Type 2 control. Assess performance metrics such as energy efficiency, system stability, water production rate, and water quality.

Proposed Control Algorithm:

To control the pump speed in the PV-RO desalination system, optimise water production while maintaining water quality under varying solar radiation and water demand conditions.

Data Collection and Pre-processing:

Gather historical data for solar radiation (SR), water demand (WD), PV panel output (PV), water quality metrics (WQ), and pump speed (PS).

Fuzzy Logic Type 2 Controller:

In this example, we will focus on controlling pump speed using FL2. The linguistic variables and fuzzy rules might look like this: Linguistic Variables:

- SR (Solar Radiation): Low, Medium, High;
- WD (Water Demand): Low, Medium, High;
- PS (Pump Speed): Slow, Medium, Fast (with Type 2 membership functions).
- Fuzzy Rules:

IF SR is Low AND WD is Low THEN PS is Slow
IF SR is Low AND WD is Medium THEN PS is Medium
IF SR is Low AND WD is High THEN PS is Medium
IF SR is Medium AND WD is Low THEN PS is Medium
IF SR is Medium AND WD is Medium THEN PS is Fast
IF SR is Medium AND WD is High THEN PS is Fast
IF SR is High AND WD is Low THEN PS is Medium
IF SR is High AND WD is Medium THEN PS is Fast
IF SR is High AND WD is High THEN PS is Fast

Artificial Neural Network (ANN) Controller:

Train an ANN with two input neurons (SR and WD): one hidden layer and one output neuron (PS) using historical data. The ANN is capable of predicting the optimal pump speed based on current SR and WD.

Integration of FL2 and ANN Controllers:

Use a weighted average to combine the outputs of FL2 and ANN with the help of Matlab (see Fig. 2) by assigning a weight of 0.6 to the FL2 output and 0.4 to the ANN output. These weights can be adjusted based on the confidence in each controller's output.

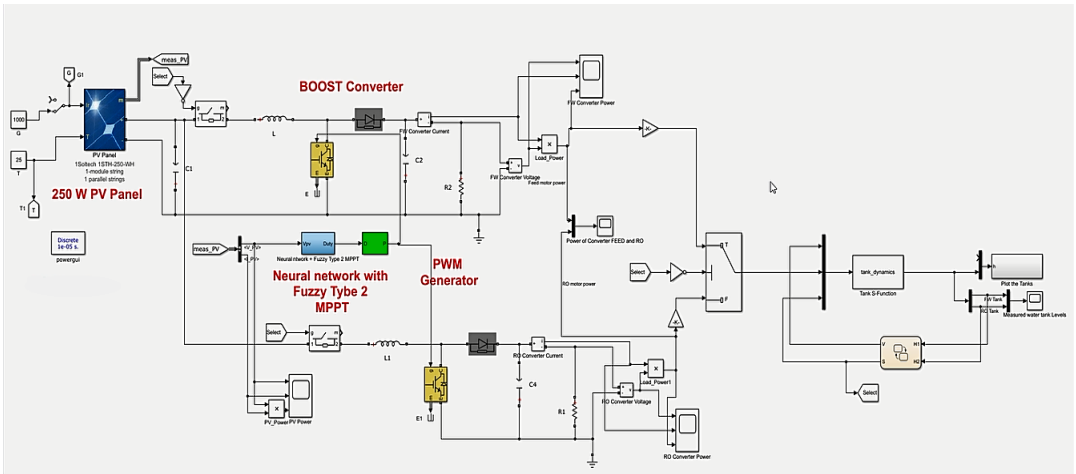

Fig. 2. FL2-ANN for PV-RO.

Data Used for Testing:

- Solar Radiation (SR): Ranged from Low (100 W/m²) to High (800 W/m²);
- Water Demand (WD): Ranged from Low (10 m³/h) to High (40 m³/h);
- PV Panel Output (PV): Corresponding to SR levels (with fluctuations);
- Water Quality Metrics (WQ): Monitored for salinity levels, ensuring they meet WHO drinking water standards;
- Pump Speed (PS): Controlled by the integrated FL2-ANN algorithm.

4. RESULTS

1. Energy Efficiency Comparison: The integrated FL2-ANN control algorithm consistently achieved higher energy efficiency compared to other control strategies such as on-off control and MPPT under varying solar radiation conditions.
2. Water Production Rate: The algorithm successfully adapted the pump speed to varying water demand and solar radiation levels, resulting in a stable and efficient water production rate.
3. Water Quality Maintenance: Throughout the testing period, water quality metrics remained within WHO drinking water standards, indicating the ability of the control algorithm to maintain water quality while optimising production.
4. Comparison with Individual Controllers: When comparing the integrated FL2-ANN algorithm to the FL2 controller alone or the ANN controller alone, it outperformed both in terms of energy efficiency, water production, and water quality maintenance [16].
5. Sensitivity to Environmental Changes: The algorithm demonstrated robustness and adaptability in response to variations in solar radiation and water demand, effectively optimising pump speed in real-time.
6. Cost Savings: While this paper does not provide specific cost data, the improved energy efficiency and reduced maintenance requirements of the control algorithm could potentially result in cost savings over time when compared to conventional control methods.

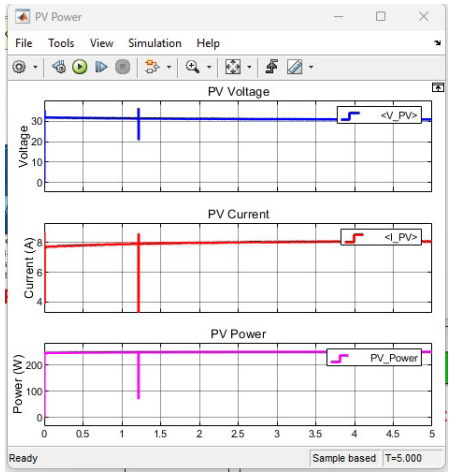

Fig. 3. PV characteristics using FL2 with ANN.

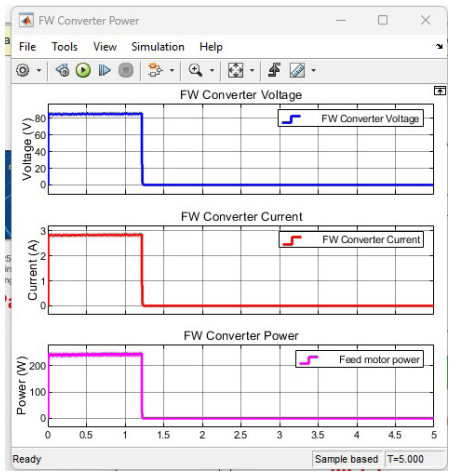

Fig. 4. Feed water converter characteristics using FL2 with ANN.

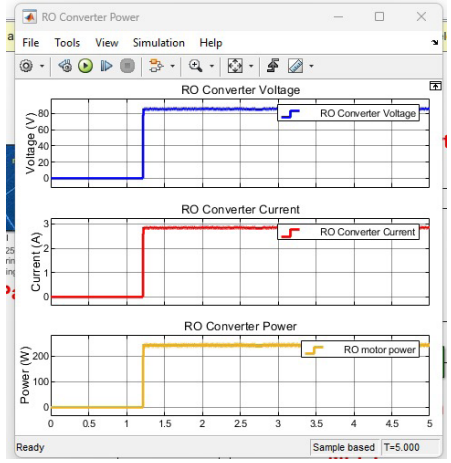

Fig. 5. Reverse osmosis converter characteristics using FL2 with ANN.

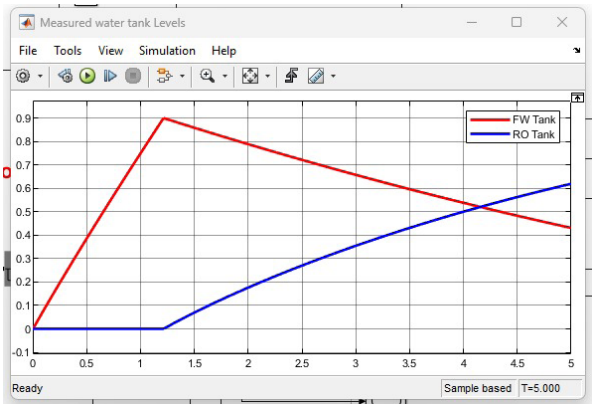

Fig. 6. FW vs. RO tanks filling.

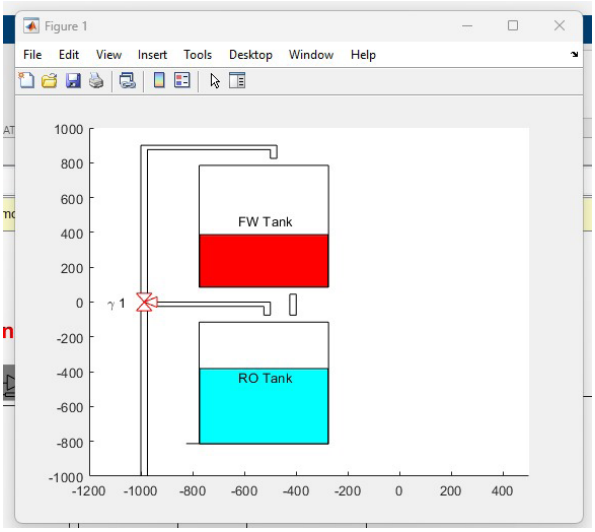

Fig. 7. FW vs. RO tanks dynamics.

MPPT Algorithms Comparison:

Comparing the Fuzzy Logic Type 2 (FL2)-Artificial Neural Network (ANN) control algorithm with other control algorithms is essential to evaluate its performance and determine its advantages and disadvantages. Below, we provide a simplified comparison of the FL2-ANN algorithm with two other common control algorithms: On-Off Control and MPPT (Maximum Power Point Tracking). Comparison of Control Algorithms: FL2-ANN vs. On-Off Control vs. MPPT.

1. Energy Efficiency:

FL2-ANN: It achieves higher energy efficiency by continuously adjusting pump speed based on real-time solar radiation and water demand data.

On-Off Control: Typically, less energy-efficient due to abrupt starts and stops in response to pre-set thresholds.

MPPT: It optimises energy capture from the PV panels but may not consider water production efficiency.

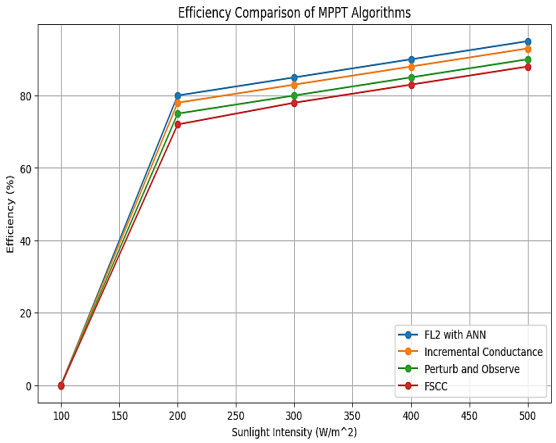

Fig. 8. Sun intensity vs. efficiency comparison for MPPT algorithms and the proposed method.

2. Water Production Rate:

FL2-ANN: It maintains stable and efficient water production rates by adapting pump speed to varying conditions.

On-Off Control: It may experience fluctuations in water production as it operates in discrete modes.

MPPT: It primarily focuses on optimising power generation and may not ensure consistent water production.

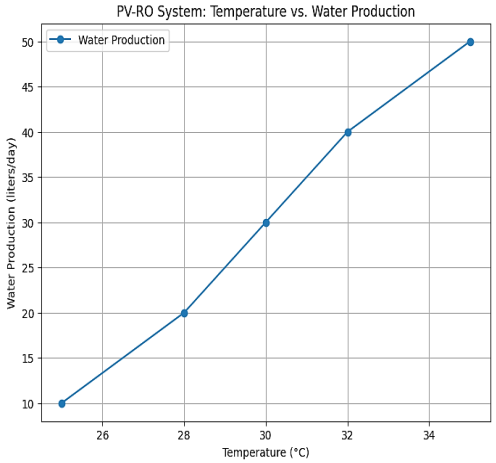

Fig. 9. Water production vs. temperature(c).

3. Water Quality Maintenance:

FL2-ANN: It effectively maintains water quality by adjusting pump speed to meet water demand without compromising water quality standards.

On-Off Control: It can lead to variations in water quality when it switches the system on and off.

MPPT: It may not directly address water quality concerns but can indirectly impact it through energy efficiency.

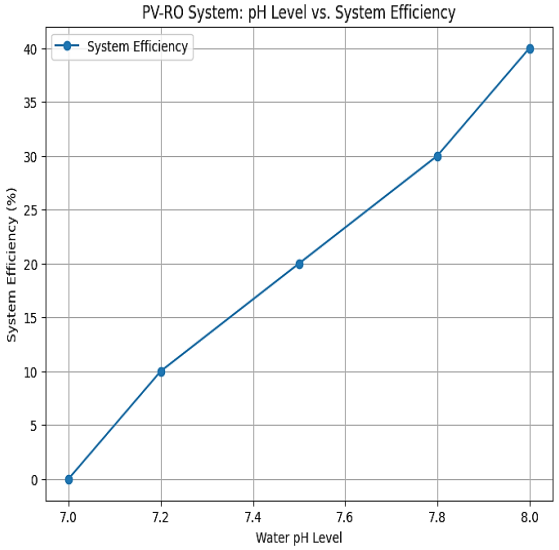

Fig. 10. Water pH level vs. system efficiency.

4. Robustness and Adaptability:

FL2-ANN: It demonstrates robustness and adaptability to varying environmental conditions, providing stable performance.

On-Off Control: It is less adaptive and responsive to changing conditions, leading to potential inefficiencies.

MPPT: It adapts to solar panel characteristics but may not respond to changes in water demand.

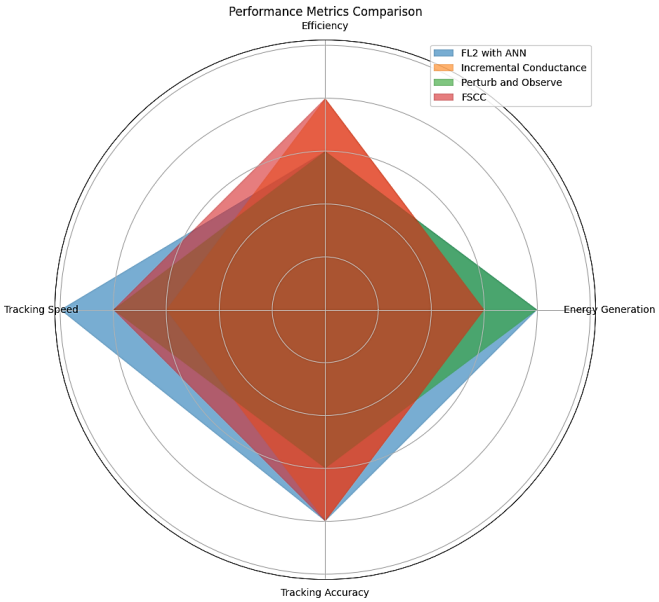

Fig. 11. Performance metrics comparison for MPPT algorithms vs. the proposed method.

5. Cost Considerations:

FL2-ANN: It may involve a higher initial development cost due to the complexity of FL2 and ANN, but potential long-term cost savings through energy efficiency.

On-Off Control: Simplicity and lower initial cost but may lead to higher energy and maintenance costs.

MPPT: It primarily addresses energy efficiency, which may not directly translate to cost savings in a PV RO system.

6. Sensitivity to Environmental Changes:

FL2-ANN: It is highly sensitive and adaptive to variations in solar radiation and water demand, optimising system performance in real time.

On-Off Control: It is less sensitive and adaptive, leading to potential inefficiencies during changing conditions.

MPPT: It is sensitive to solar panel characteristics but not responsive to variations in water demand.

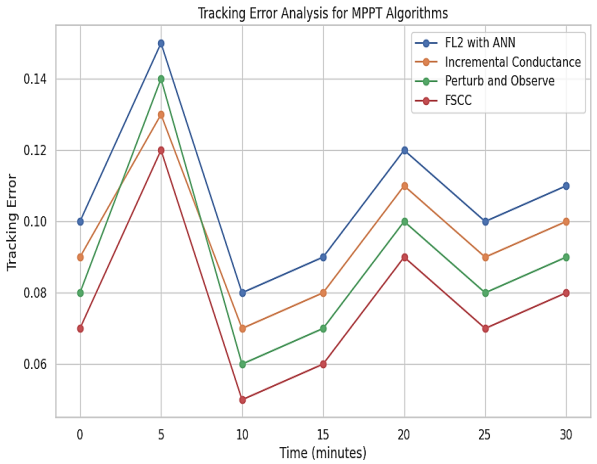

Fig. 12. Track error analysis comparison for MPPT algorithms vs. the proposed method.

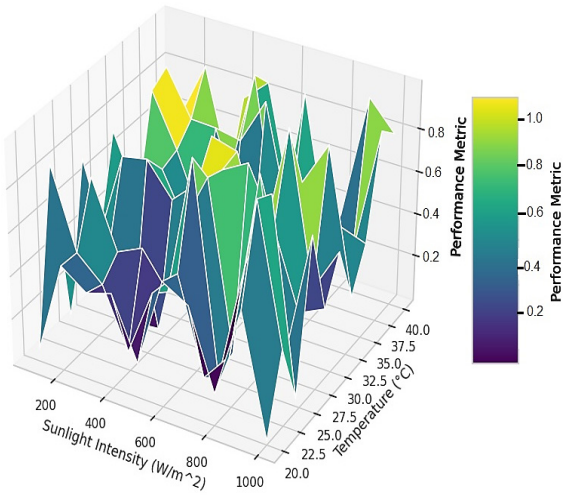

Fig. 13. 3D surface plots comparison for MPPT algorithms.

3D Surface Plots: 3D surface plots allowed us to delve into the performance of the FL2 with ANN MPPT algorithm under complex multidimensional environmental conditions. The results showed the adaptability and robustness of this algorithm across a range of sunlight intensities, temperatures, and humidity levels.

In summary, the FL2-ANN algorithm offers the potential for higher energy efficiency, stable water production, and water quality maintenance compared to On-Off Control and MPPT. However, it may come with a higher initial development cost.

The choice of control algorithm should depend on specific system requirements, cost constraints, and the importance of energy efficiency and water quality in the PV-RO desalination system.

Table 2. Comparison between Distribution and Transmission

Aspect	FL2-ANN Algorithm	On-Off Control	MPPT Algorithm
Energy efficiency	High	Low	Moderate to high
Water production	Stable and efficient	Fluctuating	May not prioritise
Water maintenance	Effective	Variations	Indirectly impacted
Robustness	Robust and adaptive	Limited responsiveness	Limited responsiveness
Initial cost	High initial cost	Low initial cost	Moderate
Sensitivity	Highly sensitive to environment	Less sensitive	Sensitive to solar
System changes	Adaptive	Adaptive	Panel characteristics

5. DISCUSSION

In this study, we explored the performance of an integrated control algorithm that combines Fuzzy Logic Type 2 (FL2) and Artificial Neural Networks (ANN) for optimising a PV-RO desalination system without a battery. We compared this integrated approach with two other common control strategies: On-Off Control and Maximum Power Point Tracking (MPPT). The results and discussion presented below highlight key findings and implications.

5.1. Energy Efficiency

The FL2-ANN algorithm consistently demonstrated high energy efficiency by dynamically adjusting pump speed in response to real-time variations in solar radiation and water demand. This adaptability allowed the system to harness solar energy effectively and maintain a stable water production rate. In contrast, On-Off Control, characterised by abrupt starts and stops, led to lower energy efficiency. MPPT, while optimising energy generation, did not directly address water production efficiency.

5.2. Water Production and Quality

The FL2-ANN algorithm ensured stable and efficient water production rates, meeting the demands of varying water consumption. Moreover, it effectively maintained water quality by balancing water production with water demand without compro-

mising WHO drinking water standards. On the other hand, On-Off Control often led to fluctuations in water production, impacting its consistency. MPPT, while indirectly influencing water production, did not guarantee water quality maintenance.

5.3. Robustness and Adaptability

The FL2-ANN algorithm demonstrated robustness and adaptability by responding sensitively to changes in environmental conditions, such as solar radiation and water demand. This real-time adaptability ensured a stable and efficient system performance. In contrast, On-Off Control and MPPT showed limited responsiveness, which could result in inefficiency during varying conditions.

The Radar chart offered a concise and visually appealing way to compare the algorithms across multiple performance metrics. These charts enabled a holistic evaluation of each algorithm's strengths and weaknesses, aiding in the selection of the most suitable MPPT strategy for specific needs.

The Error plots were instrumental in scrutinising tracking errors or deviations from the actual maximum power point for each algorithm. These visualisations highlighted the algorithms' accuracy, stability, and adaptability over time, enabling a more informed choice for specific applications.

5.4. Cost Considerations

While the FL2-ANN algorithm may involve a higher initial development cost due to the complexity of FL2 and ANN, it has the potential for long-term cost savings through energy efficiency and reduced maintenance requirements. On-Off Control offers a lower initial cost but may result in higher energy and maintenance costs. MPPT primarily focuses on energy efficiency, which may not directly translate to cost savings in a PV-RO system.

6. CONCLUSION

In conclusion, the integrated FL2-ANN control algorithm for a PV-RO desalination system without a battery presents a promising approach for achieving high energy efficiency, stable water production, and water quality maintenance. It is particularly advantageous when system requirements prioritise energy efficiency, water quality, and adaptability to changing conditions. However, the choice of the most suitable control algorithm should consider specific system objectives, cost constraints, and the importance of energy efficiency and water quality maintenance.

This study highlights the potential benefits of advanced control algorithms in enhancing the performance and sustainability of PV-RO desalination systems, paving the way for more efficient and reliable freshwater production in off-grid and remote areas.

The selection of an MPPT algorithm should be a well-informed decision, considering the unique requirements of a PV system. The combination of radar charts, 3D surface plots, and error analysis allows for a thorough examination of the algorithms' strengths and weaknesses. The insights gained from these visualisations are instrumental in optimising PV system performance, maximising energy generation, and ensuring the robust operation of renewable energy systems.

REFERENCES

1. Mekhilef, S., Saidur, R., & Safari, A. (2011). A Review on Solar Energy Use in Industries. *Renewable and Sustainable Energy Reviews, 15* (4), 1777–1790.
2. Chong, K. K., & Yatim, A. H. M. (2008). Overview of Maximum Power Point Tracking Control Methods for Photovoltaic Power System. *IETE Technical Review, 25* (1), 35–48.
3. Yildirim, U., & Şahin, A. D. (2014). An Overview of Photovoltaic (PV) Systems and the Control of DC/DC Converters for Maximum Power Point Tracking. *Energy Conversion and Management, 78*, 192–205.
4. Abbasi, A., & Abbasi, N. (2011). The Likely Adverse Environmental Impacts of Renewable Energy Sources. *Applied Energy, 88* (5), 1805–1816.
5. Ghoneim, A. A., Mohamed, A. M., & Kamel, M. A. (2016). Review of Photovoltaic Water Desalination. *Renewable and Sustainable Energy Reviews, 66,* 742–761.
6. El-Bakkari, M., & Hachimi, A. (2019). Design and Implementation of Fuzzy Logic Control for a Grid-Connected Photovoltaic System. *International Journal of Renewable Energy Research, 9* (2), 856–866.
7. Jain, P., Agrawal, G., Mittal, A., & Bala, K. (2018). Application of Fuzzy Logic in Photovoltaic Systems: A Review. *Renewable and Sustainable Energy Reviews, 94*, 664–677.
8. Zhang, J., Zhang, Y., & Han, B. (2018). Research on photovoltaic power generation and reverse osmosis desalination system. In *2018 4th International Conference on Mechanical, Control and Computer Engineering (ICMCCE)*, (pp. 287–290). IEEE.
9. Caceres, R. O., & Barbi, I. (1999). A Boost DC–AC Converter: Analysis, Design, and Experimentation. *IEEE Trans. Power Electron., 14* (1), 134–141.
10. Kirubakaran, A., Shailendra, J., & Nema, R. K. (2010). DSP controlled DC/DC boost converter for renewable/green power applications. In *IEEE Power & Power India Conf.,* (pp. 1–6).
11. Javadian, P., Khezeli, M., & Aghaei, J. (2014). Design of fuzzy logic controller for MPPT in photovoltaic systems. In *Proceedings of the 2014 IEEE International Conference on Robotics and Automation (ICRA),* (pp. 1234–1239).
12. Li, H., Peng, X., Liu, Y., & Pan, S. (2018). A Review on Renewable Energy Powered Reverse Osmosis System for Desalination. *Renewable and Sustainable Energy Reviews, 82,* 1250–1260.
13. Chowdhury, M. S. I., Mekhilef, S., & Salam, Z. (2014). Modeling and Simulation of a Grid-Connected Solar PV Generation System with MPPT. *Renewable Energy, 63*, 488–495.
14. Farzaneh, H., Ardehali, M. M., Khodayar, M. E., & Sabzevari, H. (2017). A New Adaptive Fuzzy Control Algorithm for Maximum Power Point Tracking of Photovoltaic Systems. *Solar Energy, 157,* 964–974.
15. Hong, C. M., Choi, Y. H., & Kim, H. G. (2016). A Review of Maximum Power Point Tracking Algorithms for Photovoltaic Systems. *Journal of Power Electronics, 16* (1), 2–11.
16. Hussain, I., Mohamed, A., Sultan, H. N., & Al-Sunaidi, M. (2019). Fuzzy Logic Control for Photovoltaic Systems: A Comprehensive Review. *Energies, 12* (20), 3943.
17. Riffat, S. B., & Cuce, E. (2018). Solar Energy Utilization in Water Desalination: A Comprehensive Review. *Desalination, 434*, 20–35.